DESALINATION OF WATER BY VAPOR TRANSPORT THROUGH HYDROPHOBIC NANOPORES

BY

JONGHO LEE

BACHELOR OF SCIENCE, MECHANICAL AND AEROSPACE ENGINEERING
SEOUL NATIONAL UNIVERSITY, 2003

MASTER OF SCIENCE, MECHANICAL AND AEROSPACE ENGINEERING
SEOUL NATIONAL UNIVERSITY, 2007

SUBMITTED TO THE DEPARTMENT OF MECHANICAL ENGINEERING IN PARTIAL FULLFILMENT OF THE REQUIREMENTS FOR THE DEGREE OF DOCTOR OF PHILOSOPHY IN MECHANICAL ENGINEERING

AT THE

MASSACHUSETTS ISTTITUTE OF TECHNOLOGY

SEPTEMBER 2014

Signature redacted

SIGNATURE OF AUTHOR.....

JONGHO LEE
DEPARTMENT OF MECHANICAL ENGINEERING
JULY 31, 2014

Signature redacted

CERTIFIED BY.....

ROHIT N. KARNIK
ASSOCIATE PROFESSOR, MECHANICAL ENGINEERING
THESIS SUPERVISOR

Signature redacted

ACCEPTED BY.....

DAVID E. HARDT
PROFESSOR, MECHANICAL ENGINEERING
CHAIRMAN, DEPARTMENT COMMITTEE ON GRADUATE STUDENTS

DESALINATION OF WATER BY VAPOR TRANSPORT THROUGH HYDROPHOBIC NANOPORES

BY

JONGHO LEE

Submitted to the Department of Mechanical Engineering
on July 31, 2014 in Partial Fulfillment of the
Requirements for the Degree of Doctor of Philosophy in
Mechanical Engineering

Abstract

Although Reverse osmosis (RO) is the state-of-the-art desalination technology, it still suffers from persistent drawbacks including low permeate flux, low selectivity for non-ionic species, and lack of resistance to chlorine. This leaves ample rooms for further improvement for RO technology by addressing these issues.

In this thesis, a new approach is proposed for desalination by vapor-phase transport through hydrophobic nanopores in an isothermal condition. Hydrophobic nanopores flanked by vapor-interfaces with a submicron gap provide a complete barrier for salt while behaving as highly permeable medium for water.

We first theoretically explore transport of water through a hydrophobic nanopore using a probabilistic model that incorporates rarefied gas dynamics, ballistic transport, and emission and reflection of water molecules at liquid-vapor interfaces. We then expand the model to transition regime where molecular diffusion coexists with the rarified gas transport. Effect of nanopore geometry, salinity, temperature, applied pressure, and interfacial reflection probability on the transport of water molecules through the nanopore are explored. We further realize membranes consisting of hydrophobic nanopores to experimentally study the transport with the various above-mentioned conditions.

We find the existence of two mass transport regimes, i.e., diffusion-governed and interface-governed transport, determined by interplay between transmission across the nanopores and condensation at the interfaces. The condensation resistance, represented by condensation coefficient, was experimentally measured. An accurate value of the condensation coefficient was estimated accordingly, which has been debated more than a century.

Based on this finding, the proposed approach is expected to produce up to ~2x higher permeate flux at 50°C and with porosity of 40% than conventional RO. This approach further decouples transport properties from membrane material properties, thereby opening the possibility of engineering membranes with appropriate materials that may lead to reverse osmosis membranes with improved flux, better selectivity, and high chlorine resistance allowing for inexpensive and simple fouling control.

Thesis Supervisor: Rohit Karnik
Title: Associate Professor in Mechanical Engineering

Acknowledgement

I came to Cambridge on August 2008, both with curiosity and anxiety for a totally new experience in a foreign country. The first thing that I encountered was a huge language barrier, which was much more overwhelming than I expected. Nevertheless, the first impression I received from my advisor Professor Rohit Karnik gave me much comfort and confidence for my academic life in MIT. He was very kind, gentle, and talked with a bit shy voice. From the first meeting, I got a feeling that I might be able to do well in MIT working with him. He was always supportive and tried to teach me better, and gave guidance in research directions. Especially, I truly appreciate that he walked with me having a language barrier in initial years. Although I heard many people say that there are a number of smart people in the world, I have never seen with my eyes such an intelligent person along with a gentle and humble personality. I believe that I was tremendously lucky to have him as my advisor. His curiosity in science along with his kind and warm attitude toward students and people made me have him as my role model in academia.

I thank all friends in the lab for their kindness and friendship. Suman, my best friend, sometimes looks like a ten years old kid inclined to do prank all the time, and also sometimes speaks like sixty years old man talking on career, life, and even love affair. I thank him for his friendship and fun moments we shared – including trips to Niagara fall, Martha's vineyard, Cape Cod, etc. I wish I had been to more conferences with him other than Gordon Research Conference. Marco – I like and respect his weird and also philanthropistic philosophy. He is always ready to help people including me even by postponing and sacrificing his priority. I always liked his funny but very thoughtful comments on topics I brought up. Sean – I like his frankness. Even though he looks serious in the first glance, I found Sean has a very fun character. So I always enjoyed conversation with him on various topics. Especially, because Sean was a perfect representative of Americans to me, it was always amusing to discuss with him on cultural, political or structural differences between my country and US. Tarun – he is a very weird philosopher and physicist in

our lab. As I have been aiming for academia, I have always admired his adventurous spirit, entrepreneurship, and courage for not worrying about near future. We would be short-term roommates in San Diego and Netherlands and I really enjoyed our conversations on universe, science, futures, etc. Mike – I admire his integrity, honesty, and diligence. But more than that, he is a very fun and friendly guy to hang out, equipped with excellent cynical jokes and comments. He and I made a good team for xylem project, finishing all necessary experiments in several days only. That would be my shortest but most reliable co-working. Chia – always quiet and shy girl, I remember that we had many discussions on similarity and difference between Taiwan and Korea. I was also extremely happy to see she is married and has a happy life in Connecticut. Jason – I don't think his love toward baseball will change ever as opposed to me who fell asleep in Fenway stadium during the match of Red Sox and Yankees. Sunandini – who always smiles and also has a fun and charming character, her group meeting presentation was always interesting to me. Jongmin – who never hurries and is calmed, I always hear about Korean academia news from him. As a father of two children, I have to learn more from him. Sungyoung is a solid and disciplined researcher, and I believe that he is one of the best experimentalists. I really wish for his successful career in academia, and I was happy to see he enjoys his research in Korea, having a happy family life. I also miss Cameron, Chong, Ricardo, and Ben who used to work in our lab for 8 months as co-op students from Waterloo. They were the smartest and dedicated undergrad students I have ever seen, and also fun young guys. I hope that they are going to use their young energy and passion on their bright futures.

Outside the lab, I also thank many other friends. Especially, Amith who started from my pingpong and tea mate in Mathematics department lounge, I am proud of him that he went through and overcame all hardships in MIT and I believe that he will be a great PhD in the end. I truly appreciate his friendship and sharing. Tom, as another membrane brother, and I shared a lot about frustrations whenever experiments failed. We also encouraged each other by showing that

the other of us also failed. I am proud that we both made the work happen, and received PhD together. I also thank my Korean friends, especially Hyunglae Lee, Won Kim, Kyoochul Park, and Jessie Jeon, who came to MIT with me on the year of 2008. I remember that we frequently shared our joys, excitements, worries, and frustration on our totally new circumstances, and we got help from each other a lot. Since I am the one who graduated latest, Hyunglae, Kyoochul, and Jessie as post-docs are now pursuing academic career and I give my best wish for their successful and happy lives and careers.

I cannot miss my family – my father, mother, and sister – who always pray for me and support me. I still remember the day I received admission from MIT, my father and mother were so happy and excited. Although my parents, especially my father, sometimes had a burdensome expectation on me, I appreciate that they now simply wish my happy family life. My sister, who always was proud of having a so-called smart brother, I honestly think that she is much smarter and wiser than me, and I admire her courage and persistence that I do not have. I want to say that I really love my father, mother, and my sister.

Lastly, Cambridge is a very special place to me, not because it is the first place I live in a foreign country, but because I met my wife Jeehye here. She is always lovely, adorable, cheerful, and adventurous. She never hesitates to share her emotions, love, and sorrow. I believe that my shy and passive nature has been affected and changed by her presence and character. She made my life fun, dynamic, rich and lovely. I truly appreciate that God allowed me to come to Cambridge and marry her, and to walk with her through our academic and emotional hardships and share our daily adventures and joys, and finally to have my lovely daughter Sohahn. I want to show my love to her and my daughter in this page again.

I want to thank all other friends and people whom I couldn't mention here, who always supported and prayed for me to finish this journey. I again thank God for privileging me to meet these

wonderful people and for the exotic and astonishing life in Cambridge he prepared. I pray to Him for my new and exciting journey in New Haven he is preparing for my family and me.

Contents

List of Figures

$\varphi_{A,B}$ with η and σ. The scale bar on the top of (c) represents the pore aspect ratio l/a corresponding to η.

Figure 7. Effect of pore aspect ratio l/a and condensation coefficient σ on the mass flux through the pore per unit driving pressure at different temperatures. $\varepsilon = 1$ is assumed to consider nanopore area only. (a) $\sigma = 0.5$; (b) $\sigma = 1.0$; (c) $l/a = 5$; (d) $l/a = 100$.

Figure 8. Detailed configuration of liquid-vapor interface at the feed side. θ_{eq} denotes equilibrium contact angle satisfying Young-Laplace equation (γ_{sl}-γ_{sv}+γ_{lv}cos θ_{eq}=0), and θ denotes the angle between a line tangential to interface and pore axis, which satisfies mechanical force equilibrium.

Figure 9. Minimum pore length that makes pore wetting energetically unfavorable at different values of the applied pressure and pore radius. Contact angle of 120°, NaCl concentration of 0.62M, and temperature of 20°C are assumed.

Figure 10. Predicted mass flux through membrane for different pore sizes and driving pressures at the minimum pore aspect ratio l/a which makes wetting thermodynamically unfavorable. Contact angle of 120°, NaCl concentration of 0.62 M, and 40% membrane porosity are assumed. (a) $T = 20$°C, $\sigma = 0.5$; (b) $T = 50$°C, $\sigma = 0.5$; (c) $T = 20$°C, $\sigma = 1.0$; (d) $T = 50$°C, $\sigma = 1.0$.

Figure 11. Fabrication of osmosis membranes with nanoscale vapor traps. a, Schematic illustration of membrane with short hydrophobic nanopores that trap vapor. b, Schematic of fabrication processes. i) porous alumina membrane soaked with photoresist AZ5214, ii) solvent evaporation on hot plate, iii) air plasma treatment for photoresist etching, iv) silanization on exposed alumina surface with perfluorodecyltrichlorosilane (FDTS), v) removal of residual photoresist. c, The fabricated membranes have a hydrophobic top surface (left) and hydrophilic bottom surface (right). d, SEM images of cross-section of

nanopores after no plasma treatment (left), 2 h (middle), 9 h (right) of treatment, illustrating control of pore length for hydrophobic modification. Scale bar is 300 nm. e, SEM image of membrane after 2 h plasma treatment. Scale bar is 500 nm. f, Photoresist etch depth for different plasma treatment periods. Error bars represent ±S.D.

Figure 12. Aspect ratio (AR) distribution of nanopores after plasma treatment for different time periods.

Figure 13. a, b SEM images of bare (a) and annealed (b) alumina membrane surface after dipping in boiling water for 2 h. Scale bar is 2 μm in (a) and 400 nm (b), respectively. c, d XRD spectrum for bare (c) and annealed (d) alumina membranes. Bare alumina reveals amorphous form while annealed one shows γ-alumina. Circles indicate peaks of γ-alumina.

Figure 14. Photographs of hydrophilic side surface of membrane and water droplets on the surface before (a, c) and after (b, d) UV exposure and rinsing with ammonium hydroxide solution. The droplet completely spreads on the hydrophilic side after the treatment (d).

Figure 15. Verification of membrane integrity. a, SEM images of cross-section of nanopores after 2 h plasma treatment (left) and after immersion of the fabricated membrane in 3 nm gold nanoparticle solution (right) show co-localization of the nanoparticles with the extent of photoresist etching. Scale bar is 200 nm. b, Confocal microscopy of the membrane exposed to two different fluorescence dye solutions (Alexa 633 and Alexa 488 in deionized water) on either sides of membrane reveals a distinct interface with lack of mixing. Scale bar is 5 μm. c, Environmental SEM image of fabricated membrane showing hydrophilic and hydrophobic surfaces. Arrow indicates the non-wetted region appearing as a thin line corresponding to the hydrophobic modification. Scale bar is 100 μm.

Figure 16. a, Schematic diagram of setup for impedance measurement. Electrical potential is given $V = V_0 \sin(2\pi ft)$ with $V_0 = 20$ mV, $f = 50$ mHz. b, Example of current profile for bare

alumina membrane without any treatment, fabricated membrane with hydrophobic nanopores made with 1 h and 18 h plasma etching, respectively.

Figure 17. a, Resistance change with time for a membrane with hydrophobic nanopores made by 12 h plasma etching. b, Variation of the defect rate (i.e. fraction of wetted pores) with time.

Figure 18. a, Schematic diagram of forward osmosis experiment setup. The deionized water in the right diffusion cell is drawn to the other cell with draw solution (KCl). Magnetic stir bars enhance mixing of solutions and minimize concentration polarization. b, Measured mass flux through a membrane for different osmotic pressure differences using 0.2, 0.5, 1, 1.5, and 2 M KCl as draw solutions, at a temperature of 25°C. Red dotted line is drawn as a guide for the eyes. Error bars represent ±S.D. for three different measurements on one membrane.

Figure 19. a, Forward osmosis experimental setup with diffusion cells containig 1M KCl draw solution (left) and 2mM Allura Red dy in DI water (right). b, UV-vis spectra show rejection of Allura Red dye. Black, 1 M KCl solution; red, Allura Red solution in 1 M KCl assuming zero rejection of dye mimicking how the draw solution would look if water were transported without dye rejection; blue, actual draw solution. d, 2 mM Allura Red solution in deionized water drawn across the membrane by the draw solution (left), Allura Red solution in 1 M KCl assuming zero rejection of dye mimicking how the draw solution would look if water were transported without dye rejection (middle), actual solution in draw solution cell after experiment showing dye rejection (right).

Figure 20. Scaling behaviour of the measured water flux. a, Schematic of resistance models for "short" and "long" nanopores. R_i, interfacial resistance; R_t, transmission resistance; R_h, hydrodynamic resistance. b, Variation of mass flux with AR for different KCl concentrations of draw solution measured at 39.0±0.3°C. c, Scaling of the measured mass flux normalized by maximum flux ($S_A - S_B$) with AR^{-1}. Note that as AR decreases, the normalized flux

deviates from the solid line 2.12/AR corresponding to an inverse scaling expected in the case of long pores, plotted for pressure inside nanopore, p, of 0.5 bar. The shaded area indicates the possible range corresponding to $0.2 \leq p \leq 0.8$ bar (See Section 4.1.2).

Figure 21. Transmission probability $\eta^{90,\ 99}$ for Knudsen regime and modified transmission probability η_{eff} for viscous regime. a = 40 nm, M = 1.8 x 10^{-2} kg/mol, T = 300 K, D_{12} = 2.56 x 10^{-5} m^2/s and p = 1 bar are used for the calculation

Figure 22. a, Dependence of the measured mass flux on temperature for AR = 42.1±2.1. b, Temperature dependence of total resistance for "long" pores with AR of 42.1±2.1 and for "short" pores with AR of 9.6±0.7. Dotted lines are linear fits to data averages to guide the eyes. Vertical error bars in all panels represent ±S.D. corresponding to measurements on 3 to 5 different membranes for each data point. Horizontal error bars in all panels represent ±S.D. for AR as described in Appendix D.

Figure 23. Regime of interface-governed transport. a, Mass flux normalized by the maximum mass flux corresponding to zero interfacial resistance (R_i = 0) for different concentrations of draw solution reveals a marked departure at smaller aspect ratios. Temperature is 39.0±0.3 °C. Green line indicates ideal normalized flux for σ = 1 as a guide for the eyes. Black dotted line denotes the theoretically predicted normalized mass flux for a condensation coefficient of 0.23. b, Ratio of interface resistance to transmission resistance for different AR at a temperature of 39.0±0.3 °C, obtained from data shown in panel a. Vertical error bars in all panels represent uncertainty combining S.D. of data points and the effect of uncertainty in pressure inside the nanopores, p (See Appendix D). Each data point was obtained from measurements on 3 to 5 different membranes. Horizontal error bars in all panels represent ±S.D. for AR as described in Appendix D.

Figure 24. Estimated condensation coefficients for different AR at a temperature of 39.0±0.3 °C, obtained from data shown in Figure 23 panel a (c) and for different temperatures, obtained

from flux measurements on membranes with AR of 9.6±0.7 (d). Vertical error bars in all panels represent uncertainty combining S.D. of data points and the effect of uncertainty in pressure inside the nanopores, p (See Appendix D). Each data point was obtained from measurements on 3 to 5 different membranes. Horizontal error bars in all panels represent ±S.D. for AR as described in Appendix D.

Figure 25. Effect of salt concentration on condensation coefficients. Nanopores with average aspect ratio of 11.0 were used at 25°C. a, Mass flux for different KCl concentrations, normalized by membrane porosity and by difference of evaporation rate across the membrane; b, Estimated condensation coefficients from the measured mass flux. The error bars denote ±S.D. including the effect of uncertainty in pressure inside the nanopores, p (See Appendix D).

Figure 26. Effect of interchanging of halogen ions on condensation coefficients. Nanopores with average aspect ratio of 8.5 were used with draw solutions of 0.5 M KCl and 0.5 M KI, respectively, at 30°C. a, Mass flux for different KCl concentrations, normalized by membrane porosity and by difference of evaporation rates across the membrane; b, Estimated condensation coefficients from the measured mass flux. The error bars denote ±S.D. including the effect of uncertainty in pressure inside the nanopores, p (See Appendix D). The condensation coefficients from KCl and KI are not significantly different based on the Student t-test (p value > 0.05).

Figure 27. Resistance networks for estimating the effect of meniscus curvature on transmission probability using the radiation heat transfer analogy. A_c, A_w, A_f, and A_p denote the area of cross section of pore, pore wall, menisci at feed and permeate sides, respectively. F_{cc} and F_{cw} indicate view factors between the two menisci, and a meniscus and the pore wall, respectively, for flat interfaces. F_{fp}, F_{fw} and F_{pw} denote view factors between the menisci at feed and permeate sides, the meniscus at feed side and the pore wall, and between the

meniscus at permeate side and the pore wall, respectively, assuming that the meniscus on the feed side is curved (maximum possible curvature at a contact angle of 120°) and that on the permeate side is flat. F_{cc} and F_{cw} indicate view factors between the two menisci, and from a meniscus to the pore wall, respectively, for flat interfaces. F_{fp}, F_{fw} and F_{pw} denote view factors from the meniscus on the feed side to that on the permeate side, from the meniscus on the feed side to the pore wall, and from the meniscus on the permeate side to the pore wall, respectively, assuming that the meniscus on the feed side is curved (maximum possible curvature at a contact angle of 120°) while that on the permeate side is flat.

Figure 28. Decrease in vapor pressure difference across a membrane with thermal conductivity of 0.27 W/m-K. Applied pressure of 50 bar, temperature of 50°C, NaCl concentration of 0.62 M, condensation probability of 1.0, and porosity of 40% are assumed. Dashed line indicates the vapor pressure difference variation at minimum aspect ratio $(l/a)_{min}$.

Figure 29. Effect of air pressure inside the nanopores. a, b, c Mass flux normalized by that with zero interface resistance for (a) p = 0±0.0 bar; (b) p = 0.5±0.3 bar; (c) p = 1±0.0 bar. d, e, f Ratio of R_i and R_t for different aspect ratios with (d) p = 0±0.0 bar; (e) p = 0.5±0.3 bar; (f) p = 1±0.0 bar. g, h, i Estimated condensation coefficients for different aspect ratios with (g) p = 0±0.0 bar; (h) p = 0.5±0.3 bar; (i) p = 1±0.0 bar. j, k, l, Estimated condensation coefficients for different temperatures with (j) p = 0±0.0 bar; (k) p = 0.5±0.3 bar; (l) p = 1±0.0 bar.

Figure 30. Fabrication method using alkanethiol self-assembled monolayers. a, E-beam evaporation of gold on rotating membrane with an angle θ. b, Schematic diagram of self-assembled monolayers formed based on thiol-gold bonding. c, Water droplet on the fabricated membrane

Figure 31. Defect characterization using Fluo-4. a, Schematic diagram of setup with a membrane. 0.5 mM Fluo-4 solution on the top side and 10 mM $CaCl_2$ solution on the bottom side are

placed under AC electric field. b, Snapshot of the experimental setup on fluorescence microscope. c, Fluorescence image of 'leaky' membrane. d, Corresponding Fourier transformed map for fluorescence light intensity. e, Fluorescence image of 'low defect' membrane. f, Corresponding Fourier transformed map for fluorescence light intensity. g, Time trace of fluorescence light intensity normalized by a maximum intensity at a specific 'leaky' pore.

Chapter 1. Introduction

1.1. Background and motivation

The increasing demand and depleting resources of water have worsened the fresh water scarcity problem, and the number of people facing water shortage is expected to quadruple by 2025[1]. The scarcity of fresh water is expected to become more serious in developing countries where many diseases and deaths are attributed to the poor quality of water[2], and also in Middle East and North African countries that are suffering from lack of renewable fresh water[2, 3].

In addition, the projected 40–50% growth in human population over the next 50 years, coupled with industrialization and urbanization, will result in an increasing demand on the available water resources[4]. While economic use and recycling of water for human and animal consumption can mitigate the problem to some extent[5], alternative sources of clean water are required to address this growing need. The fact that more than 97% of water in the world exists as a form of seawater or brackish water naturally leads to desalination as a promising alternative source of water. Currently, the source of feed water for desalination stems from seawater (58.9%), brackish water (21.2%), surface water and saline wastewater for the rest[6]. The capacity of desalination is growing with rate of about 55% per year and is expected to reach 100 million m^3 / day in 2015[6].

Membrane-based reverse osmosis (RO), thermal-based multi-stage flash (MSF), and multi-effect distillation (MED) are currently the major desalination technologies and constitute over 90% of the global production of desalinated water[6, 7]. As of 2012, membrane processes account for 63.7% of the total desalination capacity and thermal-based processes for 34.2%[6]. MSF is the primary thermal-based desalination technology and it accounts for about 26% of current global desalination capacity[6]. In this method, feed saline water is introduced and evaporated by latent heat supplied, typically under vacuum to reduce the boiling temperature. The generated vapor condenses to be harvested as fresh water product, while the latent heat released during the

condensation is reused to preheat the feed water. Since the thermal evaporation occurs in relatively high temperature > 90°C, there is a high chance of scaling formation which reduces heat transfer coefficient, although this scaling problem in MSF is alleviated than MED[2]. In addition, although a significant portion of energy is reused by the preheating and as a result 10 – 20 times less energy than latent heat (~2,200 kJ/kg) is actually needed, the thermal-based desalination technologies such as MSF or MED still require significantly large amount of energy compared to the thermodynamic minimum energy of separation for typical seawater (3.5 kJ per kg of fresh water for 50% recovery)[5]. However, since the required energy is almost constant regardless of feed water salinity, the thermal-based approaches are economical and widely used in Middle East Asia where the salinity of seawater is relatively high and the cost of heat energy is also low[2, 8].

Reverse osmosis (RO) is being increasingly adopted worldwide as an energy efficient technology for water purification[8]. As of 2012, RO accounts for 63.7 % of the global desalination capability[6]. In RO process, saline feed water is pressured against a semi-permeable membrane which allows only water to pass while rejecting salts. Since the permeability and therefore production rate are determined by the thickness of active selective layers, development of asymmetric membranes[9] and polyamide composite membranes prepared by interfacial polymerization[10, 11] have realized submicron thickness of active layers (< 500 nm) and enabled RO to be competitive with thermal processes for large-scale desalination applications. RO is more economical in the aspect of energy cost compared to thermal processes that require more energy due to the latent heat of water[2]. Membrane-based RO has almost reached thermodynamic efficiencies for desalination[12]. The state-of-the-art RO plants requires less than 5.7 kJ/kg with recovery ratio of 42%[5] while the theoretical minimum energy based on 50% recovery is 3.5 kJ/kg. This high-energy efficiency is primarily attributed to improvement of energy recovery units which utilize the rejected brine pressure to pre-pressurize the feed water[5, 13, 14]. But RO membranes suffer from some persistent

issues including fouling, scaling, and requirement of large membrane areas due to limited flux[8]. Although chlorine is one of the simplest and most economical ways of controlling biofouling, polyamide – the most widely used selective RO membrane material – suffers from low tolerance to chlorine and therefore degrades by exposure to chlorine[15-17]. Low rate of boron rejection of RO process is also another issue and conventional RO systems rarely satisfy the boron concentration level that World Health Organization (WHO) guideline recommends (1 mg/L or less)[18, 19]. In practical RO applications, therefore, the permeate has been diluted with other source with lower boron concentration[19] or multi-stage RO systems at different pH's are often required to remove boron[20]. A large portion of boron exists as non-ionic boric acid at pH7 which is harder to remove while it becomes ionized at higher pH[20]. Although boron rejection at pH 11 reaches 98 – 99%, operation at pH larger than 10 is not recommended due to salt precipitation which increases risk of scaling on membranes[21]. The cost involved in the multi-stage RO obviously could be reduced by development of novel RO membranes capable of rejecting boron at neutral pH. Furthermore, there is a trade-off between membrane area and efficiency due to the limited flux per unit area, and between selectivity and permeability, which is limited by material properties[22]. Further improvements in RO membranes that enable larger flux without compromising selectivity and have increased resistance to fouling are therefore needed.

Advances in nanofluidics promise membranes with improved control over their nanostructure, better selectivity, or decreased viscous losses[23-27]. For example, membranes incorporating carbon nanotubes that allow flow of water with low viscous loss are being developed for desalination of water[23, 28]. New nanofluidic transport mechanisms thus have the potential to make a significant impact on energy conversion and clean water technologies through development of better membranes. In this thesis, we suggest a new type of RO membrane that uses vapor-phase transport through hydrophobic nanopores for desalination of water. We first theoretically explore transport of water through a hydrophobic nanopore using a probabilistic model that incorporates

rarefied gas dynamics, ballistic transport, and emission and reflection of water molecules at liquid-vapor interfaces. We then expand the model to transition regime where molecular diffusion coexists with the rarified gas transport. Effect of nanopore geometry, salinity, temperature, applied pressure, and interfacial reflection probability on the transport of water molecules through the nanopore are explored. We further realize membranes consisting of hydrophobic nanopores to experimentally study the transport with the various above-mentioned conditions. We show that transport of vapor involved in two-phase flow at the nanoscale is determined by interplay between diffusion across nanopores and evaporation/condensation resistances at the two-phase interface. Finally, the significant potential of this new approach for desalination is shown and discussed.

Chapter 2. Theoretical investigation of vapor phase transport of water through hydrophobic nanopores[1]

2.1. Concept of vapor trapping membrane for desalination

We propose a membrane that consists of hydrophobic nanopores that trap vapor by virtue of their hydrophobicity and small size, separating the saline feed water on one side and the desalinated permeate water on the other side (Figure 1). Two water menisci are formed on either side of the pore and mass transfer occurs only in the form of evaporation at one meniscus, transport of water vapor through the nanopore, and condensation at the other meniscus. The salt concentrations and pressures on either side of the nanopore as well as the temperature determine the equilibrium vapor pressure at each meniscus. If a pressure that exceeds the osmotic pressure is applied on the feed water (saline) side, a vapor pressure difference is generated across the nanopore, resulting in a net flux of water across the pore through evaporation at one interface and condensation at the other interface. Since transport occurs in the vapor phase, the process is selective and only allows

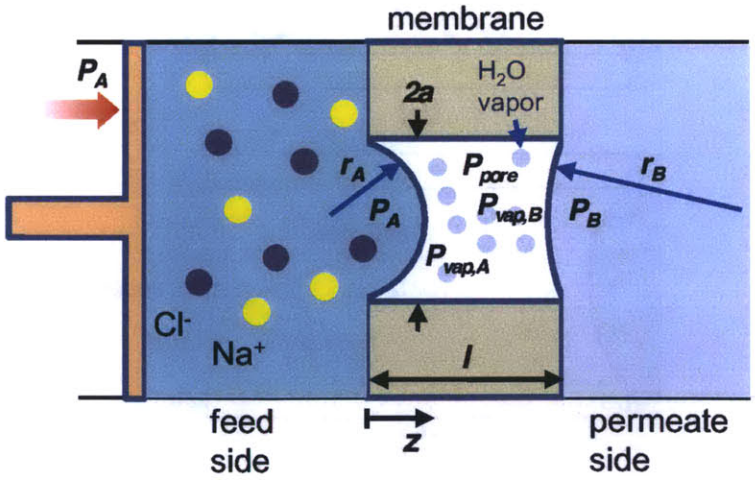

Figure 1. Schematic diagram of a hydrophobic nanopore with liquid-vapor interfaces on either side. Application of pressure greater than the osmotic pressure on the saline water side results in vapor-phase transport of water across the nanopore.

[1] This chapter can be referred to Lee et al.[29]

water molecules to cross the nanopore. Furthermore, the nanopore is isothermal due to the small length scale and conduction through the nanopore wall material; thus energy required for evaporation is immediately recovered by condensation.

Transport of water vapor across a vapor-trapping membrane with water on either side has been used for desalination in a technique known as direct contact membrane distillation[30-32]. However, this method relies on a temperature difference to drive transport of water, and is subject to high thermal losses and the actual temperature difference across the membrane is smaller than the bulk temperature difference due to temperature polarization. The present approach replaces the temperature difference by a pressure difference, thereby eliminating thermal losses and temperature polarization issues.

Generally, gas transport in a pore occurs by four different mechanisms: Knudsen diffusion,

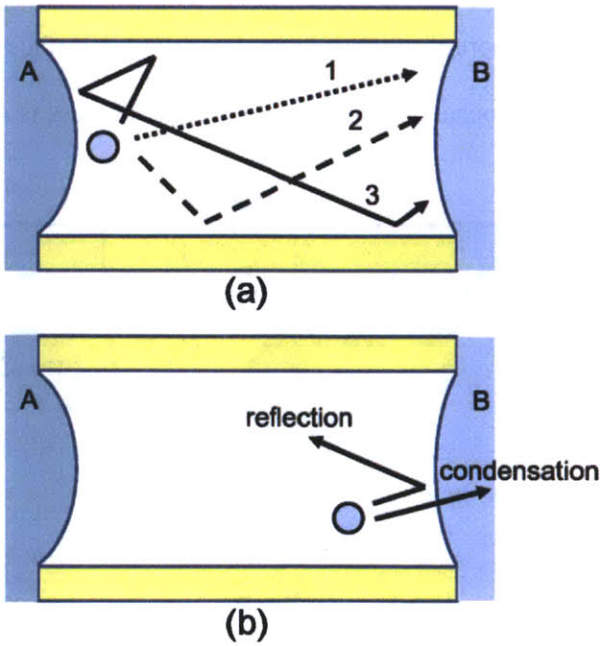

Figure 2. Schematic diagram showing some potential trajectories of molecules inside the nanopore. (a) trajectories the molecule takes from meniscus A to B. (1) meniscus A → meniscus B (ballistic transport), (2) meniscus A → wall → meniscus B, (3) meniscus A → wall → meniscus A → wall → meniscus B; (b) Upon reaching meniscus B, the molecule can either condense or undergo reflection.

molecular diffusion, viscous flow, and surface diffusion[33, 34]. The applied pressure that should be larger than osmotic pressure, i.e., 30 bar for seawater, necessitates small pore diameters less than ~50 nm to prevent wetting. Since the mean free path for water vapor at 20-50°C is about 1-5μm, we assume that vapor-phase transport through the pores occurs primarily by Knudsen diffusion. Studies of wetting properties of carbon nanotubes show sharp transitions between non-wetted and wetted states[24, 35]. In addition, the water vapor adsorption on pure hydrophobic surfaces such as silicalite-1 and beta zeolites is negligibly small[36, 37]. Membrane distillation which incorporates intrinsically hydrophobic porous membranes does not have severe wetting issues from water adsorption in the hydrophobic pores. Furthermore, adsorption of water molecules on hydrophobic surfaces is confined to hydrophilic defects[38-40]; adsorption on such a defect and subsequent emission of a molecule is equivalent to a scattering event from the wall. When hydrophobic and hydrophilic surfaces are patterned in close proximity, it has been shown that water vapor condenses on the hydrophilic patterned sites in preference to the hydrophobic ones[39]. Due to the small length scale of the nanopore, water vapor may be expected to condense on the menisci rather than on the pore surface. In this study, we therefore assume that transport of water through the nanopore by surface flow is negligible as compared to Knudsen diffusion. While Knudsen diffusion theory is known to be valid for the pore diameters down to 2 nm,[41] the classical Knudsen diffusion coefficient is defined only in the limit of an infinite pore length. The predicted Knudsen flux diverges to infinity as the pore length approaches zero; thus, calculation of flux in pores of finite length requires a different approach. Similarly, a model for transport through a hydrophobic pore must also consider the effects of the menisci.

In this chapter, we develop a general model based on a transmission probability framework that accounts for finite nanopore length, rates of evaporation and condensation, as well as reflection and condensation probabilities at the liquid-vapor interfaces (Figure 2).

2.2. Microscopic picture of water transport across liquid/vapor interface

The condensation process of vapor molecules into liquid-phase can be explained by two steps[42-44]. The impinging vapor molecules are first adsorbed onto the surface and thermally equilibrate with the mean energy of liquid molecules at the surface. The fraction of the impinging molecules that achieve thermal equilibrium is called thermal accommodation coefficient. The experimentally measured values ranges between 0.7[45] and 1.0[42, 46, 47] although the majority of literature indicates that the thermal accommodation coefficient of water is likely to be unity. The adsorbed molecules are then either desorbed back to vapor-phase or absorbed into the liquid-phase. The fraction of the impinging vapor molecules that are converted to liquid-phase is called condensation coefficient (also called mass accommodation coefficient). The measurement of condensation coefficient of water has been much more challenging than the thermal accommodation coefficient. Although numerous experimental studies have been conducted to measure the condensation coefficient, the reported values are scattered over three orders of magnitude (0.001 – 1)[48, 49]. Extensive reviews by Marek and Straub[48] and Eames et al.[49] concluded that the water surface free from any contamination and surfactants should have a relatively large value of condensation coefficient, and the values such as lower than 0.1 that have been experimentally measured seemed unlikely. As a rule of thumb, we take condensation coefficient of water between 0.5 and 1. One illustration based on thermal accommodation of unity and condensation coefficient of 0.7 as an example would be that although all vapor molecules impinging on the liquid/vapor interface adsorb and reach thermal equilibrium with the liquid surface, 30% of them return to vapor-phase and 70% condense. From the heat transfer point of view, 70% of the vapor molecules carry the latent heat to the liquid phase, while 30% of them also transfer some amount of heat by dissipating their kinetic energy during the thermal equilibration process.

2.3. Probability of molecular transport across a nanopore

Let $\varphi_{A,B}$ be defined as the probability that a molecule emitted (by evaporation) from meniscus A condenses at meniscus B. If the rates of evaporation at each meniscus are known, the net flux of water through the nanopore can be calculated in terms of $\varphi_{A,B}$ (which equals $\varphi_{B,A}$ by symmetry). $\varphi_{A,B}$ can be further expressed in terms of two distinct probabilities: (a) η, the probability with which a molecule that leaves one meniscus arrives at the other meniscus also known as the transmission probability, and (b) σ, the condensation coefficient.

To calculate $\varphi_{A,B}$, we consider all possible ways in which a molecule emitted from meniscus A finally condenses at either meniscus A or B (Figure 3). A molecule which has evaporated from meniscus A is transported to the other meniscus B with transmission probability η. This transmission probability includes the cases where the molecule arrives at meniscus B after collision(s) with the wall and without any collision with the pore wall. However, this molecule also can return to meniscus A with probability $1 - \eta$ after scattering from the wall. When a molecule leaves one meniscus and arrives at the other meniscus or back to the same meniscus (after scattering event(s) from pore walls), we call the transport event as one "cycle". Therefore the molecule will reach either meniscus A or B after each cycle. This molecule will then condense with a probability σ on the meniscus it arrived at, or be reflected with a probability β (= $1 - \sigma$). If the molecule is reflected from the meniscus A or B, it will start its flight again from the meniscus it was reflected on. We define A_n as the probability that a molecule emitted from meniscus A arrives back at meniscus A after n cycles, and B_n as the probability that a molecule emitted from meniscus A arrives at meniscus B after n cycles. Therefore the probability that a molecule condenses on meniscus A after n cycles is $(1 - \beta)A_n$, and that on meniscus B is $(1 - \beta)B_n$. A molecule reflected from meniscus A with the probability βA_n will start its $n+1^{th}$ cycle flight toward meniscus B, and vice versa.

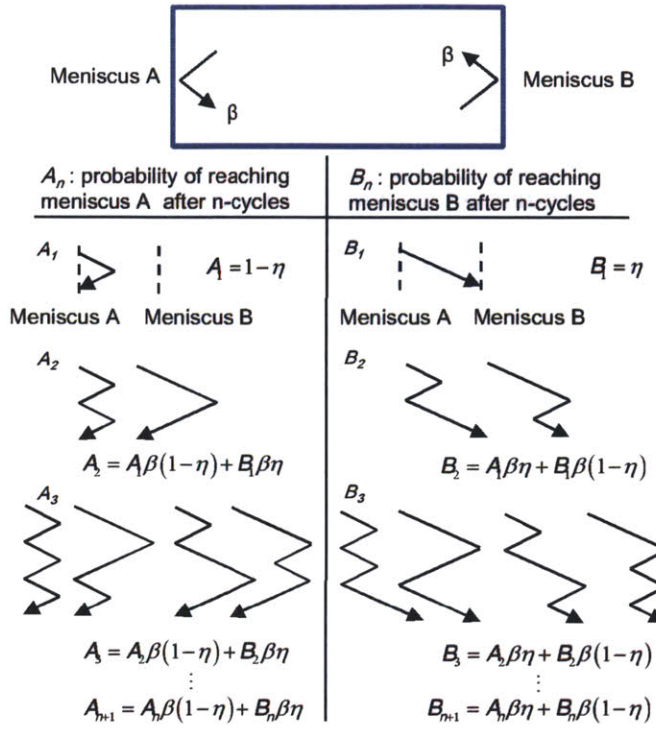

Figure 3. Possible paths and probabilities of molecules emitted from meniscus A until they condense at either meniscus A or B. In the arrow diagrams, the leftmost position indicates meniscus A, the center position indicates scattering from the pore walls, and the rightmost position indicates meniscus B. For example, in the diagram for A_2, the molecule that leaves meniscus A can arrive at meniscus A (after scattering from the pore walls), be reflected from the meniscus A, and arrive again at A by a similar process (left), or the molecule emitted from A can reach meniscus B, be reflected from meniscus B, and arrive at meniscus A (right).

As shown in Figure 3, if a molecule arrives at meniscus A at the $n+1^{th}$ cycle, there are two paths that it could have taken after the n^{th} cycle. The first path is that the molecule arrived at meniscus A and was reflected from it, and left meniscus A, but was scattered from the wall, and finally reached meniscus A. The probability of this path is $A_n\beta(1-\eta)$. The second path is that the molecule reached meniscus B and was reflected, and transported back to meniscus A. The corresponding probability is $B_n\beta\eta$. Therefore, A_{n+1} can be obtained as:

$$A_{n+1} = A_n\beta(1-\eta)+B_n\beta\eta. \qquad (1)$$

With similar reasoning, B_{n+1} is also calculated as

$$B_{n+1} = A_n\beta\eta + B_n\beta(1-\eta). \tag{2}$$

Then, the following relation can be obtained:

$$A_n + B_n = \beta\left(A_{n-1} + B_{n-1}\right) = \cdots = \beta^{n-1}\left(A_1 + B_1\right) = \beta^{n-1}. \tag{3}$$

The probability $\varphi_{A,A}$ and $\varphi_{A,B}$ that a molecule that has evaporated from meniscus A finally condenses on meniscus A and B, respectively, can now be expressed as follows:

$$\varphi_{A,A} = (1-\beta)\sum_{n=1}^{\infty} A_n, \tag{4}$$

$$\varphi_{A,B} = (1-\beta)\sum_{n=1}^{\infty} B_n. \tag{5}$$

Then, it can be readily shown that $\varphi_{A,A} + \varphi_{A,B} = 1$. This simply means that molecules evaporated from a meniscus must eventually condense either on meniscus A or B. When we solve for A_n, the following relation is obtained:

$$A_{n+1} = A_n\beta(1-\eta) + B_n\beta\eta = \alpha A_n + \beta^n\eta, \tag{6}$$

where $\alpha = \beta(1-2\eta)$. Therefore, A_n can be expressed as follows:

$$\begin{aligned} A_n &= \alpha^{n-1}A_1 + \alpha^{n-2}\beta\eta + \alpha^{n-3}\beta^2\eta + \mathrm{L} + \alpha\beta^{n-2}\eta + \beta^{n-1}\eta \\ &= \alpha^{n-1}A_1 + \beta^{n-1}\eta\frac{1-\left(\frac{\alpha}{\beta}\right)^{n-1}}{1-\frac{\alpha}{\beta}}. \end{aligned} \tag{7}$$

Then we can calculate $\varphi_{A,A}$ and $\varphi_{A,B}$:

$$\varphi_{A,A} = (1-\beta)\sum_{n=1}^{\infty} A_n = 1 - \frac{\eta}{2\eta\beta - \beta + 1}, \tag{8}$$

$$\varphi_{A,B} = 1 - \varphi_{A,A} = \frac{\eta}{2\eta\beta - \beta + 1}. \tag{9}$$

Using the fact that $\beta = 1 - \sigma$ (by definition), we can write

$$\varphi_{A,B} = \frac{\eta}{2\eta(1-\sigma) + \sigma}. \tag{10}$$

For practically encountered contact angles up to 120°, we can neglect the effect of meniscus curvature on η and assume the pore geometry to be cylindrical (see Appendix A). We further assume that the whole system is isothermal, which is a reasonable approximation even in the case of membrane materials with a relatively poor thermal conductivity (see Appendix B). With these assumptions, we can take advantage of the fact that the transmission probability η in Equation (10) is equivalent to the transmission probability across a pore of finite length. Transmission probability was first introduced by Clausing[50] to obtain pressure-driven flux of a rarefied gas through a pore of finite length. Here, we use the transmission probability η as calculated by Berman[51] for a pore of finite length under the diffuse scattering assumption (Figure 4). η is a function only of the pore aspect ratio l/a with a maximum value of 1 occurring at zero pore length, corresponding to ballistic transport. η decreases with increasing l/a and converges to $8/3(l/a)$ for long pores, which is consistent with Knudsen diffusion.

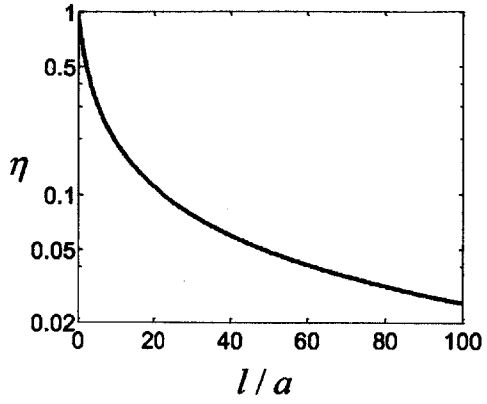

Figure 4. Probability of transmission of a molecule across a cylindrical nanopore with length l and radius a (from Berman[51]).

As mentioned in Section 2.2, the value of σ is difficult to predict and must be obtained empirically. Following the review of Eames et al.[52], condensation coefficient of water is assumed to be between 0.5 and 1 in this study. In addition, it is also assumed that σ is independent of curvature of meniscus and salt concentration. The dependency of condensation coefficient on salt concentrations and also other parameters such as temperature and ion types will be discussed in Section 4.6.

2.4. Derivation of mass flux across the nanopores

2.4.1. Change in equilibrium vapor pressure

While we obtained the transport probability for a molecule evaporated from one side to condense on the other side of the nanopore, the total net flux across the nanopore depends on the rate of evaporation from each meniscus. The rate of evaporation is related to the vapor pressure and probability of condensation σ. The rate of absorption of water molecules at the liquid-vapor interface is equal to the product of the rate of incidence and the probability of condensation,

which, at equilibrium, must equal the rate of evaporation. For temperatures up to 50°C, the density of water vapor deviates from that predicted by kinetic theory of gases by less than 0.4%; we therefore use the kinetic gas theory to estimate the rate of incidence. This is known as the Hertz hypothesis[52, 53], which gives the rate of gross evaporation per unit area at each meniscus, i.e., $\dot{m}_{e,i}$ (i = A or B) as:

$$\dot{m}_{e,i} = \sigma S_i = \sigma \sqrt{\frac{M}{2\pi R_g T_i}} P_{vap}\left(T_i, P_i, C_i\right), \tag{11}$$

where $S_{A(B)}$ is the theoretical maximum rate of evaporation from side A (or B) assuming a condensation coefficient of unity, i.e., $S_i = \sqrt{M / 2\pi R_g T_i} P_{vap}\left(T_i, P_i, C_i\right)$. Here, P_{vap} is the equilibrium vapor pressure of water at meniscus A (or B) as a function of temperature T_i, pressure P_i and salt concentration C_i. R_g is the universal gas constant (8.31 J/mol·K) and M is the molecular weight of water (1.8×10^{-2} kg/mol).

The equilibrium vapor pressure P_{vap} for different temperature, pressure and salt concentration can be derived by relating chemical potential of water in saline solution with that in vapor phase. The chemical potential of water $\mu_w^{(l)}$ in saline solution is given as[54, 55]

$$\mu_w^{(l)} = \mu_w^{*,(l)} + R_g T \ln a_w = \mu_w^{*,(l)} + R_g T \ln \gamma_w x_w, \tag{12}$$

where $\mu_w^{*,(l)}$ is the chemical potential of pure water at a reference state as a function of temperature and pressure. Activity of the water a_w can be decomposed into activity coefficient γ_w and mole fraction x_w of water in the solution. For water vapor in gas-phase, the chemical potential is given as[56]

$$\mu_w^{(g)} = \mu_w^{\theta,(g)} + R_g T \ln \frac{f_w}{P^0}, \tag{13}$$

where $\mu_w^{\theta,(g)}$ is a chemical potential of pure water vapor at a reference state as a function of temperature, f_w is fugacity of water and P^0 is a standard pressure which is typically taken as 1 bar[55]. At moderate pressure, the water vapor behaves as ideal gas. In that case, the fugacity of the water vapor can be taken as vapor pressure P_{vap} in the gas mixture.

If we imagine a gas mixture including water vapor above saline solution at equilibrium, the chemical potential of water in both phases must be equal. Therefore,

$$\begin{aligned}\mu_w^{(l)} &= \mu_w^{*,(l)} + R_g T \ln a_w \\ &= \mu_w^{\theta,(g)} + R_g T \ln \frac{P_{vap}}{P^0} = \mu_w^{(g)},\end{aligned} \tag{14}$$

and for pure water in equilibrium with vapor,

$$\mu_w^{(l)} = \mu_w^{*,(l)} = \mu_w^{\theta,(g)} + R_g T \ln \frac{P_{vap}^0}{P^0} = \mu_w^{(g)}, \tag{15}$$

where P_{vap}^0 is equilibrium vapor pressure of pure water as a function of temperature and pressure. Rearrangement of the two above equations lead to the water vapor pressure in equilibrium with saline solution as[55]:

$$P_{vap} = a_w P_{vap}^0, \tag{16}$$

where a_w is activity of water in the solution. The osmotic pressure Π is given as a function of water activity[57],

$$\Pi = -\frac{R_g T}{V_m} \ln a_w, \tag{17}$$

Substitution of Equation (17) into (16) leads to:

$$P_{vap} = P_{vap}^0 \exp\left(-\frac{\Pi V_m}{R_g T}\right). \tag{18}$$

When a pressure drop P is applied across the meniscus, vapor pressure is elevated according to Kelvin's equation[58]:

$$P_{vap}^{\kappa} = P_{vap} \exp\left(\frac{PV_m}{R_g T}\right). \tag{19}$$

Substitution of Equation (18) into (19) leads to:

$$P_{vap}^{\kappa} = P_{vap}^{0} \exp\left[\frac{(P-\Pi)V_m}{R_g T}\right]. \tag{20}$$

which is also known as Kohler equation[59, 60]. For convenience, we use P_{vap} for equilibrium vapor pressure instead of P_{vap}^{κ} from now on. Under isothermal condition as in the present study, the difference in equilibrium vapor pressure is then given as:

$$\begin{aligned} P_{vap,A} - P_{vap,B} &\approx P_{vap}^{0}\left[\frac{(\Delta P-\Delta\Pi)V_m}{R_g T} + \left(\frac{V_m}{R_g T}\right)^2 \frac{P_A^2 - P_B^2 + \Pi_A^2 - \Pi_B^2 + 2(P_A\Pi_A - P_B\Pi_B)}{2}\right], \\ &\approx \frac{(\Delta P-\Delta\Pi)V_m}{R_g T} P_{vap}^{0} \end{aligned} \tag{21}$$

where $\Delta P = P_A - P_B$ and $\Delta\Pi = \Pi_A - \Pi_B$. Discarding the second-order term on the right-hand side results in an error of at most ~3.5% even for $|\Delta P - \Delta\Pi| = 100$ bar.

2.4.2. Derivation of mass flux based on probabilistic framework

At equilibrium, the pressure difference across the nanopore (ΔP) is equal to the osmotic pressure difference ($\Delta\Pi$). Increasing the pressure difference across the nanopore beyond the osmotic pressure difference results in $P_{vap,A} > P_{vap,B}$ and net transport of water across the nanopore. Knowing the rate of evaporation (Equations (17) – (19)) and the probability $\varphi_{A,B}$ that a water

molecule emitted by evaporation condenses on the other meniscus (Equation (10)), the net mass flux through a membrane consisting of the nanopores with a porosity ε is given by

$$\dot{m} = \varepsilon\left(\varphi_{A,B}\dot{m}_{e,A} - \varphi_{B,A}\dot{m}_{e,B}\right) = \varepsilon\varphi_{A,B}(\dot{m}_{e,A} - \dot{m}_{e,B})$$
$$= \frac{\varepsilon\sigma\eta}{2\eta(1-\sigma)+\sigma}\sqrt{\frac{M}{2\pi R_g T}}\left(\frac{\Delta P - \Delta\Pi}{R_g T}V_m\right)P^0_{vap}(T) \quad (22)$$

Seawater (or brackish water) is characterized in terms of total dissolved solids (TDS) ranging from 15,000 to 50,000 ppm (corresponding to 0.26 M to 0.90 M NaCl), with the TDS of standard seawater being 35,200 ppm (0.62 M NaCl solution). TDS for brackish water ranges from 1,500 to 15,000 (0.026 M to 0.26 M NaCl solution). The corresponding osmotic pressure is about 13 to 44 bar for sea water and 1.3 to 13 bar for brackish water, although seawater with the same TDS as that of NaCl solution has a lower osmotic pressure due to presence of higher mass solutes[8]. RO plants for desalination of sea water typically operate at pressures ranging from around 55-80 bar[8].

2.4.3. Heat transfer analogy for calculation of transport through the nanopore

An alternative way to obtain the net mass flux is by using an analogy from radiation heat transfer[61]. As shown in Figure 5, the mass transport system in a nanopore can be modeled as three resistances in series due to reflection from the two menisci and scattering from the pore wall. While $S_{A(B)}$ is the theoretical maximum gross evaporation rate through meniscus A(B), the actual rate of gross evaporation is $\sigma S_{A(B)}$. In addition, we define $G_{A(B)}$ as mass flux incident on meniscus A(B), and $J_{A(B)}$ as mass flux leaving meniscus A(B) by emission and reflection. Then the mass flux $\dot{m}_{pore}$ leaving meniscus A is given as:

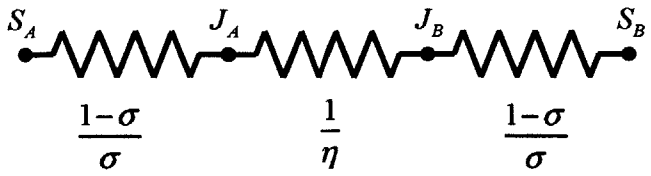

Figure 5. Configuration of mass transport resistances from analogy with radiation heat transfer

$$\dot{m}_{pore} = J_A - G_A = \sigma S_A - \sigma G_A, \tag{23}$$

where $J_{A(B)} = \sigma S_{A(B)} + (1 - \sigma) G_{A(B)}$ from the above definition. For meniscus B, the above equation is applicable in the same way except that the sign of $\dot{m}_{pore}$ reverses. $\dot{m}_{pore}$ can be obtained as follows:

$$\dot{m}_{pore} = \frac{\sigma}{1-\sigma}\left(S_A - J_A\right). \tag{24}$$

Therefore the mass transfer resistance through the meniscus between $S_{A(B)}$ and $J_{A(B)}$ is $(1 - \sigma)/\sigma$. In terms of incoming fluxes J_A and J_B at each meniscus, the net mass flux through the pore using transmission probability η is given as:

$$\dot{m}_{pore} = \eta\left(J_A - J_B\right). \tag{25}$$

Therefore the resistance from the pore wall can be simply $1/\eta$. Then the total resistance of this system is given as:

$$R_{total} = \frac{2(1-\sigma)}{\sigma} + \frac{1}{\eta}. \tag{26}$$

With the fluxes of mass source S_A and S_B, the net mass flux is obtained as:

$$\dot{m}_{pore} = \frac{S_A - S_B}{\sum R} = \sqrt{\frac{M}{2\pi R_g T}}\left(P_{vap,A} - P_{vap,B}\right) \Big/ \left(\frac{2(1-\sigma)}{\sigma} + \frac{1}{\eta}\right)$$
$$= \sigma\varphi_{A,B}\sqrt{\frac{M}{2\pi R_g T}}\left(P_{vap,A} - P_{vap,B}\right), \tag{27}$$

The mass flux across the membrane with porosity ε is then

$$\dot{m} = \varepsilon \dot{m}_{pore}. \tag{28}$$

2.5. Characteristics of vapor-phase transport through a nanopore

The theoretical maximum mass flux occurs when there is no resistance to transport across the nanopore, i.e. $\eta = \sigma = 1$. Under these conditions, the rate of condensation is equal to the rate of incidence of water molecules at the meniscus, and the rate of evaporation is also maximized (see Equation (11)). Molecules that evaporate at one meniscus undergo ballistic transport to the other meniscus, where they condense. The maximum flux per unit driving pressure ($\Delta P - \Delta\Pi$) depends on the interface temperature and vapor pressure of water, and can be expressed as:

$$\frac{\dot{m}_{net,\max}}{\Delta P - \Delta\Pi} = \varepsilon\sqrt{\frac{M}{2\pi R_g T}}\frac{V_m}{RT}P^0_{vap}(T). \tag{29}$$

This maximum mass flux increases rapidly with temperature, closely following the increase in equilibrium vapor pressure with temperature as shown in Figure 6a where $\varepsilon = 1$ is used to take only nanopore area into account. As the vapor pressure increases with temperature, the modulation of the equilibrium vapor pressure due to application of external pressure across the nanopore also increases; in fact, Equation (21) shows that the modulation is directly proportional to P^0_{vap}, the equilibrium vapor pressure of water.

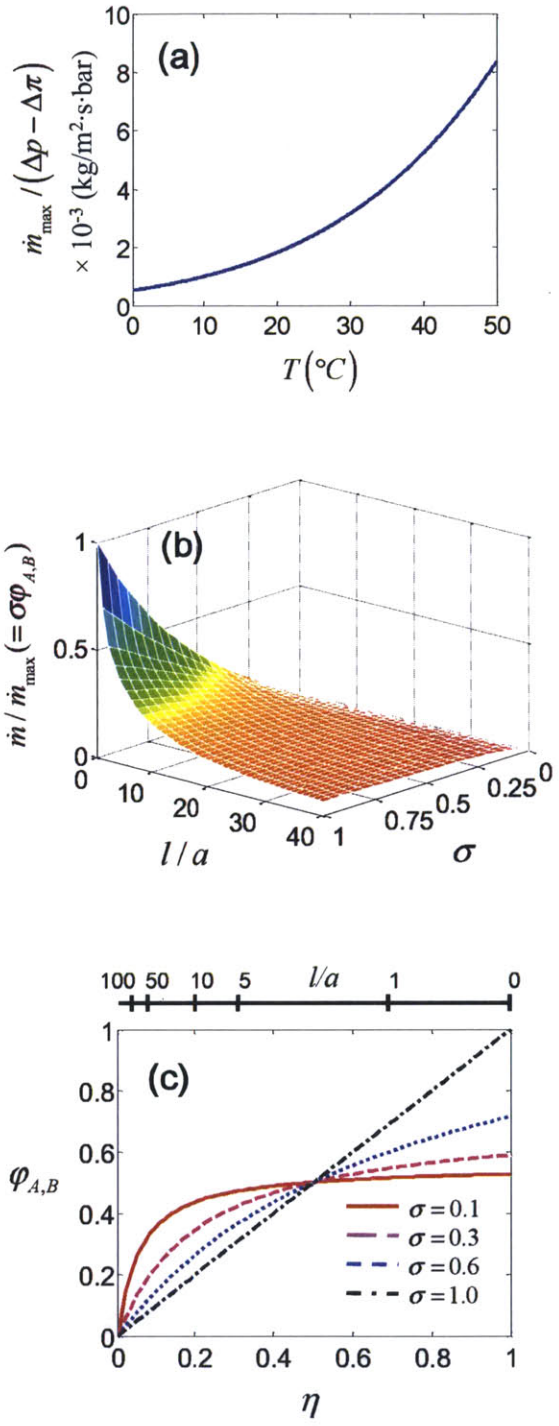

Figure 6. (a) Specific ratio of theoretical maximum mass flux to driving pressure at different temperatures. $\varepsilon = 1$ is assumed to consider nanopore area only. (b) Net mass flux normalized by theoretical maximum mass flux through a nanopore. The theoretical maximum mass flux indicates the mass flux for $\sigma = 1$ and $l/a = 0$ ($\eta = 1$). (c) Variation of $\varphi_{A,B}$ with η and σ. The scale bar on the top of (c) represents the pore aspect ratio l/a corresponding to η.

The ratio of the mass flux to the theoretical maximum mass flux equals $\sigma\varphi_{A,B}$, which is determined by the pore aspect ratio l/a (directly related to η) and the condensation coefficient σ. Figure 6b,c shows that $\varphi_{A,B}$ equals the transmission probability η when $\sigma = 1$. This case corresponds to zero resistance to mass flux at the menisci so that all water molecules incident on the meniscus undergo condensation. $\eta = 1$ corresponds to the case of a very short nanopore with ballistic transport, where $\varphi_{A,B}$ approaches $1/(2-\sigma)$. In this case, $\varphi_{A,B}$ equals 1/2 for very small σ; each molecule undergoes several reflections at the menisci, with equal chance of condensation at either meniscus. Thus, when $\eta > 0.5$ (corresponding to $l/a < 0.57$), a smaller probability of condensation decreases $\varphi_{A,B}$. When $\eta < 0.5$ (corresponding to $l/a > 0.57$), a smaller probability of condensation actually increases $\varphi_{A,B}$ (Figure 6c). While it may seem counterintuitive, it is easily seen that a molecule emitted from one meniscus has a high probability of returning to the original meniscus several times before reaching the other meniscus if the pore is long (small η). A small value of σ increases the probability of reflection from the original meniscus, thereby increasing the chance of reaching the other meniscus after undergoing multiple reflections at the original meniscus. Interestingly, $\eta = 0.5$ corresponds to a pore aspect ratio (l/a) of 0.57, in which case σ has no effect on $\varphi_{A,B}$.

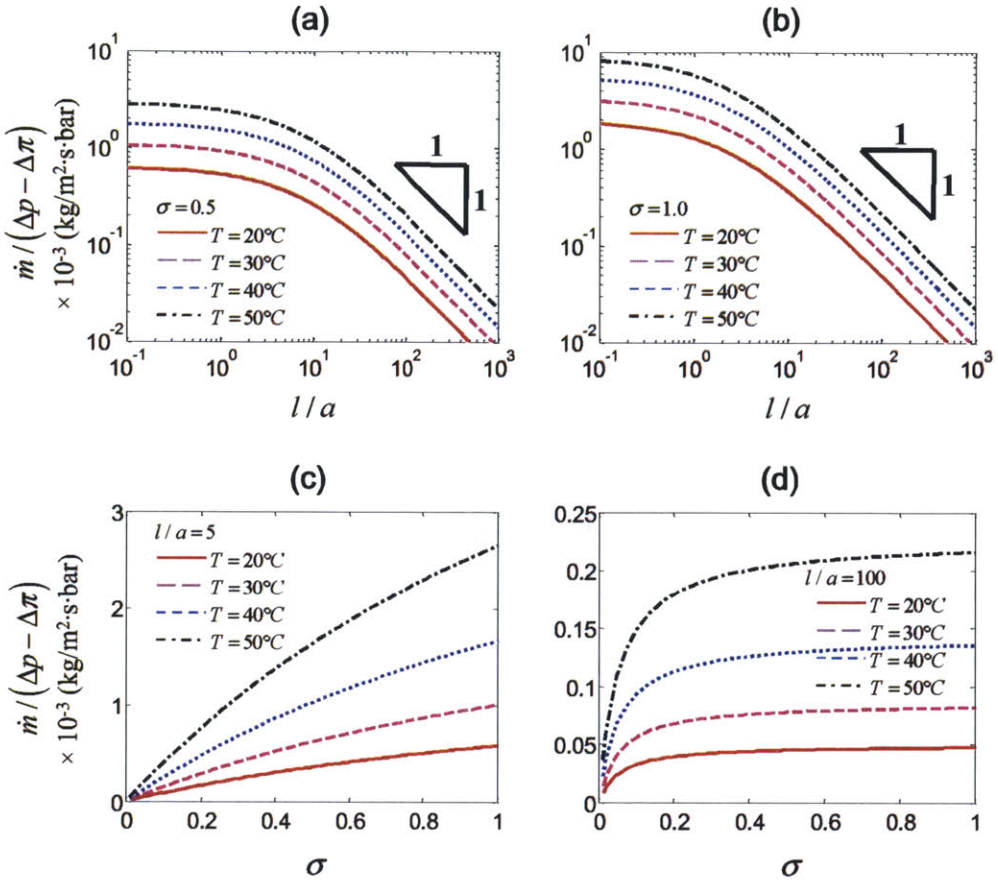

Figure 7. Effect of pore aspect ratio l/a and condensation coefficient σ on the mass flux through the pore per unit driving pressure at different temperatures. $\varepsilon = 1$ is assumed to consider nanopore area only. (a) $\sigma = 0.5$; (b) $\sigma = 1.0$; (c) $l/a = 5$; (d) $l/a = 100$.

Figure 7 illustrates the effect of temperature, pore geometry, and condensation coefficient on the net mass flux per unit driving pressure. Figure 7a and b reveal that the mass flux monotonically decreases as the pore length is increased. For very short nanopores ($\eta \rightarrow 1$), the flux is about three-fold higher at $\sigma = 1$ as compared with $\sigma = 0.5$; since a higher σ directly increases not only the rate of evaporation (see Equation (11)), but also $\varphi_{A,B}$ by reducing mass transport resistance at menisci. In the case of sufficiently long pores, the net flux decreases inversely as l/a, which is consistent with Knudsen flux with a constant Knudsen diffusion coefficient. In all cases, it is seen that the flux increases with increasing temperature due to the increasing vapor pressure. Figure 7c

and d show the effect of the condensation coefficient σ on the mass flux with T and l/a as parameters. For small pore length, for instance $l/a = 5$ (where $\eta = 0.23$) as shown in Figure 7c, the mass flux increases with σ. At very small values of σ, the linear variation is due to the linear increase in the rate of evaporation as given by Equation (11); $\varphi_{A,B}$ remains close to 0.5 since σ is small, as shown by Equation (10). On the other hand, for long pores ($l/a = 100$ shown in Figure 7d), the mass flux rapidly increases with σ for small σ and then becomes independent of σ. For very small values of σ, the mass flux is directly proportional to σ, since a low value of σ brings $\varphi_{A,B}$ close to 0.5. Above a moderate value of σ, resistance due to reflection at the menisci becomes negligible and transport is governed only by the transmission probability η. A close examination of Equation (10) shows that $\varphi_{A,B}$ is inversely proportional to σ for small values of η, and this effect is exactly offset by the increase in rate of evaporation with σ (Equation. (11)). Thus, the mass flux becomes nearly independent of σ and for very long pores and converges to its value corresponding to $\sigma = 1$. Since η approaches $8/3(l/a)$ for long pores, the mass flux converges to:

$$\dot{m} = \frac{8\varepsilon}{3(l/a)}\sqrt{\frac{M}{2\pi R_g T}}\left(P_{vap,A} - P_{vap,B}\right) = \frac{2}{3}\bar{v}a\varepsilon M\frac{P_{vap,A} - P_{vap,B}}{lR_g T} \qquad (l/a >> 1) \qquad (30)$$

This expression is the same as that derived for Knudsen diffusion flux through a pore with pressures $P_{vap,A}$ and $P_{vap,B}$ at either end. It implies that for sufficiently long pores, the actual vapor pressure at the each meniscus is maintained close to the equilibrium vapor pressure according to the local condition of the meniscus, which is often assumed to be the boundary condition to analyze mass flux in membrane distillation[32]. From Equation (10), the condition for this assumption to be valid is seen to be $2\eta << \sigma$.

2.6. Criteria for wetting of a hydrophobic nanopore

Implementation of the proposed technique for desalination will require appropriate choice of membranes with hydrophobic nanopores. The ability of the nanopores to resist wetting under a large applied pressure is critical for the operation of such a membrane. Several studies have examined the wetting and dewetting behavior of water in hydrophobic mesopores[62-64]. Using the Young-Laplace equation, the criterion that a pore of radius a resists wetting is:

$$a \leq \left| \frac{2\gamma_{lv} \cos\theta_{eq}}{\Delta P_A} \right| \tag{31}$$

where γ_{lv} is surface tension of the water and vapor interface, θ_{eq} is the equilibrium contact angle, and ΔP_A is the pressure difference across the interface. This criterion has been found to be valid for pores as small as 2.6 nm in diameter[62]. For a contact angle of θ_{eq} = 120° and a pressure difference ΔP_A = 50 bar, the critical pore diameter is 28 nm.

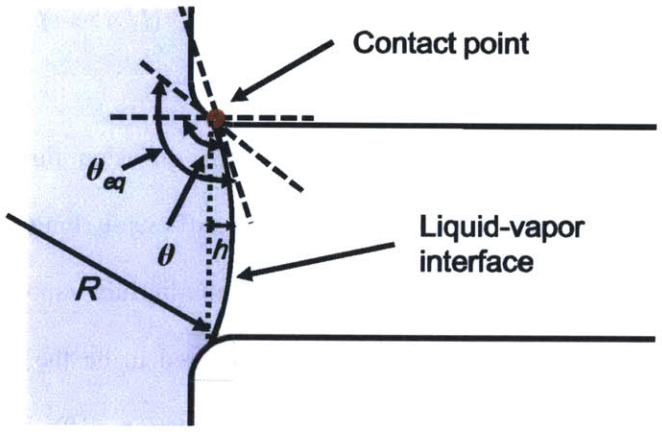

Figure 8. Detailed configuration of liquid-vapor interface at the feed side. θ_{eq} denotes equilibrium contact angle satisfying Young-Laplace equation (γ_{sl}-γ_{sv}+γ_{lv}cos θ_{eq}=0), and θ denotes the angle between a line tangential to interface and pore axis, which satisfies mechanical force equilibrium.

For a given pore radius, the aspect ratio *l/a* needs to be minimized to achieve a high mass flux. However, even if the pore radius satisfies Equation. (31), there is a critical aspect ratio below which wetting of the pore becomes energetically favorable[64], which may lead to merging of the two interfaces depending on the actual kinetic barrier. This condition depends on the length of the nanopore and can be expressed in terms of the pore aspect ratio. For a given radius of pore and pressure difference that can sustain a meniscus the interface will settle at a certain contact point with an equilibrium contact angle where force equilibrium is also satisfied. The angle θ between tangential line of the interface and pore axis at the contact point is determined by mechanical equilibrium, and is generally different from equilibrium contact angle θ_{eq} (see Figure 8). If the interface at the feed side moves in to fill the pore, *PV* work will be expended in forming new liquid-solid surface and a part of the work will be compensated by merging of the two liquid interfaces:

$$-\int_{V_0}^{0} \Delta P_A dV + \Delta E = (\gamma_{sl} - \gamma_{sv}) A_w - \gamma_{lv} (A_f + A_p), \tag{32}$$

where γ_{sl} and γ_{sv} are interfacial energies of solid-liquid and solid-vapor interfaces, respectively. V_0, A_w, A_f, and A_p denote the initial pore volume occupied by vapor and air, the areas of pore wall, menisci at feed and permeate sides, respectively. ΔE is the additional energy to induce the filling and therefore the filling would not occur spontaneously when $\Delta E > 0$. The *PV* work by applied pressure $P_{applied}$ moving interface then becomes

$$W_{PV} = -\int_{V_0}^{0} (P_{applied} - P_{pore}) dV = \Delta P_A V_0, \tag{33}$$

where P_{pore} remains constant to keep saturation condition. Assuming spherical shape of meniscus, the above equation becomes:

$$\Delta P_A V_0 + \Delta E = 2(\gamma_{sl} - \gamma_{sv}) \pi a l - \gamma_{lv} (2\pi R h + \pi a^2), \tag{34}$$

where V_0, ΔP_A, R, and h are given as:

$$V_0 = \pi a^2 l + \pi \left(\frac{a}{\cos\theta} \right)^3 \left[\frac{2}{3} - \frac{2}{3}\sin\theta - \frac{1}{3}\cos^2\theta \sin\theta \right], \tag{35}$$

$$\Delta P_A = -\frac{2\gamma_{lv}}{a}\cos\theta, \tag{36}$$

$$\frac{R}{a} = -\frac{1}{\cos\theta}, \tag{37}$$

$$\frac{h}{a} = \frac{R}{a} - \left[\left(\frac{R}{a} \right)^2 - 1 \right]^{1/2}. \tag{38}$$

Simplifying these equations, the criterion that satisfies $\Delta E > 0$ becomes:

$$\frac{l}{a} > \frac{1}{\cos\theta - \cos\theta_{eq}} \left[\frac{1}{2} + \frac{1}{1+\sin\theta} \right] \tag{39}$$

where $\cos\theta = -a\Delta P_A/2\gamma_{lv}$ and $\cos\theta_{eq} = -a_{max}\Delta P_A/2\gamma_{lv}$. For a given finite pore length, this criterion always gives a critical pore radius that is smaller than that calculated from the Young-Laplace criterion (Equation (31)). The wetting and dewetting behavior is not well-characterized for short hydrophobic pores bounded by menisci on either side. Thus, while it is possible that the Young-Laplace criterion is sufficient to prevent wetting, the thermodynamic criterion given by Equation (39) is more conservative of the two. For example, for a contact angle of θ_{eq} = 120°, pressure difference ΔP_A = 50 bar with NaCl of 0.62 M, and a pore radius of 5 nm, the minimum pore length that makes wetting energetically unfavorable is 15.2 nm. The minimum pore length at 20°C for different pore radii is given in Figure 9. Since the surface tension does not change significantly in the temperature range of 20-50°C (Table 1), the minimum pore length is not significantly affected by temperature.

Table 1. Values of parameters used in this study

Temperature (T_s) (°C)	20	30	40	50
Surface tension (γ_{lv}) (N/m)	7.28×10^{-2}	7.12×10^{-2}	6.96×10^{-2}	6.79×10^{-2}
Vapor pressure (P^{0}_{vap}) (Pa)	2.31×10^{3}	4.20×10^{3}	7.30×10^{3}	1.22×10^{4}

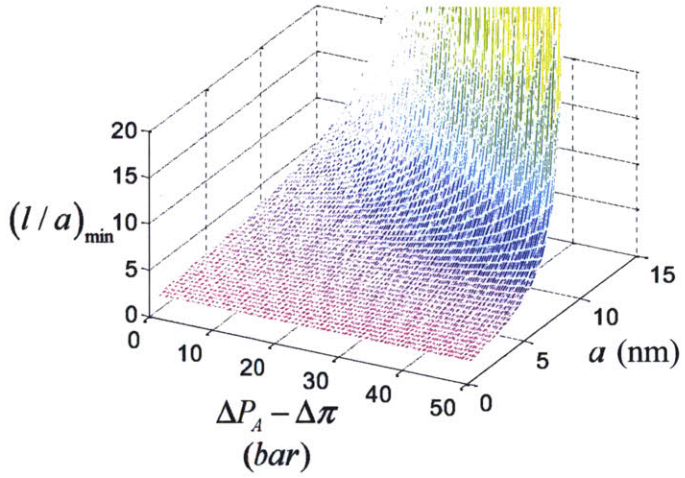

Figure 9. Minimum pore length that makes pore wetting energetically unfavorable at different values of the applied pressure and pore radius. Contact angle of 120°, NaCl concentration of 0.62M, and temperature of 20°C are assumed.

2.7. Mass flux through a membrane incorporating vapor-trapping nanopores

For a given pore radius that is smaller than the critical pore radius according to the Young-Laplace criterion, Equation. (39) predicts a minimum pore length for wetting to be thermodynamically unfavorable. Using this conservative pore length, Figure 10 depicts the mass flux (Equation (22)) through a membrane consisting of cylindrical pores with 40% porosity for

different pore radii and driving pressures for a 0.62 M NaCl feed water solution and a contact angle of 120°. For a given pressure drop, as the pore radius increases, the minimum aspect ratio $(l/a)_{min}$ also increases so that the transmission probability and mass flux are decreased. It is seen that nanopores with diameters in the 5-10 nm range might be practical for implementing this approach of desalination. Similarly, the flux increases significantly if temperature is increased from 20-50°C, and moderately as σ increases from 0.5 to 1. The red region with zero flux indicates that the pore radius is too large to sustain the applied pressure without wetting the pores. Thus, the highest flux occurs for the smaller pores. The validity of Equation (34) will have to be tested experimentally; it is entirely possible that shorter aspect ratios and therefore higher fluxes can be obtained even when wetting is thermodynamically favorable.

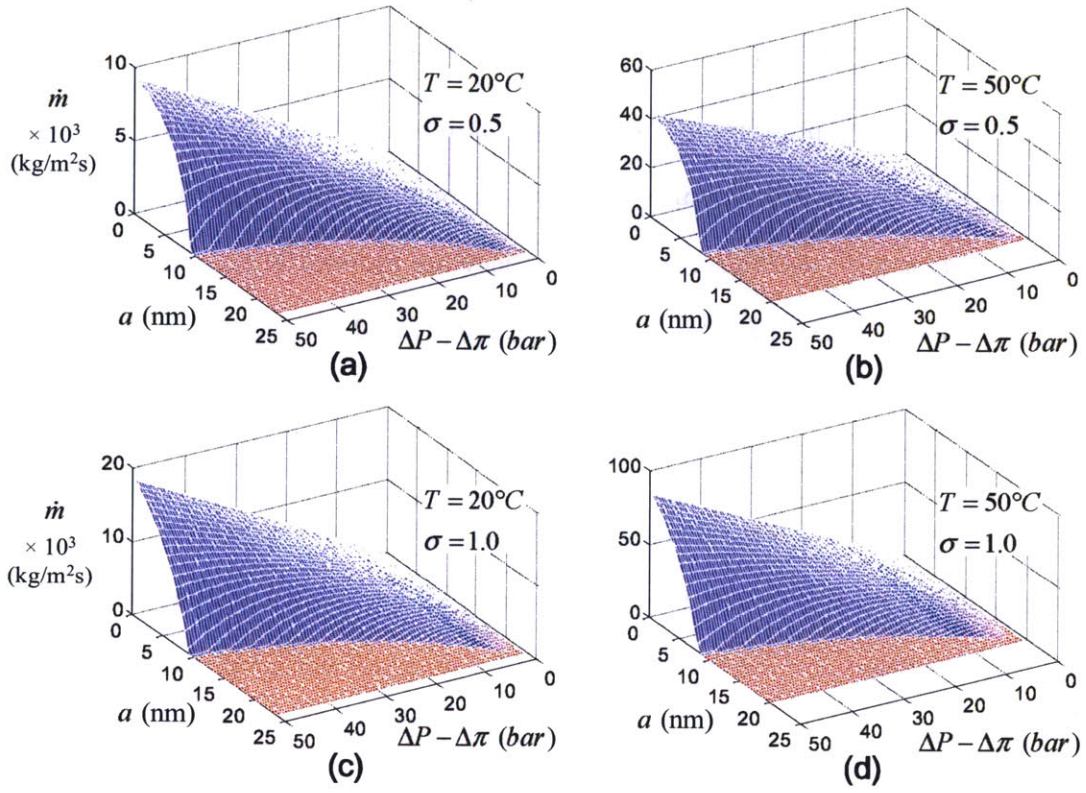

Figure 10. Predicted mass flux through membrane for different pore sizes and driving pressures at the minimum pore aspect ratio l/a which makes wetting thermodynamically unfavorable. Contact angle of 120°, NaCl concentration of 0.62 M, and 40% membrane porosity are assumed. (a) T = 20°C, σ = 0.5; (b) T = 50°C, σ = 0.5; (c) T = 20°C, σ = 1.0; (d) T = 50°C, σ = 1.0.

The predicted flux through the membrane is in the range of or larger than typical experimentally observed flux through current RO membranes[65-67]. Although we have not considered system-level issues such as concentration polarization and design of the membrane module, these results suggest that the proposed technique may be promising for desalination of water. For example, Figure 10 indicates that the maximum flux that can be achieved for a 40% porous membrane at 50 bar driving pressure is approximately 18 g/m^{2}s at 20°C and 70 g/m^{2}s at 50°C. RO membrane literature reports flux in the range of 5-22 g/m^{2}s for composite polyamide membranes[65-68]. Several different polymers and treatments have been explored for improving the selectivity[10, 69], flux[70], resistance to chlorine[71] and boron rejection[18]; however, there is a trade-off between these

parameters and improvement of one aspect tends to adversely affect the other aspects. Commercial membranes typically yield fluxes based on nominal membrane area in the range of 7.7-10.6 g/m^2s for driving pressures of 27 bar.[66] The theoretical results presented here suggest that membranes based on hydrophobic nanopores are promising for improving the flux as compared to current RO membranes, especially if they are operated at temperatures that are modestly above room temperature. Moreover, the currently used RO membranes do not have adequate chemical resistance to chlorine[8, 71], which is widely used as an industrial disinfectant to control biofouling. The inherent coupling between the permeability, selectivity, chlorine resistance and boron rejection that confounds optimization of polymeric membranes is decoupled in the case of the present approach. It is then conceivable that chlorine-resistant hydrophobic materials can be found for the manufacture of the proposed nanoporous membranes for desalination of water.

Chapter 3. Fabrication of membranes[2]

From the previous chapter, it is seen that nanopores with small aspect ratios are required to realize high flux of water vapor given the same applied pressure. Fabrication of membranes embedding such short nanopores with membrane thickness of ~100 nm will be challenging and the membranes will lack mechanical strength to self-sustain. There have been numerous studies on fluid transport involved in nanoscale conduits fabricated by e-beam[73, 74] and ion-beam[75] lithography, interference lithography[76], nanosphere lithography[77, 78], nanopore size tuning by atomic layer deposition[79, 80], track-etching[81], and carbon nanotubes[82]. Although the control of pore size using e-beam and ion-beam lithography is straightforward, fabrication of the pores in large area is time-consuming and costly. The other approaches often require extensive trial and error processes to find the proper parameters for the desired geometries such as length and pore size. Especially, fabrication of nanopores with any arbitrary lengths in large area has not been trivial. Porous alumina have been extensively studied[83, 84] and used as template of nanofabrication[85, 86] due to its regularity and controllability of nanopore geometry in large scale. In this chapter, we use porous alumina membrane as fabrication templates and designed membranes comprising nanopores with short hydrophobic regions of tunable length that trap nanoscale pockets of vapor separating two liquid phases (Figure 11a).

3.1. Creation of short hydrophobic nanopores

3.1.1. Fabrication approach

Porous alumina membranes (1cm x 1cm, Synkera Technology Inc.) with nominal diameter of 100 nm (actual diameter: 71.8±23.9 nm) were annealed at 1,000 °C to transform the material from

[2] This chapter can be referred to Lee et al.[72]

alumite to γ-alumina to prevent dissolution in water during the experiments. Positive photoresist AZ 5214E was placed under vacuum for 16 h to reduce the solvent content. The membranes were placed on a droplet (~7 μL) of the photoresist for 2 h to fill the nanopores and then baked on a hot plate at 100 °C for 50 min to evaporate the solvent. The photoresist was then etched by air plasma in a plasma cleaner (Harrick Plasma Inc.) at 7.16 W and ~0.7 mTorr, to expose short lengths (200-2500 nm) of the nanopores (Figure 11b). The membranes were then briefly washed with an aqueous solution of 5wt% phosphoric acid for about 1 min, and dried with nitrogen. The exposed surface was modified with a hydrophobic self-assembled monolayer created from vapor-phase perfluorodecyltrichlorosilane (FDTS) overnight in a vacuum desiccator. Hydrophobic surface modification using long alkyl-chain silanes has been extensively used due to its excellent hydrophobicity and durability[87-89]. FDTS is hydrolyzed by reacting with water and produces hydrochloric acid. The hydrolyzed molecules form silanol bonds after reacting with hydroxyl groups on the exposed alumina surface.

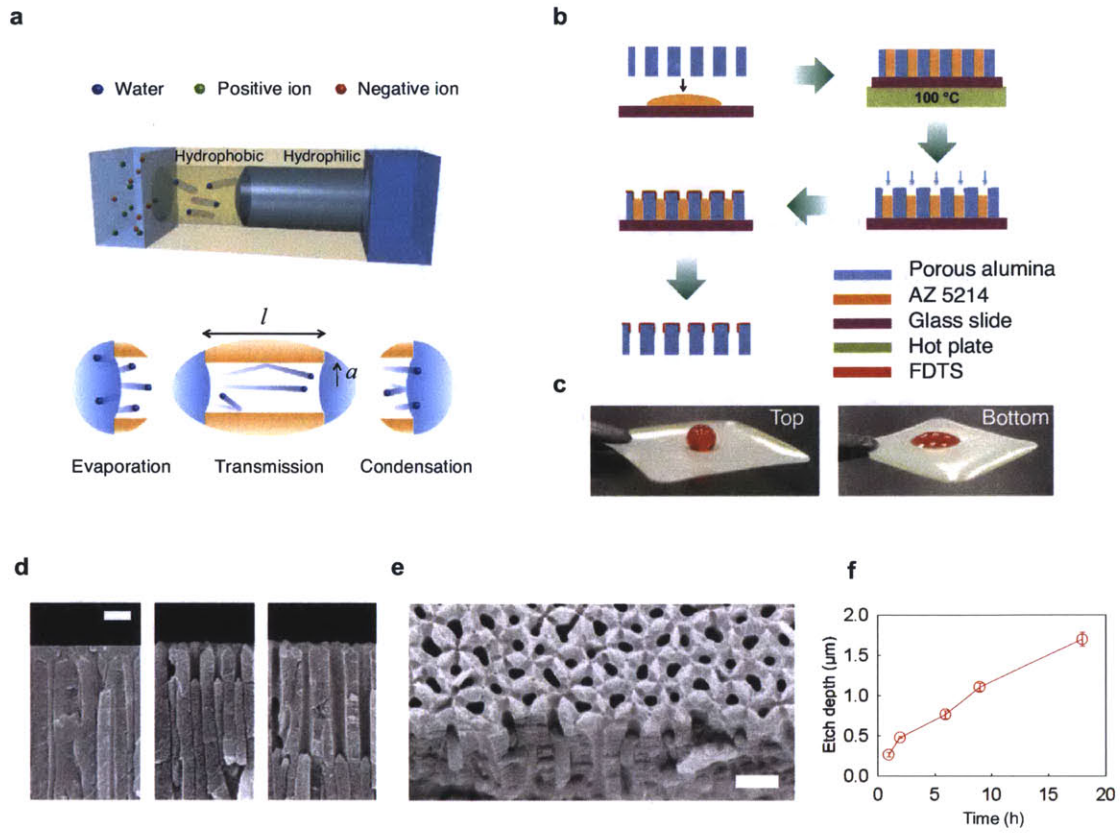

Figure 11. Fabrication of osmosis membranes with nanoscale vapor traps. a, Schematic illustration of membrane with short hydrophobic nanopores that trap vapor. b, Schematic of fabrication processes. i) porous alumina membrane soaked with photoresist AZ5214, ii) solvent evaporation on hot plate, iii) air plasma treatment for photoresist etching, iv) silanization on exposed alumina surface with perfluorodecyltrichlorosilane (FDTS), v) removal of residual photoresist. c, The fabricated membranes have a hydrophobic top surface (left) and hydrophilic bottom surface (right). d, SEM images of cross-section of nanopores after no plasma treatment (left), 2 h (middle), 9 h (right) of treatment, illustrating control of pore length for hydrophobic modification. Scale bar is 300 nm. e, SEM image of membrane after 2 h plasma treatment. Scale bar is 500 nm. f, Photoresist etch depth for different plasma treatment periods. Error bars represent ±S.D.

After majority of the photoresist was removed by washing in acetone, both sides of the membranes were exposed to UV light (~200 W) for 4 min each and the membrane was immersed in 3v/v% aqueous solution of ammonium hydroxide for 30 min to remove photoresist residues. The membranes were then baked overnight at 90 °C. The resulting membranes exhibited a hydrophobic top surface with a contact angle of 150.1±3.1° and hydrophilic bottom surface (Figure 11c). The length and aspect ratio (AR = l/a, where l and a are pore length and radius, respectively) of the hydrophobic nanopores could be tuned by simply controlling the duration of the photoresist etching step (Figure 11d-f, Figure 12), enabling control over the relative effect of the liquid-vapor interface on water transport as discussed later.

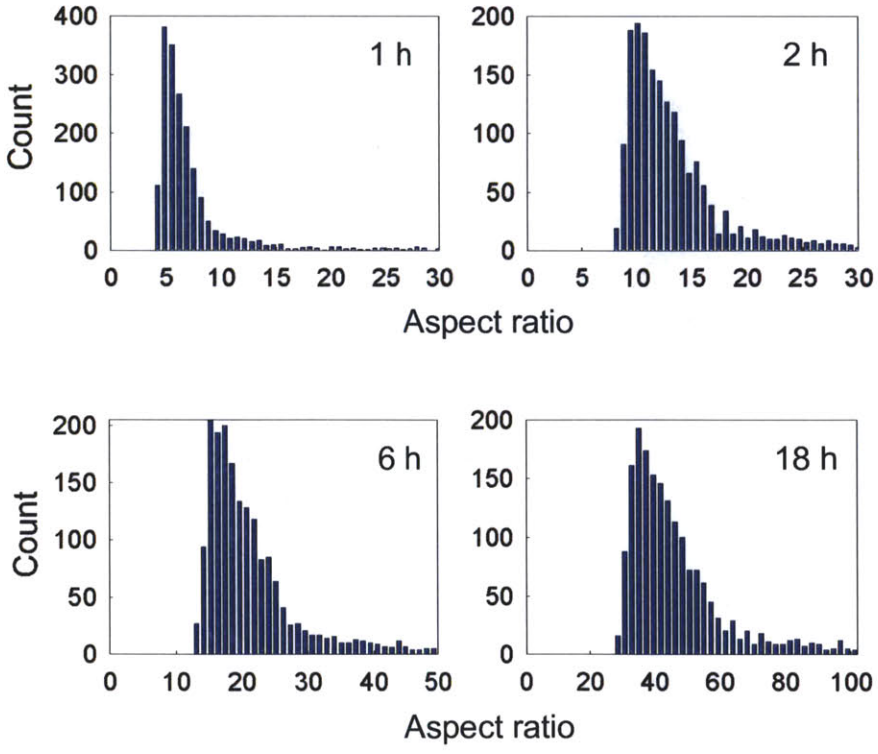

Figure 12. Aspect ratio (AR) distribution of nanopores after plasma treatment for different time periods.

3.1.2. Effect of annealing

The as-received anodized porous alumina, called alumite, has amorphous form[90]. As shown in Figure 13a,b, we found that the surface of as-received porous alumina membrane reacts with hot water (> 40 °C) and produces flower-like aluminium hydroxide (boehmite). Similar structure was reported from the alumina film made from sol-gel method and this highly rough structure has been also utilized for superhydrophobic surfaces[91]. In order to increase the stability in water, we annealed the porous alumina membrane at 1000 °C for 10 h. The annealed membrane did not show any surface structure transformation even after being immersed in boiling water for 2 h.

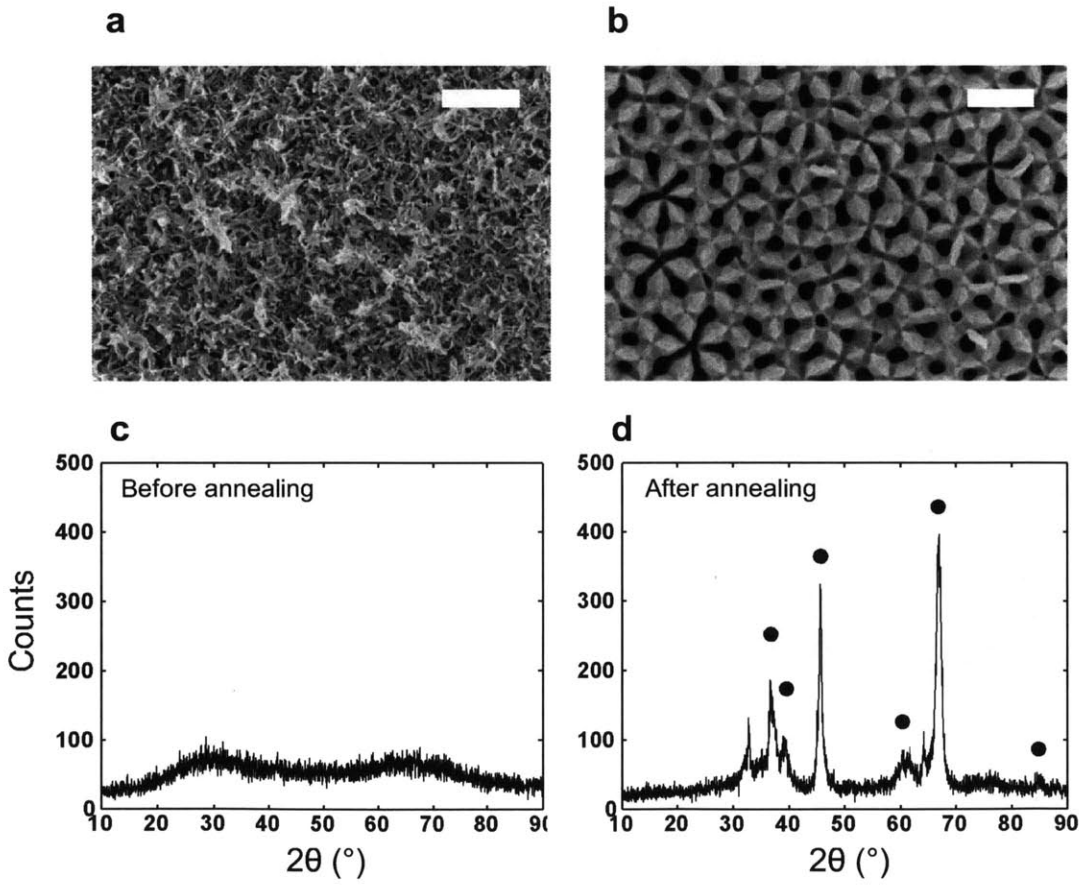

Figure 13. a, b SEM images of bare (a) and annealed (b) alumina membrane surface after dipping in boiling water for 2 h. Scale bar is 2 μm in (a) and 400 nm (b), respectively. c, d XRD spectrum for bare (c) and annealed (d) alumina membranes. Bare alumina reveals amorphous form while annealed one shows γ-alumina. Circles indicate peaks of γ-alumina.

This annealing step also greatly enhanced the chemical resistance to ammonium hydroxide which was used to dissolve any residual photoresist. XRD spectra for the alumina membrane before and after the annealing step are shown in Figure 13c,d where peaks corresponding to gamma-phase alumina were detected prominently.

3.1.3. Effect of ammonium hydroxide

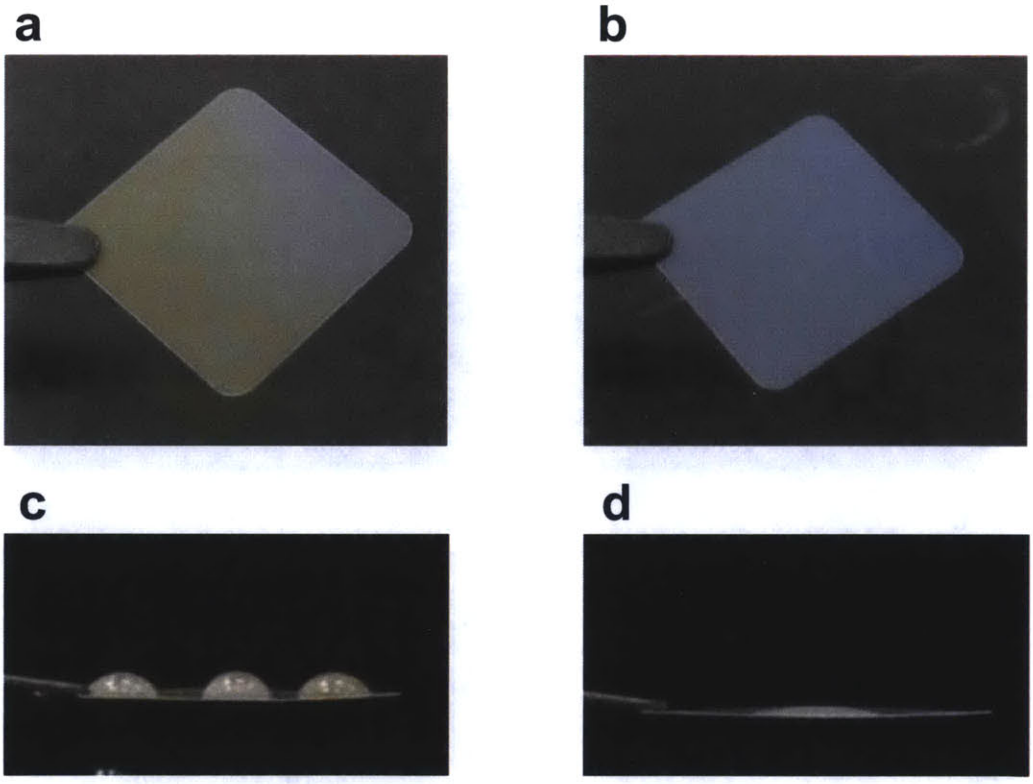

Figure 14. Photographs of hydrophilic side surface of membrane and water droplets on the surface before (a, c) and after (b, d) UV exposure and rinsing with ammonium hydroxide solution. The droplet completely spreads on the hydrophilic side after the treatment (d).

After silanization, the photoresist remaining in the nanopores was removed by acetone washing. However, we found that residual photoresist prevented water from completely wetting the hydrophilic part of nanopores. When this happens, the water meniscus is not formed at the

boundary of hydrophobic and hydrophilic regions in the nanopores and therefore the corresponding mass flux is low. Since the positive photoresist AZ 5214E acquires a carboxylic acid group upon UV exposure and becomes soluble in base, both sides of the membranes were exposed to UV (~200 W) for 4 min each after rinsing with acetone. The membrane was then placed in a gently stirred bath with 3v/v% NH_4OH (ammonium hydroxide) aqueous solution for 30 min. Figure 14 shows that the residual photoresist on the membrane was clearly washed away by this treatment. This procedure yielded repeatable fluxes, unlike the case with partial removal of photoresist in the absence of this treatment.

3.2. Verification of short hydrophobic nanopores

Several lines of evidence demonstrated the integrity of the fabricated membranes. After immersion in an aqueous gold nanoparticle (~3 nm diameter in average) solution, the particles were found to be excluded from regions that were exposed for surface modification, consistent with exclusion of the liquid phase from the hydrophobic nanopores (Figure 15a). Figure 15a also suggests the creation of sharp two-phase interfaces co-located at the position to which the photoresist was originally etched. Over 90% of the nanopores had gold nanoparticles adsorbed up to the hydrophobic-hydrophilic boundaries, indicating good wetting of the hydrophilic surfaces. When two different fluorescent dye solutions were placed on either side of the membrane, confocal microscopy revealed that the solutions did not mix, although the gap between the two solutions was too small to be resolved (Figure 15b). Environmental scanning electron microscopy under water vapor saturation conditions revealed that the top thin hydrophobic layer remained un-wetted (Figure 15c).

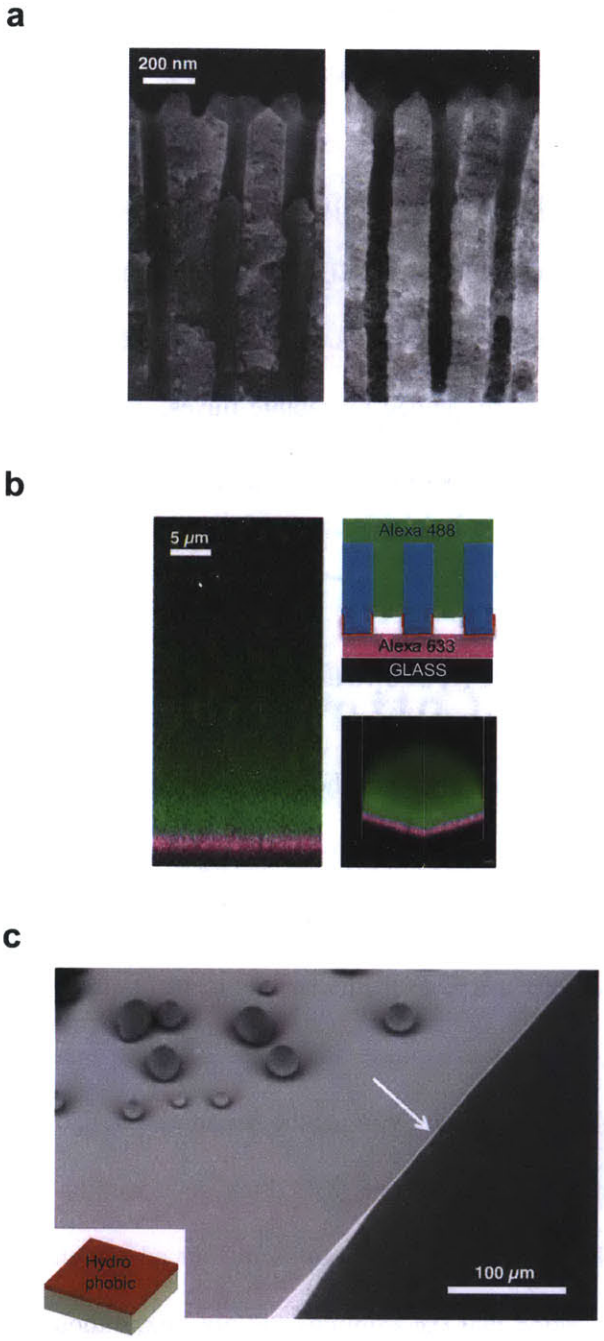

Figure 15. Verification of membrane integrity. a, SEM images of cross-section of nanopores after 2 h plasma treatment (left) and after immersion of the fabricated membrane in 3 nm gold nanoparticle solution (right) show co-localization of the nanoparticles with the extent of photoresist etching. Scale bar is 200 nm. b, Confocal microscopy of the membrane exposed to two different fluorescence dye solutions (Alexa 633 and Alexa 488 in deionized water) on either sides of membrane reveals a distinct interface with lack of mixing. Scale bar is 5 μm. c, Environmental SEM image of fabricated membrane showing hydrophilic and hydrophobic surfaces. Arrow indicates the non-wetted region appearing as a thin line corresponding to the hydrophobic modification. Scale bar is 100 μm.

3.3. Measurement of defect rates

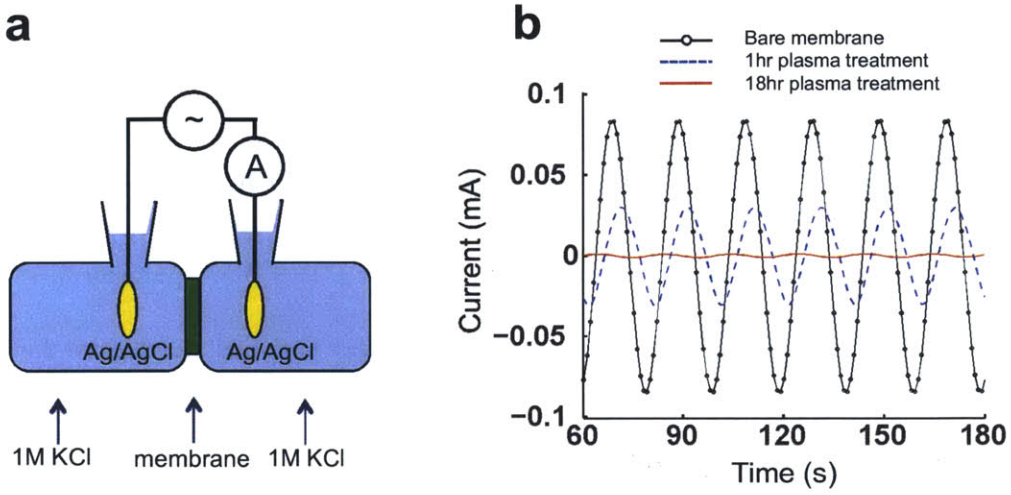

Figure 16. a, Schematic diagram of setup for impedance measurement. Electrical potential is given $V = V_0 \sin(2\pi ft)$ with $V_0 = 20$ mV, $f = 50$ mHz. b, Example of current profile for bare alumina membrane without any treatment, fabricated membrane with hydrophobic nanopores made with 1 h and 18 h plasma etching, respectively.

While the water should be transported as vapor-phase across the membrane, salt ions in feed solution could leak to the DI water in permeate side through any defective (hydrophilic) nanopores. Due to the large length of hydrophilic nanopore (~50 μm), even small concentration of salt ions in permeate side can induce high concentration polarization on the hydrophilic side of the nanopores. From a simple diffusion-convection scenario, $C_i \sim C_b \exp(uL/D_{salt})$ where C_i and C_b are concentration of salt ions at the meniscus location inside the nanopore and bulk DI water, respectively, u is flow velocity in hydrophilic part of nanopores with length of L, D_{salt} is diffusion coefficient of salt ions in water. In the typical experimental conditions, C_i can be up to 10 – 20 times larger than the bulk concentration of salt ions in the permeate side, implying that the salt concentration in the DI water must remain well below ~10 mM. Therefore if defects in the membranes cause serious leakage of salt to DI water, C_i may increase and become comparable to that of draw solution and vapor flux would be reduced significantly. We quantified the defects on the membranes using impedance measurement across the membranes (Figure 16a). AC electrical

potential was provided through Ag/AgCl electrodes dipped in cells with 1 M KCl solution on both sides of the membrane, and electrical resistance R^e was estimated from the measured current as $R^e = V_{rms}/I_{rms}$, where $V_{rms} = \sqrt{\frac{\int_0^T V^2 dt}{T}}$ and $I_{rms} = \sqrt{\frac{\int_0^T I^2 dt}{T}}$ with measurement time T. Impedance of membrane with fully wetted nanopores was estimated from $R^e_{wet} \sim \frac{L}{\alpha A \varepsilon} = 3.0\Omega$ where conductivity of 1 M KCl α ~ 10 S/m, orifice area A ~ 16.9 mm^2, porosity ε ~ 10%, nanopore length L ~ 50 μm. Direct measurement of R^e_{wet} was not possible due to the high impedance of the solution between the membrane and the electrodes.

Since two menisci face each other across hydrophobic nanopores, the membrane can be viewed as an electrical circuit consisting of a capacitor of capacitance C_{memb}, and electrical resistance component parallel to it. The frequency f of the applied AC electrical potential should be sufficiently smaller than $f_0 = 1/R^e_{memb}C_{memb}$ to ensure that the measured impedance represents electrical resistance without capacitive impedance. If we assume 1% of the pores are wetted, then R^e_{memb} ~ 300 Ω. If we also assume a length of hydrophobic nanopore l ~ 100 – 1000 nm, $C_{memb} \sim \varepsilon_r \varepsilon_0 \frac{A\varepsilon}{l}$ ~ 20 – 200 pF with relative permittivity of air ε_r ~ 1 and electric constant ε_0 = 8.85 x 10^{-12} F/m. In the all impedance measurement conducted here, we used f = 50 mHz << $1/R^e_{memb}C_{memb}$ ~ 10^7 – 10^8 Hz. A small amplitude of voltage (20 mV) was chosen to prevent any nonlinear phenomena[92] and to avoid any significant electrowetting which may lead to merging of two menisci[88].

Figure 16b shows the current vs. time curve for different membranes. The fraction of defective (i.e. wetted) pores was estimated as $\chi = \frac{R^e_{wet}}{R^e - R^e_{solution}}$. Generally, the membrane with longer hydrophobic nanopores had fewer defects because as seen from the AR distribution in Figure 12,

it has smaller chance of having nanopores with low AR that are more prone to wetting. The defect rate turned out to be less than 1% for all cases and we would not expect any significant leakage. During the all experiments described later, the concentration of salt ions in the DI water side was also monitored by conductivity probe, which detected less than 0.1 mM KCl.

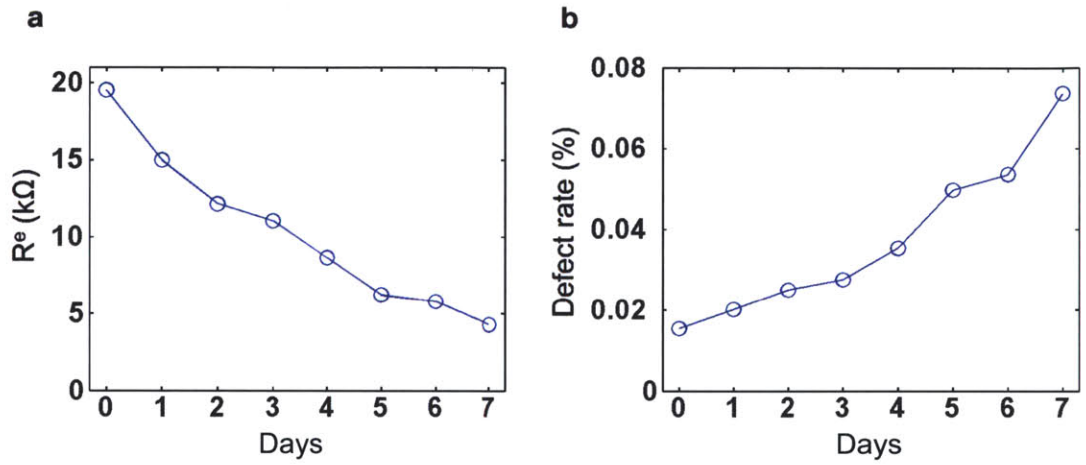

Figure 17. a, Resistance change with time for a membrane with hydrophobic nanopores made by 12 h plasma etching. b, Variation of the defect rate (i.e. fraction of wetted pores) with time.

3.4. Longevity of hydrophobic membrane

The longevity of hydrophobicity is crucial for practical applications such as fabrics[93], self-cleaning surfaces[94], or water treatment[95]. Since the membranes fabricated from the procedures developed here can be potentially applied for desalination[29], it is important to keep track on the hydrophobicity of the membrane for proper functionality. We monitored the wetting of the membrane pores stored in 1 M KCl solution, by measuring the electrical resistance across the membrane with time (Figure 17). The resistance of the membrane gradually decreased with time. After 7 days, the membrane resistance decreased from about 20 kΩ down to 5 kΩ, but the fraction of wetted pores still remained less than 0.1%. In the present study, the diameter of the nanopore is about 100 nm. For the smaller diameter with the same length of pores, the wetting

will be more energetically unfavorable and therefore the longevity would be enhanced. Increasing the longevity and durability of surface hydrophobicity[96] even for use in extreme environments[97] is an active area of research.

Chapter 4. Characterization of vapor-phase transport using forward osmosis experiments[3]

Although aqueous solutions on both sides of the membrane are not directly connected, water can be transported across the membrane by evaporation and condensation. While the water vapor is driven by the equilibrium vapor pressure difference, the modulation of the vapor pressure difference directly depends on the applied and osmotic pressure difference across the membrane (See Equation (17)). Therefore the effect of osmotic pressure on vapor flux is essentially the same as the applied pressure but in the opposite direction. Due to the brittle nature of the alumina, the fabricated membrane cannot sustain high mechanical pressures. We investigated the vapor-phase transport by forward osmosis where water is drawn by draw solution based on the osmotic

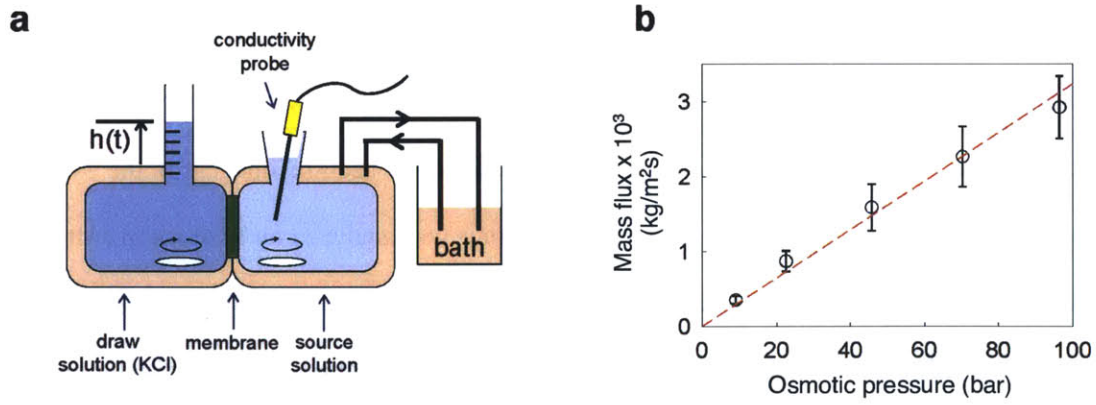

Figure 18. a, Schematic diagram of forward osmosis experiment setup. The deionized water in the right diffusion cell is drawn to the other cell with draw solution (KCl). Magnetic stir bars enhance mixing of solutions and minimize concentration polarization. b, Measured mass flux through a membrane for different osmotic pressure differences using 0.2, 0.5, 1, 1.5, and 2 M KCl as draw solutions, at a temperature of 25°C. Red dotted line is drawn as a guide for the eyes. Error bars represent ±S.D. for three different measurements on one membrane.

pressure difference across the membrane[98,99].

[3] This chapter can be referred to Lee et al.[72]

4.1. Experimental setup

4.1.1. Forward osmosis

The membrane was mounted between glass diffusion cells (Permegear Inc.) with 7 mL volumes on each side of the membrane. The diameter of the orifice where membrane is placed is 5 mm. However, due to the slight misalignment of the two cells, the active transport area of the membrane is somewhat reduced. While a non-treated alumina membrane is mounted between the cells, we filled up the cells with Allura Red dye (analytical standard, 98% purity, Sigma Aldrich) solution which stains the membrane surfaces. After the membrane was taken out, the overlapped stained area on each side of the surface was analyzed by ImageJ, from which the active transport area was obtained as 15.7 mm^2. The custom made-diffusion cells have luer-slip ports. A graduated 250-μL luer-tip glass syringe (Hamilton Co.) was mounted and bonded by melted paraffin on the port of the cell containing the KCl draw solution to measure the volume change (Figure 18a). Before each forward osmosis experiment, the cells were cleaned with piranha solution and by sonication for 1 h. A camera was set up to acquire images of the syringe at designated time intervals, from which the volume change was analyzed by Photoshop software. A constant temperature sheath flow around the cells was maintained using a peristaltic pump (Thermo Scientific) that circulated water from an external temperature-controlled water bath. The hydrophobic side of the membrane was always mounted facing the draw solution to ensure minimal concentration polarization. When solutions were introduced, hydrophilic side cell was always filled to ensure the complete wetting of the hydrophilic part of the membrane and nanopores. When the hydrophobic side cell (draw solution side) was filled, a large obvious air bubble was usually formed. To remove the bubble, a small tubing attached to a syringe (3mL, BD Syringe) was manually introduced to reach the bubble and the bubble was removed by gentle suction using the syringe. Whenever a new solution was introduced, e.g., different salt

concentration, the cells were rinsed with the same solution at least twice to prevent any contamination from residual previous solution. The temperature difference across the membrane is negligibly small (See Appendix B). With a relatively high thermal conductivity of alumina (~ 40 W/m-K), the temperature difference should be less than 10^{-4} °C and therefore the vapor transport occurs in isothermal condition. In all experiments, solute concentration on the hydrophilic side was low enough to ensure that concentration polarization was negligible.

4.1.2. Estimation of pressure inside nanopores

To prevent any bubble formation during the flux measurement, draw solutions and DI water were partially degassed by heating on the hot plate. Given that volume of nanopores is less than 0.01% of volume of air that can saturate the solutions, the concentration (pressure) of air in the nanopores should be in equilibrium with that in the solutions. Due to the fact that the ratio of solubilities of oxygen and nitrogen remain almost constant throughout the temperatures used in our experiments[100], we assumed that the dissolved air concentration in the solutions is proportionate to the dissolved oxygen concentration, which was measured by an oxygen indicator (eDaq). This measures electrical currents generated by galvanic cell reaction where the oxygen diffused into the indicator from the solutions is consumed at cathode. To calibrate the electrode, currents for a reference zero oxygen concentration were measured after boiling deionized water followed by bubbling with nitrogen gas for 10 min, while the currents for reference solutions saturated with air were measured at each temperature used in experiments. Oxygen concentrations in the solutions were calculated from the measured current assuming a linear relation of the oxygen concentration and the current. As a result, the average of the estimated air pressure in the hydrophobic nanopores under conditions used in the experiments reported in this work was 0.5 bar with ±0.3 bar of maximum deviation.

4.2. Verification of vapor-phase transport

The flux of water across the membrane increased with increasing osmotic pressure difference driving the flow, corresponding to increasing KCl concentration (Figure 18b). To confirm that the water was transported as a vapor-phase, a non-volatile Allura Red dye (Sigma Aldrich) was added to the deionized water side (2 mM). While the total volume of the draw solution was increased by ~ 150 μL, UV-vis spectroscopy showed that the draw solution remained free of the dye, corresponding to 99.90±0.025% rejection (Figure 19; error indicates S.D. for three different membranes). Noting that the nanopore diameter is 71.8±23.9 nm which is much larger than size of Allura Red (~ 1.2 nm), point of zero charge of alumina is at a pH about 8-9[101], and Debye screening layer thickness corresponding to high KCl concentration (1 M) is small, this rejection cannot be attributed to electrostatic exclusion of the negatively charged Allura Red. In contrast, in the absence of hydrophobic modification the alumina membranes rapidly allowed salt and the dye to diffuse to the other side. These results confirm that water was transported as vapor-phase in the fabricated membranes, while non-volatile substances were rejected.

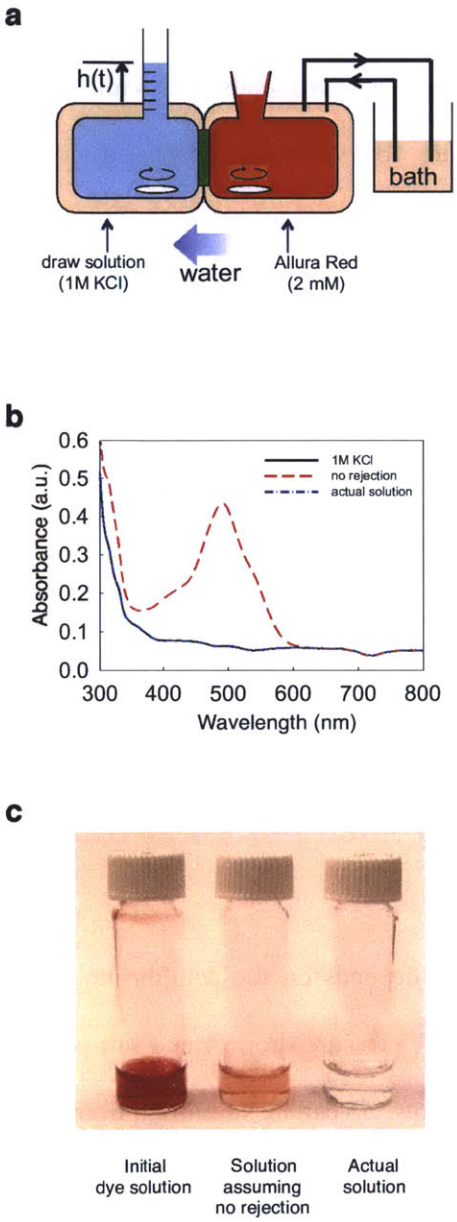

Figure 19. a, Forward osmosis experimental setup with diffusion cells containig 1M KCl draw solution (left) and 2mM Allura Red dy in DI water (right). b, UV-vis spectra show rejection of Allura Red dye. Black, 1 M KCl solution; red, Allura Red solution in 1 M KCl assuming zero rejection of dye mimicking how the draw solution would look if water were transported without dye rejection; blue, actual draw solution. d, 2 mM Allura Red solution in deionized water drawn across the membrane by the draw solution (left), Allura Red solution in 1 M KCl assuming zero rejection of dye mimicking how the draw solution would look if water were transported without dye rejection (middle), actual solution in draw solution cell after experiment showing dye rejection (right).

4.3. Effect of pore length on water transport

4.3.1. Behavior of mass flux for different pore aspect ratios

We investigated transport of water across membranes with different hydrophobic pore lengths using the same apparatus (Figure 18a). The flux decreased monotonically with increasing pore length, corresponding to an increasing pore aspect ratio (Figure 20). For long pores, we expect the flux to vary inversely with the pore length, therefore inversely with aspect ratio (AR) defined as pore length divided by pore radius. While flux through the longer nanopores approaches this inverse scaling (solid line in Figure 20c), the scaling breaks down for shorter nanopores, suggesting the emergence of different phenomena governing transport.

To understand this behavior, we recall the mass flux $\dot{m}$ across a membrane with porosity ε, as derived in Equation (22) & (27) considering the difference in evaporation rates at the two interfaces as the driving force across a series of transport resistances is as follows:

$$\dot{m} = \varepsilon \frac{S_A(T_A, P_A, C_A) - S_B(T_B, P_B, C_B)}{\sum R}, \tag{39}$$

The driving force $\Delta S = S_A - S_B$ depends on the equilibrium vapor pressure difference $P_{vap,A} - P_{vap,B}$ governed by temperature T, pressure drop P, and salt concentration C at each interface[29]. For isothermal, osmosis-driven flow, ΔS can be simplified from Equation (21) as:

$$S_A - S_B = \sqrt{\frac{MV_m^2}{2\pi R_g^3 T^3}} \left(P_{vap}^0(T) \Delta\Pi \right) \tag{40}$$

Here V_m is the molar volume of pure liquid water, P^0_{vap} is the equilibrium vapor pressure of pure water with a flat interface, and $\Delta\Pi$ is the osmotic pressure difference ($\Delta\Pi = \Pi_B - \Pi_A$) driving the transport. Note that the sign of osmotic pressure difference here is defined such that osmotically

driven flow is regarded positive. Given that the liquid phases are at ambient pressure, any Laplace pressure drops across the menisci (<1 bar) cancel out and do not affect the flux of water.

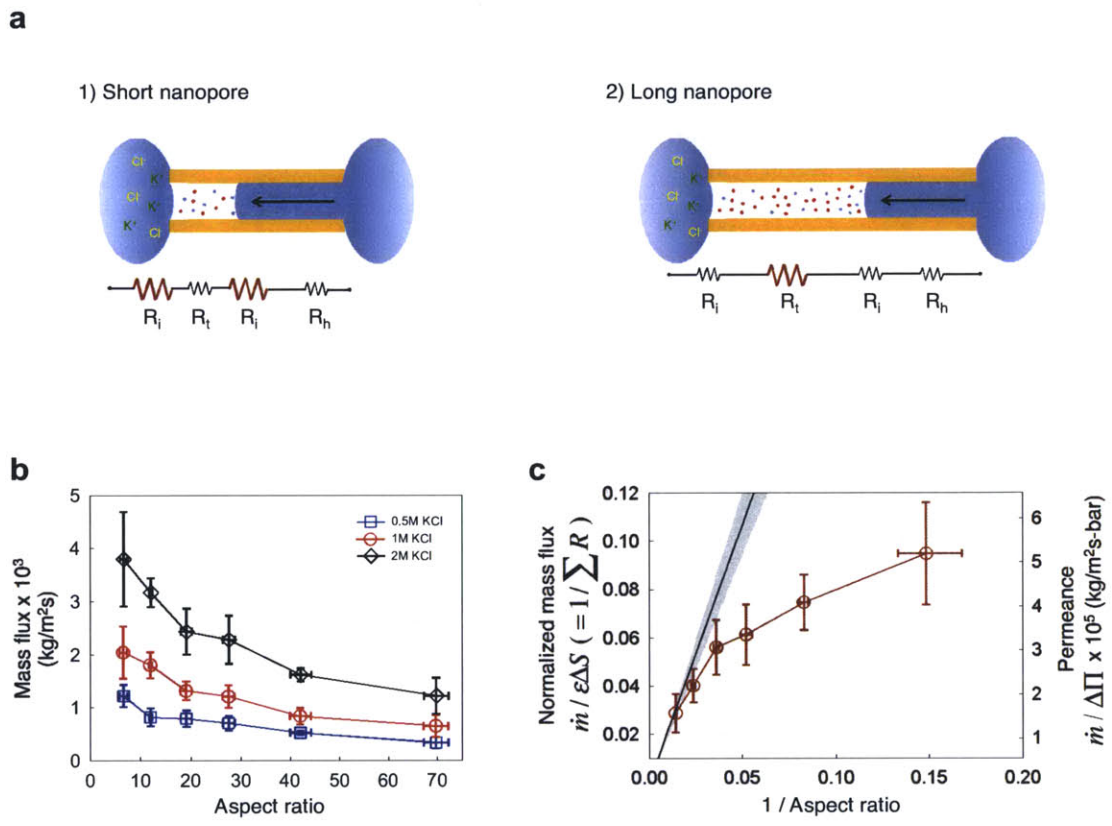

Figure 20. Scaling behaviour of the measured water flux. a, Schematic of resistance models for "short" and "long" nanopores. R_i, interfacial resistance; R_t, transmission resistance; R_h, hydrodynamic resistance. b, Variation of mass flux with AR for different KCl concentrations of draw solution measured at 39.0±0.3°C. c, Scaling of the measured mass flux normalized by maximum flux ($S_A - S_B$) with AR^{-1}. Note that as AR decreases, the normalized flux deviates from the solid line 2.12/AR corresponding to an inverse scaling expected in the case of long pores, plotted for pressure inside nanopore, p, of 0.5 bar. The shaded area indicates the possible range corresponding to $0.2 \leq p \leq 0.8$ bar (See Section 4.1.2).

As defined in Section 2.3.2, $\Sigma R = R_t + 2R_i$ in Equation 1 denotes the resistance to transport, comprising *i*) a transmission resistance R_t associated with vapor-phase transmission of molecules across the nanopores; and *ii*) liquid-vapor interfacial resistances R_i associated with reflection of

molecules at the liquid-vapor interfaces (Figure 20a). The hydrodynamic resistance to flow in the hydrophilic lengths of the nanopores is negligible.

$R_t = 1/\eta$, where η is the transmission probability of a gas molecule starting from one end of a pore to reach the other end[102]. R_t is dominated by collision of water molecules with pore walls in the Knudsen regime[34], but is influenced here to some extent by collisions with air molecules as the mean free path of water molecules in air (60-100 nm)[103] is comparable to the nanopore diameter.

4.3.2. Derivation of transmission probability for water molecules in a non-rarified condition (Dusty-gas model)

The average nanopore diameter used in the experiments is 71.8 ± 23.9 nm, which is in the same range as the mean free path in vapor-air mixture under ambient pressure. Therefore, molecular diffusion also plays a role in transport of molecules in addition to Knudsen diffusion. To take molecular diffusion into account, we used the dusty-gas model to derive an effective transmission probability across the nanopores. Dusty-gas model, which may be regarded as an extension of Stefan-Maxwell diffusion model, is widely accepted for gas transport through porous media and extensive reviews are available in literature[104-106]. Stefan-Maxwell diffusion model equates the friction force experienced by gas molecules due to interaction with other gas species molecules, to the external driving forces such as (electro)chemical potential gradient[106]. Dusty-gas model models the interaction of gas molecules with porous medium such as pore wall or network as stationary 'dust' particles, which introduces another source of friction force on the gas molecules of interest. This model was experimentally verified by Remick and Geankoplis for binary[107] and ternary[108] gas systems for diffusion of inert gases under uniform pressure (from Knudsen to molecular diffusion regime) through bundles of cylindrical tubes. Since our membranes can be

exactly regarded as bundles of nanopores, the dusty-gas model would also be valid in our case. Under experimental conditions considered here, the ideal gas law is valid. Then the equation of gas fluxes in porous media from dusty-gas model is given as[104]:

$$\sum_{j=1, j\neq i}^{n} \frac{x_j \bar{N}_i - x_i \bar{N}_j}{D_{ij}^e} + \frac{\bar{N}_i}{D_{iM}^e} = -\frac{p}{R_g T}\nabla x_i - \frac{x_i}{R_g T}\left(1 + \frac{B_0 p}{\varsigma D_{iM}^e}\right)\nabla p, \tag{42}$$

where R_g is the universal gas constant, T is temperature, and ζ is the viscosity of the gas mixture. p denotes the total pressure, x_i denotes the mole fraction of gas species i and $\bar{N}_i$ indicates average molar flux of species i based on total cross-section including the transport medium. B_0 refers to the permeability defined as $\bar{u} \equiv -(B_0/\zeta)\nabla p$ where $\bar{u}$ is average velocity of the gas mixture defined as flow rate divided by the total cross-section area, due to the pressure gradient. D_{ij}^e is the effective diffusivity associated with friction between species i and j, while D_{iM}^e is Knudsen diffusivity arising from interaction of species i with the medium (dust particles). Apart from the concentration gradient, the last term in the parenthesis on right-hand side indicates contribution to the flux from viscous flow driven by the total pressure gradient. Given that the membrane in this work can be assumed to be a matrix comprising bundles of cylindrical pores, $B_0 = \varepsilon a^2/8$ where a and ε denote radius of the cylindrical nanopores and membrane porosity, respectively. $D_{ij}^e = \varepsilon D_{ij}$ and $D_{iM}^e = \varepsilon D_{iM} = \frac{2}{3} a\varepsilon \bar{\upsilon}_i$ where D_{ij} is binary diffusivity of species i and j in free space, and D_{iM} is the Knudsen diffusivity for cylindrical pore[104]. Here, we assume that the gas inside the nanopores consists of two gas species, i.e., air and water vapor. By comparison of vapor pressure $P_{vap}{}^0(T) \sim 3 - 20$ kPa for 30 – 60 °C with atmospheric pressure, air can be treated as a majority species and therefore the properties of gas mixture such as viscosity are assumed to be the same as those of air. By substituting typical values of $a \sim 40$ nm, $p \leq 1$ bar, $\zeta \sim 1.8 \times 10^{-5}$ Pa s, $\varepsilon \sim 0.1$, $\bar{\upsilon} \sim \sqrt{\frac{8R_g T}{\pi M}} \sim 600$ m/s with molecular mass M of water 1.8×10^{-2} kg/mol, $\frac{B_0 p}{\varsigma D_{iM}^e} \sim 0.06 << 1$.

Thus, we can neglect the contribution from viscous flow. Provided that air inside the nanopores is stationary on average, the equation can be simplified further as:

$$\frac{(1-x_1)N_1}{D_{12}} + \frac{N_1}{D_{1M}} = -\frac{1}{R_g T}\nabla p_1, \tag{43}$$

where species 1 indicates water vapor, and 2 indicates air, while p_i is partial pressure of species *i*. Here, we used the relation $N_1 = \bar{N}_1 / \varepsilon$, where N_i refers to the molar vapor flux based on cross-section of pore only. The above equation then can be rearranged as:

$$-\nabla c_1 = N_1\left[\frac{1-x_1}{D_{12}} + \frac{1}{D_{1M}}\right], \tag{44}$$

where c_i is molar concentration of vapor, i.e., $p_i = c_i R_g T$. If we define an effective diffusivity given a concentration gradient such that $N_1 \equiv -D_{eff}\nabla c_1$, the following relation can be deduced:

$$\frac{1}{D_{eff}} = \frac{1-x_1}{D_{12}} + \frac{1}{D_{1M}}, \tag{45}$$

where x_1 is the fraction of vapor pressure in the mixture. At low temperatures such that $x_1 << 1$, the above equation can be simplified as $1/D_{eff} = 1/D_{12} + 1/D_{1M}$, which is also called the Bosanquet formula[109].

Evans et al.[110] calculated transmission probability for porous media by Monte-Carlo simulation and estimated the Knudsen diffusivity by equating mole flux calculated from the transmission probability with the flux calculated from a typical diffusion equation with the Knudsen diffusivity. Following their approach, transmission probability η of water molecules in the absence of air can be expressed as:

$$\eta\frac{\Delta c_1}{4}\bar{v} = -D_{1M}\nabla c_1,$$
$$\eta = \frac{4D_{1M}}{\bar{v}l}, \tag{46}$$

where Δc_1 is the vapor concentration difference between the both ends of a nanopore with length l, such that $\nabla c_1 = -\Delta c_1/l$. We postulate that in the presence of air, an effective transmission probability η_{eff} can be obtained from the effective diffusivity D_{eff} in Equation (45) as follows:

$$N_1 \equiv -D_{eff}\nabla c_1 = \eta_{eff}\frac{\Delta c_1}{4}\bar{v}, \tag{47}$$

and therefore,

$$\frac{1}{\eta_{eff}} = \frac{\bar{v}l}{4D_{eff}} = \frac{1}{\eta} + \frac{\left(1 - P_{vap}^0/p\right)\bar{v}l}{4D_{wa}}, \tag{48}$$

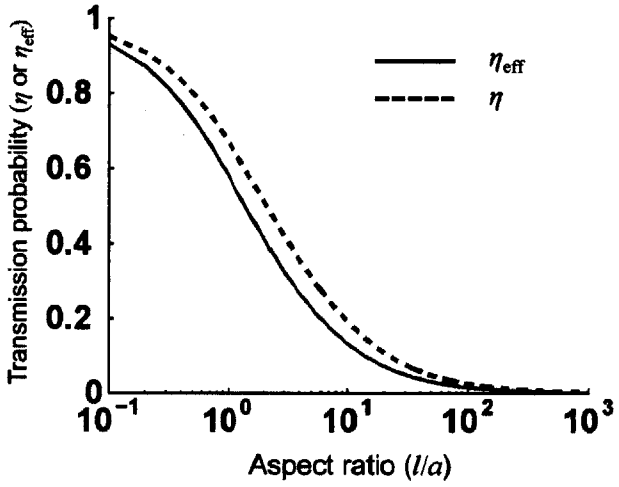

Figure 21. Transmission probability η[102, 111] for Knudsen regime and modified transmission probability η_{eff} for viscous regime. a = 40 nm, M = 1.8 x 10^{-2} kg/mol, T = 300 K, D_{12} = 2.56 x 10^{-5} m^2/s and p = 1 bar are used for the calculation

where p is again the total pressure inside the nanopores, ranging from vapor pressure to atmospheric pressure (1 bar). Note that if there is no air inside the nanopores, η_{eff} converges to η, which refers to purely Knudsen flow of water vapor. Figure 21 shows η and η_{eff} with a total pressure of 1 bar as a function of AR (= l/a). It is obvious that η_{eff} is always smaller than η because of additional transport resistance from scattering of water molecules by air molecules present in the pore. It should be mentioned that it would be hard to justify the above treatment to obtain η_{eff} for very small AR (<1). The Knudsen diffusion coefficient in the dusty-gas model is regarded as a rate of momentum transfer between the gas and the media. As the AR is reduced, however, ballistic transport will be more pronounced where the gas molecules directly reach the other side of the pore without colliding on the wall and therefore no momentum transfer would occur. Therefore it would be the case that only the gas molecules having interaction with the wall should be accounted for, to obtain the equivalent Knudsen diffusivity. The contribution of this ballistic transport on the transmission probability can be calculated by Walsh's approach[112], i.e., $\eta_{ballistic} = \frac{\sqrt{l^2+4a^2}-l}{\sqrt{l^2+4a^2}+l}$. While the smallest AR of the nanopores tested in our experiments is 6.7 ± 0.8, the contribution of ballistic transport to the total transmission probability is already less than 10% and decreases rapidly as AR increases. Therefore we expect that the above derivation is applicable to all ranges of the ARs tested in this study. However, if nanopores with much smaller ARs are considered, a different approach will need to be developed to come up with an equivalent Knudsen diffusivity. In fact, even though fabrication of short nanopores is straight-forward from our developed procedures, it would be challenging to prevent such nanopores from being wetted by water, since wetting of the such short hydrophobic nanopores would be energetically more favorable[29].

4.3.3. Mass flux for large AR

With the effective transmission probability η_{eff}, the flux normalized by theoretically maximum flux is given as:

$$\frac{\dot{m}}{\varepsilon \Delta S} = \frac{1}{R_t + 2R_i} = \frac{1}{\frac{1}{\eta_{eff}} + \frac{2(1-\sigma)}{\sigma}}. \tag{49}$$

Since the condensation coefficient is independent of pore aspect ratio, the normalized flux for large AR is determined by the asymptotic value of η_{eff}. As aspect ratio increases, it is expected that the flux follows a typical diffusion equation with a constant diffusion coefficient. Substitution of Equation (48) into Equation (49) leads to:

$$\frac{\dot{m}}{\varepsilon \Delta S} = \frac{1}{\frac{1}{\eta} + \frac{\left(1 - P_{vap}^0(T)/p\right)\bar{v}a}{4D_{wa}(T,p)}(l/a) + \frac{2(1-\sigma)}{\sigma}}. \tag{50}$$

For very large AR, $\frac{1}{\eta} \to \frac{3}{8}\frac{l}{a}$ and hence,

$$\lim_{l/a \to \infty} \frac{\dot{m}}{\varepsilon \Delta S} = \frac{1}{\left[\frac{3}{8} + \frac{\left(1 - P_{vap}^0(T)/p_0\right)\bar{v}a}{4D_{wa}(T,p_0)}\right]AR} = \frac{2.12}{AR}, \tag{51}$$

where a = 35.9 nm, T = 312 K, and $p = p_0$ = 0.5 bar are used. The normalized flux should be proportional to 1/AR and this asymptotic line is shown in Figure 20c with lower and upper bound for $p = p_0 \pm \Delta p$, where Δp is uncertainty of pressure inside the nanopore and was obtained as 0.3 bar from Section 4.1.2. The asymptotic lines for lower ($p = p_0 + \Delta p$) and upper ($p = p_0 - \Delta p$) bound are 1.88/AR and 2.41/AR, respectively.

4.3.4. Mass flux for small AR

While transport for large AR is described by a constant diffusion coefficient and scales as AR^{-1}, ballistic transport occurs in shorter nanopores causing deviation from the AR^{-1} relationship. However, the deviation observed in Figure 20c could also arise from the liquid-vapor interface that becomes significant for short nanopores (Figure 20a).

R_i is governed by the probability that a water molecule impinging from the vapor phase condenses into the liquid phase, called condensation (or mass accommodation) coefficient[46]. Under thermodynamic equilibrium, it equals the evaporation coefficient defined as the flux ratio of molecules emitted (evaporated) from the liquid to that of molecules incident from the vapor phase[48]. In our experiments, the net flux is less than 2% of the flux of impinging molecules from the vapor phase. Therefore, we assume that the two coefficients are equal, denoted by σ.

Equation (27) explains the monotonic increase of flux with temperature for membranes with a fixed AR of 42.1±2.1 (Figure 22a), since P^0_{vap} increases with temperature. The flux of water

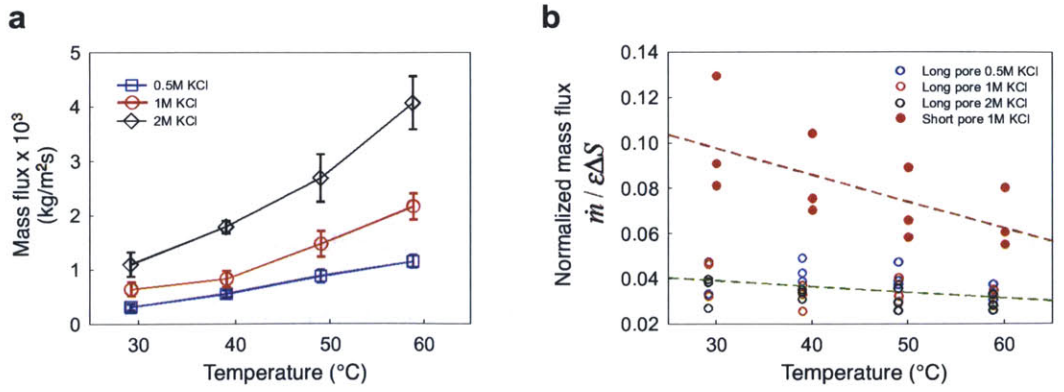

Figure 22. a, Dependence of the measured mass flux on temperature for AR = 42.1±2.1. b, Temperature dependence of total resistance for "long" pores with AR of 42.1±2.1 and for "short" pores with AR of 9.6±0.7. Dotted lines are linear fits to data averages to guide the eyes. Vertical error bars in all panels represent ±S.D. corresponding to measurements on 3 to 5 different membranes for each data point. Horizontal error bars in all panels represent ±S.D. for AR as described in Appendix D.

normalized by the driving force and membrane porosity depends only on transport resistance, i.e., $\dot{m}/\varepsilon\Delta S = 1/\sum R$. We find that for membranes comprising longer nanopores (AR = 42.1±2.1) $\dot{m}/\varepsilon\Delta S$ is invariant with temperature (Figure 22b). However, for membranes with short nanopores (AR = 9.6±0.7), $\dot{m}/\varepsilon\Delta S$ decreases with increasing temperature, indicating that $\Sigma R = R_t + 2R_i$ is temperature-dependent. While the transmission probability is only geometry dependent[102], the observed behavior could reflect temperature dependence of σ as some studies suggest[42, 113]. Any temperature dependence of R_i will only affect transport across shorter nanopores, as R_i becomes negligible compared to R_t for long pores. While these results suggest that the liquid-vapor interface may play a role in the deviation from linearity observed in Figure 20c, we now turn our attention to clarify the magnitude of this effect.

4.4. Effect of interfacial resistance on water transport

To isolate the effect of the condensation coefficient, we normalized the flux by that expected for a condensation coefficient of unity (*i.e.* $R_i = 0$, Figure 23a). We find that the normalized flux approaches unity for large AR (longer pores) where we expect the liquid-vapor interfaces to offer minimal resistance, verifying that Equation (49) (which does not have any fitting parameters when R_i is negligible) accurately accounts for the transmission resistance. However, for small AR the mass flux is significantly lower than that predicted for zero interfacial resistance, indicating a condensation coefficient less than unity and a significant contribution of the interfacial resistance to transport.

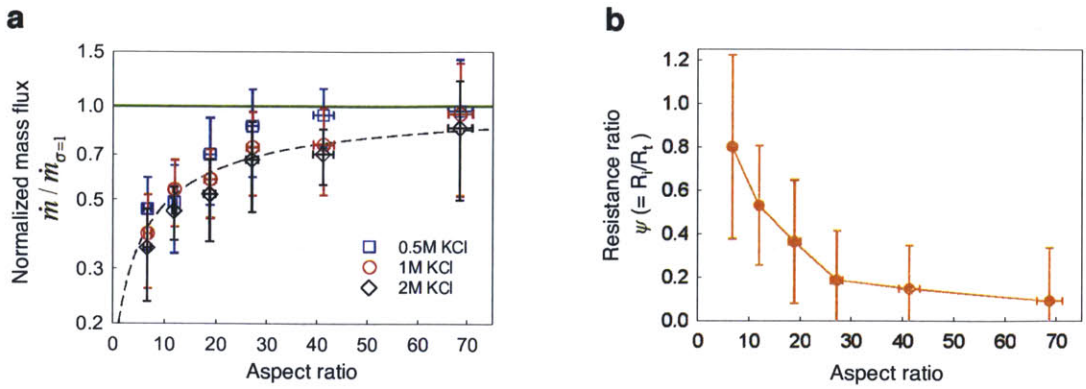

Figure 23. Regime of interface-governed transport. a, Mass flux normalized by the maximum mass flux corresponding to zero interfacial resistance ($R_i = 0$) for different concentrations of draw solution reveals a marked departure at smaller aspect ratios. Temperature is 39.0±0.3 °C. Green line indicates ideal normalized flux for $\sigma = 1$ as a guide for the eyes. Black dotted line denotes the theoretically predicted normalized mass flux for a condensation coefficient of 0.23. b, Ratio of interface resistance to transmission resistance for different AR at a temperature of 39.0±0.3 °C, obtained from data shown in panel a. Vertical error bars in all panels represent uncertainty combining S.D. of data points and the effect of uncertainty in pressure inside the nanopores, p (See Appendix D). Each data point was obtained from measurements on 3 to 5 different membranes. Horizontal error bars in all panels represent ±S.D. for AR as described in Appendix D.

The results demonstrate the existence of two transport regimes: The first regime occurs in large AR pores in which the influence of condensation coefficient (and therefore interfacial resistance) is negligible and mass flux is governed by the transmission resistance. The second regime corresponds to small AR pores where the interfacial resistance is significant. The two regimes are delineated by a dimensionless parameter $\psi \equiv R_i/R_t = \eta_{\text{eff}}\ (1 - \sigma)/\sigma$, given by the ratio of the interfacial and transmission resistances. The effect of the liquid-vapor interface becomes significant when ψ increases (Figure 23a,b). ψ has an interesting probabilistic interpretation. When the interfacial resistance is negligible, the outward flux of molecules evaporated from the interface must be S_A. This flux constitutes molecules that have directly evaporated, and those that have returned with probability $r = (1 - \eta_{\text{eff}})$ and have been reflected from the meniscus with probability $(1 - \sigma)$. Considering one meniscus and assuming that the other is ideal ($\sigma = 1$), the outward flux from the first meniscus is simply given by $\sigma S_A\left(1+r(1-\sigma)+r^2(1-\sigma)^2+\ldots\right)=S_A/(1+\psi)$. Hence, $\psi << 1$ is the condition for the outward

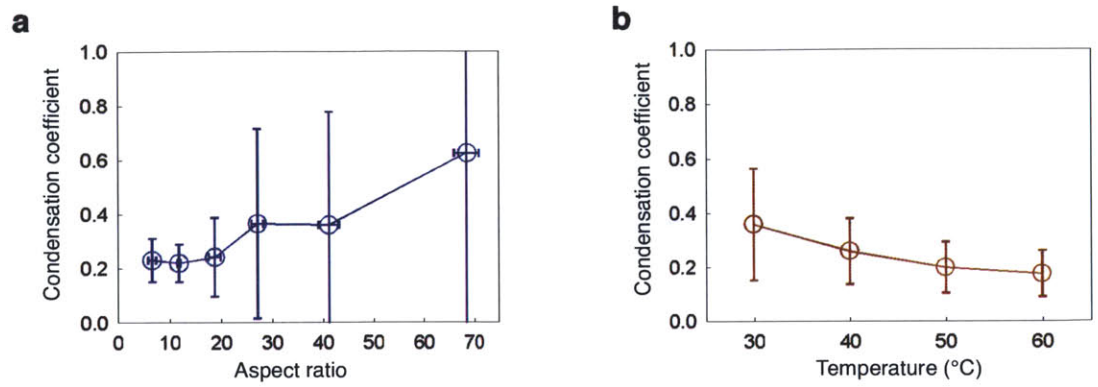

Figure 24. Estimated condensation coefficients for different AR at a temperature of 39.0±0.3 °C, obtained from data shown in Figure 23 panel a (a) and for different temperatures, obtained from flux measurements on membranes with AR of 9.6±0.7 (b). Vertical error bars in all panels represent uncertainty combining S.D. of data points and the effect of uncertainty in pressure inside the nanopores, p (See Appendix D). Each data point was obtained from measurements on 3 to 5 different membranes. Horizontal error bars in all panels represent ±S.D. for AR as described in Appendix D.

flux from the meniscus to approach that for an ideal meniscus. When $\sigma = 1$, the directly evaporated flux equals the ideal flux and there is no contribution from reflection, but when $\sigma < 1$, a finite return probability (*i.e.* $\eta_{\text{eff}} < 1$) combined with reflection from the meniscus ensures a close to ideal flux if $\psi << 1$. Conversely, if we consider molecules incident on the meniscus, for $\psi << 1$ molecules impinging on the meniscus either readily condense upon incidence when $\sigma = 1$, or if they are reflected when $\sigma < 1$, they always return back to the meniscus ($\eta_{\text{eff}} << 1$) and condense. On the other hand, for $\psi >> 1$, impinging molecules cannot readily condense upon incidence ($\sigma << 1$), or the reflected molecules ($\sigma < 1$) escape to the other side readily ($\eta_{\text{eff}} \approx 1$) so that the chance of condensation on the meniscus is small.

While the interface can govern transport of water, the membrane permeance $\dot{m} / \Delta\Pi$ measured in this study (see Figure 20c) for porosity ~10% is comparable to that of polyamide-based forward osmosis membranes (~6.7×10^{-5} kg/m^{2}s-bar)[114], which is ~10^3-fold smaller than Poiseuille flow through the unmodified membrane. However, vapor-phase transport provides high selectivity for

non-volatile substances while potentially retaining flexibility in the choice of membrane material for improving properties such as chemical resistance.

4.5. Revisit condensation coefficient of water

The experiments also enable estimation of the condensation coefficient (σ) of water. The measurement of condensation coefficient of water has been the subject of long debates and disagreements for nearly a century. As explained in Section 2.2, condensation/evaporation processes involve transfer of mass and heat simultaneously. The transfer of latent heat involved in mass transfer by condensation/evaporation and heat transfer through thermal accommodation coefficient alter liquid surface temperature. The altered temperature field around the liquid surface also affects conductivity and diffusivity of water vapor or carrier gas, if any, which again changes rate of mass transfer[46, 115, 116]. Therefore the heat and mass transfer are coupled through the condensation coefficient and thermal accommodation coefficient. Since those coefficients are not directly measurable, typically the rate of condensation or evaporation is experimentally measured and the coefficients are estimated by fitting the curves from the coupled heat and mass equations.

4.5.1. Literature on estimation of condensation coefficient

Various experimental methods have been employed to estimate the condensation coefficient (and thermal accommodation coefficient) by measuring: 1) pressure or mass change during condensation/evaporation[113, 117-119]; 2) heat transfer coefficient[120, 121]; 3) droplet growth rates[45-47, 122-124]; 4) condensation rate of water isotope[42, 125].

Direct measurement of pressure/mass change for estimation of the condensation coefficient were performed relatively early[113, 117-119], where the rate of evaporation/condensation at measured surface temperatures was used to estimate the condensation coefficient. Although this method requires accurate measurement of surface temperature, it is not trivial to control and assure the accurate temperature in those apparatuses while latent heat transfer is present. The condensation coefficient estimated by this method varies, e.g., 0.027 – 0.042 by Delaney et al.[113], 0.04 by Alty[117], 0.42 by Hickman[118], and 0.7 – 1.0 by Bonacci et al.[119]

In the heat coefficient measurement method, water vapor is condensed on cooled surfaces, typically copper, and the overall heat transfer coefficient is measured[120, 121]. The overall heat transfer resistances can be decomposed into several components including conduction or convection inside/outside in liquid/vapor phase, respectively, conduction resistance in metal, condensation resistance, and so on. By modeling each resistance including the condensation resistance, the condensation coefficient is deduced from the measured overall heat transfer coefficient. Each resistance component such as condensate film or liquid flowing inside pipes, condensate substrate, and so on can be modeled by known heat transfer relations, while the condensation resistance involving condensation coefficient was modeled by Schrage[126] used in Mills and Seban's experiments[120] or modified formula used in Nabavian and Bromley's experiments[121]. Given the measured overall heat transfer coefficient, the accuracy of condensation coefficient depends on the relative magnitude of condensation resistance compared to the other resistances. Therefore the other resistances should be minimized to obtain more accurate condensation coefficient, which has not been trivial. Therefore the estimated condensation coefficient had somewhat large uncertainties, e.g., 0.45 – 1.0 by Mills and Seban and 0.35 – 1.0 by Nabavian and Bromley, respectively.

Estimation of condensation coefficient (and also thermal accommodation coefficient) of water based on droplet growth rate has been extensively carried out by many researchers[45-47, 122-124]. The

size of water droplets inside a chamber with typically supersaturated water vapor is measured and thermal accommodation coefficient and condensation coefficient are deduced by matching the growth rate with existing theories involving the coefficients. The simplest theory was developed by Maxwell[127] for quasi-steady and diffusion-controlled evaporation from a single droplet in continuum range where droplet size is much larger than the mean free path. The mass transfer rate, and therefore determining the growth rate, is regarded to be equal to the diffusion rate based on a constant diffusion coefficient and saturation vapor pressure right at the droplet surface, i.e., $j_c = D(\rho_s - \rho_\infty)/R$ where j_c is mass flux leaving the surface, D is diffusion coefficient of vapor in surrounding gas, ρ_s and ρ_∞ are vapor density at the surface and ambient, respectively. For heat transfer, analogous heat equation was derived. Fukuta and Walter[115] proposed improved mass and heat transfer equations by matching the above Maxwell's continuum flux with kinetic flux (molecular bombardment rate based on kinetic theory) at a location one mean free path away from the droplet surface. The heat and mass fluxes involve the thermal accommodation and condensation coefficients with which portions of bombarding vapor molecules transfer heat and mass, with rates corresponding to temperature and pressure at that location. Vietti and Schuster[128] pointed out that this Fukuta and Walter's and other more modified theories do not match experimental results for a broad range of pressure. Barrett and Clement[129] mentioned that Stefan flow, i.e., vapor flow due to mean flow of gas mixture (vapor and air), is not included in Fukuta and Walter's theory which could result in a slight error. Nevertheless, a number of experiments have been carried out to estimate the condensation coefficient based on these theories. Gollub et al.[130], Sageev et al.[47], and Shaw and Lamb[45] performed the growth rate measurement experiments of water droplets in diffusion chambers where the size distribution of droplets were estimated by light scattering. Chodes et al.[122] measured falling speeds of nucleated droplets and estimated grow rate. In these experiments, the condensation coefficients of water were estimated by matching the growth rate with Fukuta and Walter's theory. Since the droplet growth theory predicting the

growth rate has two unknown variables, i.e., condensation and thermal accommodation coefficients, the measured droplet growth rates cannot lead to a definitive set of the coefficients. Thermal accommodation coefficient has to be decided to obtain the condensation coefficient and the accuracy of thermal accommodation coefficient definitively affects the other. Chodes et al.[122] and Gollub et al.[130] assumed thermal accommodation coefficient of unity, while Sageev et al.[47] and Shaw and Lamb[45] deduced it from separate experiments such as thermal relaxation time measurement and freezing rate measurement, respectively. The estimated condensation coefficients were 0.033 by Chodes et al., 0.12 by Gollub et al., and 0.06 by Shaw et al. while the growth rate measured by Sageev et al. was insensitive to condensation coefficient which makes it difficult to deduce the condensation coefficient.

Fuchs improved the Maxwell's theory by introducing Stefan flow in case of binary mixture[116]. In order to maintain a uniform total pressure field, there must exist an equal and opposite pressure gradient of carrier gas to that of vapor. Given that the carrier gas (typically air) is non-condensable, the mean velocity of the carrier gas is zero, and therefore the carrier gas portion of the mean flux of the mixture, i.e., $x_g(N_g + N_v)$, should be equal and opposite to the diffusive flux generated by the carrier gas gradient, where x_g is mole fraction of the carrier gas and N_g and N_v are mole flux of the carrier gas and the vapor, respectively. He also proposed a correction factor to predict the heat and mass flux from rarified gas to continuum regimes as a function of Knudsen number[131]. Wagner improved further the theory by taking into account the effect of temperature and composition gradient on heat and mass flow[132]. In addition, Barrett and Clement[129] derived more accurate equations by including vapor enthalpy flux into the total heat flux. A comprehensive review for the development of the these theories is available in literature by Vesala et al.[133] Winkler et al. measured the rate of droplet growth nucleated from Ag nanoparticle and compared the rate with that predicted by the theories developed in the above line[46]. From that the expected droplet growth rate based on their experimental conditions was highly sensitive to

thermal accommodation coefficient and the prediction based on thermal accommodation coefficient of unity was well matched with the experimental data, they concluded that the thermal accommodation coefficient of water is unity, without a separate set of experiments to measure it independently. Once the thermal accommodation coefficient was set as unity, the condensation coefficient was estimated to be unity too, although the sensitivity of growth rate to the condensation coefficient was small and seemed somewhat difficult to obtain unambiguous values.

Condensation coefficient of water has been also estimated by measuring condensation rate of water isotopes. Jamieson[125] introduced a water jet into tritium-labeled steam and condensation rate of steam on the water-steam interface was measured by radioactivity of the jet at the receiver. While the condensed steam could re-evaporate when the jet is in contact with the steam for a long time, the possibility of re-evaporation was minimized by increasing the jet speed. It was observed that the radioactivity of the jet approached constant as the jet speed is increased, from which condensation coefficient is estimated to be larger than 0.305. Li et al.[42] performed a droplet train experiment where droplets were injected into a chamber full of saturated vapor with trace amount of D_2O or $H^{17}{}_2O$. The condensed amount of the isotopes were used to estimate thermal accommodation and condensation coefficients. The thermal accommodation coefficient they obtained is quite close to unity while they found the condensation coefficient decreases with temperature from 0.32 at 258 K to 0.17 at 280 K. Although there was a limitation on range of temperature tested and the droplet velocities were high corresponding to an effective increase in vapor temperature of 10-50 K, this is the first study up to our knowledge that clearly shows the temperature dependency of condensation coefficient of water.

4.5.2. Estimation of condensation coefficient based on transport through submicron length of hydrophobic nanopores

Although condensation coefficient lower than 0.1 measured in very early experiments is probably attributed to contamination of water surface[48], the difficulty in accurately obtaining condensation coefficient arises mainly from uncertainties in estimating heat and mass transfer resistances and the interfacial temperature in the presence of latent heat transfer[119, 134, 135], since a local temperature gradient is created and vapor pressure is a strong function of temperature. In such thermally non-equilibrium conditions, mass and heat transfer are coupled through condensation coefficient and thermal accommodation coefficient as fitting parameters as reviewed in the previous Section. There are two pathways for heat transfer from vapor to liquid-phase. While the latent heat is transferred to liquid from vapor-phase during the condensation, the vapor molecules impinging on the liquid surface can also transfer heat energy by thermal interaction with liquid-phase molecules, and may return back to the vapor phase corresponding to the condensation coefficient less than unity.

While the thermal accommodation coefficient has been typically assumed as unity, the experimentally measured values range from 0.7[45] to 1[42, 47]. In addition, use of different heat transfer models results in order-of-magnitude differences in the values of condensation coefficient, since the fitting is not very sensitive to condensation coefficient making acquisition of reliable values challenging[45, 47, 122, 134]. As reviewed in the previous Section, values of condensation coefficient measured experimentally even in relatively recent studies (since 1986) are scattered over almost two orders of magnitude (0.01 – 1) [42, 45-47, 124, 136, 137]. Molecular dynamics simulations have also yielded different condensation coefficients depending on the potentials used[138, 139] and therefore those values hardly match with experimental ones.

Among the studies discussed in the previous Section, we pay special attention to two most recent studies by a collaborative group who performed careful experiments under thermal equilibrium conditions by tracing condensation of H^{17}_2O on fast-moving water droplets[42] and measuring growth rate of droplet by nucleating on silver nanoparticles[46]. However, the magnitudes and

temperature dependency of condensation coefficient were not consistent between the two experiments. Although the reason was not clear, they conjectured that the condensation processes and thus condensation coefficient could be altered by dynamics of growing surface of water droplets[137]. The experiments by Winkler et al.[46] measured the condensation coefficient very far from equilibrium at high rates of evaporation, whereas the other experiments by Li et al.[42] involved droplet velocities corresponding to up to 40 K deviations in vapor temperature from equilibrium.

In our experiments, the proximity of two water menisci with the submicron gap guarantees accurate measurement of the condensation coefficient near equilibrium conditions ($\Delta T_{max} < 10^{-4}$ °C). Control of the nanopore geometry also allows for accurate estimation of the mass transport resistance, as verified by excellent agreement of Equation (44) with data in the case of membranes with large AR (Figure 23a). We find that a condensation coefficient of 0.23 describes the experimental results at 39.0°C for the entire range of AR (dashed line in Figure 23a). The detailed procedures to estimate the condensation coefficient from experiments are shown in Appendix D. The condensation coefficients estimated at each AR at 39.0°C agree for the small AR pores, while the uncertainties are large at higher AR where the interfacial resistance has a minimal impact on transport (Figure 24a). Condensation coefficients estimated at different temperatures for AR = 9.6±0.7 show a decreasing trend (Figure 24b), which qualitatively agrees with a recent experimental study by Li et al.[42] As reviewed in the previous Section, they carefully minimized temperature gradients by tracing the condensation of $H_2{}^{17}O$ on water droplets injected into vapor at high speeds, although at temperatures below 7 °C and at speeds corresponding to a vapor temperature elevated by ~10-50 K. Interestingly, the condensation coefficients match with those in the present work if the temperature scale is shifted by ~40 K.

The experiments reported in our study overcome many of the major uncertainties involved in measurement of the condensation coefficient, and demonstrate that majority of water molecules

incident on the liquid-vapor interface are reflected back into the vapor phase. Strictly speaking, condensation coefficient measured here is an averaged value of that at the two interfaces. The dependence of condensation coefficient on salt concentration, as well as ion types will be discussed in the next Section. If their effects are negligible, that would indicate that our estimated condensation coefficient is the correct value for pure water.

4.6. Effect of concentrations and type of salt on condensation coefficients

Since condensation occurs at the liquid-vapor interface, presence of foreign molecules other than water at the interface could potentially alter the condensation coefficient. It is well-known that organic impurities such as surfactants significantly reduce rate of condensation and in fact those contaminants are one of the main factors that result in very low estimated values of condensation coefficients in early experiments[48]. In our study, special care was taken to prevent any contamination. Before the measurement of flux, the diffusion cells were cleaned by piranha solution and by sonication in deionized water for 1 h, while the membranes were dipped in boiling deionized water and then thoroughly washed by deionized water. However, from the same reasoning it is possible that presence of ions at the interface affects the rate of condensation. If so, a concentrated solution should have a larger population of ions near the interface and we should be able to see a concentration dependence of the condensation coefficient. To investigate this hypothesis, a membrane comprising nanopores of average aspect ratio of 11.0 was used to measure the mass flux drawn by 0.2, 0.5, 1, 1.5, and 2 M KCl solutions at 25°C. The surface tension of the water changes within 5% even at 2 M solution[140]. Condensation coefficients were estimated through the same procedures stated in Appendix D. The resulting condensation coefficients did not exhibit significant dependence on salt concentration (Figure 25).

Another possible factor that could affect the condensation coefficient is type of salt ions. Recent Molecular dynamics simulation studies revealed that molecules of high polarizability such as heavier halogen anions, i.e., Br- and I^- tend to be accumulated at the liquid-vapor interface, while lighter ones such as F^- and Cl^- are depleted[141]. The anisotropic electrostatic field near at vapor-liquid interface stabilize the highly polarizable ions, even compensating the partial solvation[142, 143]. This dense population of heavy ions near the interface may change interaction of impinging vapor molecules with those in liquid phase. To investigate this possibility, we used two different draw solutions, i.e., 0.5 M KCl and 0.5 M KI, as model solutions comprising lighter and heavier halogen anions. Forward osmosis experiments were performed at 30°C for membranes with an average nanopore aspect ratio of 8.5, and condensation coefficients were estimated (Figure 26). The two values were not statistically different from each other based on student t-test. These results suggest that the type of salts and correspondingly the participation of ions near the surface do not significantly affect the condensation coefficients compared to other uncertainties under the experimental conditions employed in this work.

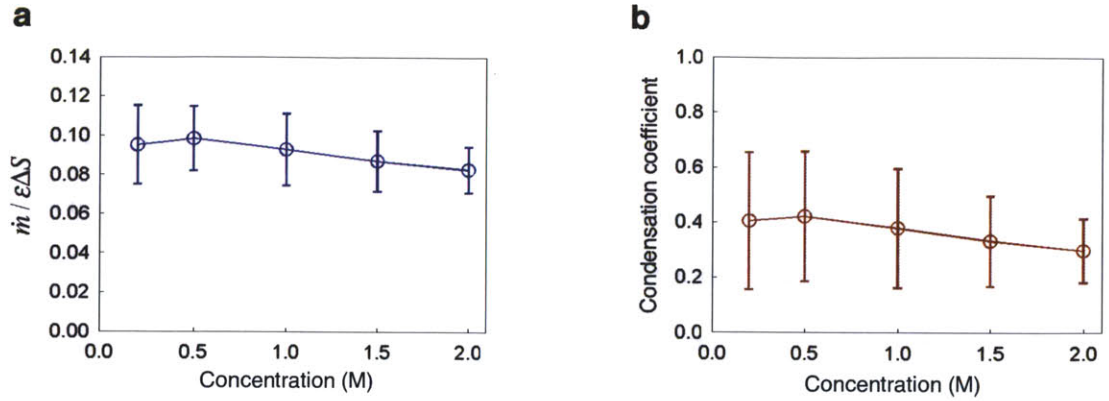

Figure 25. Effect of salt concentration on condensation coefficients. Nanopores with average aspect ratio of 11.0 were used at 25°C. a, Mass flux for different KCl concentrations, normalized by membrane porosity and by difference of evaporation rate across the membrane; b, Estimated condensation coefficients from the measured mass flux. The error bars denote ±S.D. including the effect of uncertainty in pressure inside the nanopores, p (See Appendix D).

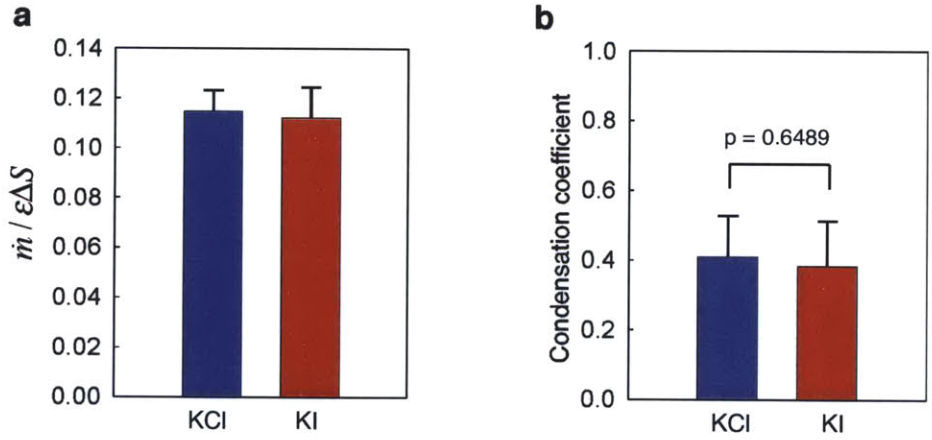

Figure 26. Effect of interchanging of halogen ions on condensation coefficients. Nanopores with average aspect ratio of 8.5 were used with draw solutions of 0.5 M KCl and 0.5 M KI, respectively, at 30°C. a, Mass flux for different KCl concentrations, normalized by membrane porosity and by difference of evaporation rates across the membrane; b, Estimated condensation coefficients from the measured mass flux. The error bars denote ±S.D. including the effect of uncertainty in pressure inside the nanopores, p (See Appendix D). The condensation coefficients from KCl and KI are not significantly different based on the Student t-test (p value > 0.05).

4.7. Effect of non-condensable gas on condensation of water

From previous experimental studies, it was observed that any trace-amount of non-condensable gas near liquid/vapor interfaces, typically air, could reduce the rate of condensation

significantly[144, 145]. Since the vapor flux moves toward the interface for condensation while the non-condensable gas does not condense, the non-condensable gas accumulates near the interface as a boundary layer. Apart from diffusion resistance due to the presence of the non-condensable gas in the bulk, the relatively higher concentration of the non-condensable gas in the boundary layer increases transport resistance and it also decreases relative humidity of the water vapor, and therefore the rate of condensation decreases. The short length scale of the nanopore used in our experiments leads to negligible thickness of boundary layer inside the nanopores. For example, when typical experimental conditions such as binary diffusivity between vapor and air D_{wa} of 2.56 x 10^{-5} m^2/s under 1 bar and at temperature of 300 K, mean flow velocity u of water vapor ~10 mm/s, the approximate boundary layer thickness δ can be obtained from scaling analysis, i.e., $\delta \sim D/u \sim 2.56 \times 10^{-3}$ m, which far exceeds the length of the nanopores. Therefore we assume that the effect of the accumulation of air is negligible and the diffusion resistance which is already considered in Section 4.3.2 is the dominant transport resistance.

Chapter 5. Conclusion

5.1. Summary

We have proposed a new approach for desalination of water using pressure-driven transport through hydrophobic membranes. Pore diameters in the range of 10 nm are adequate to sustain the applied pressure for desalination of seawater. Theoretical analysis of transport through these membranes shows that the pore aspect ratio and the probability of condensation of water molecules incident on the water meniscus are the key factors that determine the flux. The flux is largely governed by condensation coefficient for short pores while the flux becomes independent of the condensation coefficient and corresponds to Knudsen flux as the aspect ratio becomes larger. The nanopore aspect ratio over which merging of two interfaces is energetically unfavorable is utilized as a design condition for nanopore membrane. Based on this criterion, the analysis suggests that the proposed method has the potential to provide high flux membranes at moderately elevated temperature with the added advantage of decoupling the material properties from the transport properties, which may allow for the development of chlorine-resistant and high boron rejection membranes. Further development of this technique may lead to improved membranes for desalination by reverse osmosis.

We experimentally investigated the transport of water across short hydrophobic nanopores flanked by liquid-vapor interfaces. We fabricated osmosis membranes based on nanoporous alumina consisting of nanopores of ~100 nm in diameter. By hydrophobic modification on part of the inner surface of the nanopores, we created hydrophobic nanopores of tunable lengths. The integrity of the fabricated membranes was proved by exclusion of gold nanoparticles in an aqueous solution from the hydrophobic pore region, complete separation of two different dyes across the membranes, and non-wetting of the thin hydrophobic layer. The measured electrical impedance revealed defect rates less than 0.1 %.

The fabricated osmosis membranes were characterized by forward osmosis experiments where KCl was used as a draw solution. We verified vapor-phase transport across the membranes by showing rejection of non-volatile dye while water was transported. Measurements of the osmotic flow of water for different pore aspect ratios, osmotic pressures, and temperatures demonstrate the existence of a mass transport regime governed by resistance of the liquid-vapor interface, which is determined by interplay between the condensation coefficient of water and the transmission resistance across the pores. To accurately estimate the role of each resistance, we derived the effective transmission probability of water vapor based on dusty-gas model in the presence of air, which was assumed to be non-condensable and therefore stationary. As predicted in the theoretical investigation, the resistance of the interface is a governing factor for vapor transport through nanopores of small length, while the resistance becomes negligible compared to that of diffusion (transmission) for long nanopores.

We estimated the magnitude of the condensation coefficient of water at different temperatures under isothermal conditions, and found that it decreases with increasing temperature. The condensation coefficient showed no noticeable dependency on concentration and type of salt considered in this study. These findings would also lead to better understanding and prediction of mass transfer through nanofluidic devices, droplets and bubbles, biological components with two-phase interfaces, and porous media. Beyond fundamental understanding, the accurate estimation of the value of condensation coefficient will benefit solving engineering challenges. One example is water management problem in Proton Exchange Membrane Fuel Cell (PEMFC) which has been attracting attention for applications of alternative and environmental friendly power generation and transportation[146, 147]. While poor maintenance of water contents in the membrane resulting in flooding or drying impairs the performance[148], a better prediction of water concentration based on accurate condensation coefficient will lead to better maintenance of high efficiency with time. We believe that this accurate value of condensation coefficient will lead to

improvement of weather prediction such as cloud and smog formation[149], and of thermal management applications[150] as well.

5.2. Large scale membrane fabrication for RO applications

Although we showed that this approach of desalination will allow high flux, high selectivity, and material independence from transport property based on forward osmosis experiments, the effectiveness for reverse osmosis needs to be proved. Currently the alumina-based membrane with a thickness of 50 μm is too brittle to sustain high pressure applied for reverse osmosis. In addition, the flow rate through small area is difficult to measure reliably. Therefore a novel membrane fabrication methodology for flexible and large-scale membranes should be explored.

The thin active layer consisting of delicate cylindrical nanopore geometry with such flexibility could be manufactured using block-copolymers. Due to the simple realization and sophisticated architecture of regular nanostructures in a large scale based on self-assembly nature[151-154], block-copolymers have been extensively investigated and have found wide applications from drug delivery[155, 156], nanocomposite[157-159], nanoreactors[160, 161], artificial muscles[162] to nanoporous membranes[163, 164]. In particular, a number of fabrication studies of membranes consisting of cylindrical nanopores have been reported where one type of block forms the membrane matrix while the other block assumes cylindrical shapes that are later etched, leaving nanopores with diameter down to ~ 10 nm[165-168]. Thin active layer consisting of hydrophobic nanopores on supportive layer would be one promising way to fabricate the flexible vapor-trapping membranes on a large scale.

The hydrophobic, vapor permeable active layers do not have to be regularly structured, as long as the transport is equivalent to membranes with hydrophobic nanopores. Flows in porous media are

ubiquitous in aquifer, oil reservoirs, soil and rock flows and have been one of the most common classical fluid mechanics problems due to their importance in various applications from oil and gas extraction, fuel cell, porous electrodes, biological flows, water treatment, and desalination[169-171]. For vapor transport, relatively random hydrophobic porous media should provide passages for water vapor molecules similar to the more structured cylindrical pores explored here, although the effective passage length would be longer due to the greater tortuosity. Nevertheless, porous media are often relatively straightforward to fabricate compared to regular nanostructures and are therefore more suited for mass production purpose. One possible way that is currently considered is deposition of hydrophobic nanoparticles on hydrophilic supportive layer using electrophoretic deposition (EPD)[172]. PDMS coated silica nanoparticles with 14 nm diameter (PlasmaChem) have been deposited on commercially available highly porous nylon membranes (Sterlitech) and annealed for stabilization and robust bonding among the particles. The transmission probability of vapor molecules through the porous layer created by the nanoparticles can be calculated from Monte-Carlo simulation. We assume that the porous layer is randomly packed by identical spherical nanoparticles, which results in porosity of 0.36 – 0.44[170]. The permeability predicted from the Monte-Carlo simulations based on this configuration needs to be experimentally tested. Currently, the control over uniformity of thin layer of nanoparticle deposition using EPD is not optimized. While the thin layer should lead to higher vapor permeability, it also increases chance of defects.

Not only for having thin active layer, but also for chlorine resistant membrane, hydrophobic surface modification on membranes made of chlorine-resistant polymer such as Polyvinylidene Fluoride (PVDF) may be one possible way for simple large area production. Typically PVDF based membranes are hydrophobic. However, Elimelech's group has carried out extensive works on development of PVDF membranes that have tunable hydrophobicity and hydrophilicity[173].

Hydrophobic surface modification on the surface of such hydrophilic PVDF membranes will be a promising way of fabricating chlorine resistant, high flux, and flexible vapor-trapping membrane.

Finally, we are also now trying a novel fabrication process using two different silanes. This process has been applied to relatively thick and rigid 2-inch circular membranes made of TiO_2 nanoparticles (Sterlitech). Hydrophilic silane such as aminosilane is first deposited on the nanoparticles at the surface of and inside the membrane. Then the top surface of membrane is briefly exposed to air plasma to destroy the hydrophilic silane in the top layer, followed by silanization using hydrophobic silane. This method seems most promising and simplest among the fabrication approaches we have discussed. We are currently optimizing this fabrication process with different silanes.

5.3. Boron rejection

As reviewed in Introduction, RO based seawater desalination does not satisfy the WHO guideline for boron rejection (1 mg/L or less in permeate). Since boron exists as boric acid at neutral pH and not as an ion, multiple stage RO at increased pH or dilution with boron-free water is typically used to meet the guideline. Therefore one stage RO that can remove boron to a satisfactory level will greatly simplify the process and save the operation and installation costs. In vapor-trapping membrane, all volatile compounds will go through, including boric acid. The permeability is approximately proportional to the equilibrium vapor pressure of each component, assuming that the interface resistance is negligible compared to the transmission resistance. The equilibrium vapor pressure of boric acid is typically ~ 10 times less than that of water. From the fact that typical boron concentration of seawater is ~ 4.5 ppm[174], 10 times slower boron flux than water vapor will easily meet the WHO guideline for boron concentration in the permeate.

5.4. Limitations & Outlook

The vapor-trapping membranes have several limitations. First, from the principle of the separation, the high selectivity of the membrane is applied only to non-volatile components. Therefore if the contaminants are volatile, i.e., alcohol, they will permeate through the membrane and additional pretreatment or post-treatment will be necessary to remove them before the feed is introduced to the membrane or after reverse osmosis. As discussed in the boron rejection, however, the flux of the volatile substances is approximately proportional to the equilibrium vapor pressure assuming that the transmission resistance is dominant. Therefore reasonable and even high selectivity can be realized especially for substances of low vapor pressure, i.e., boric acid.

Second, the hydrophobic active layer should be extremely thin (< 100 nm) for a reasonable water flux to compete with conventional RO membrane. Although the flux can be enhanced by increasing membrane porosity, high porosity of membrane may be subject to mechanical compression due to the large applied pressure, which eventually reduces the porosity. In addition, in realistic sense, there is a high chance that large-scale membrane can be achieved by incorporating randomly porous media. Therefore the corresponding high tortuosity will lead to effectively long pathways for the vapor molecules to travel, increasing transmission resistance given the same membrane thickness. However, as stated in the Section 5.2, novel fabrication approaches for low cost, large scale, regular nanostructures will realize a competent vapor-trapping membrane. One of the drawbacks of conventional RO membranes is that the RO membrane soften, creep, and fails at high temperatures and therefore typically operation above 45°C is not recommended[175, 176]. Furthermore, the salt permeability increases 3 – 5 % with increase of temperature of 1°C[177]. In principle, the flux through vapor-trapping membranes is

enhanced by higher temperature without compromising the selectivity. Although we found that the condensation coefficient of water decreases with temperature and therefore that compromises the enhancement of vapor pressure at high temperature, the vapor-trapping membrane certainly has the advantage of tolerating high temperature feed water, compared to conventional RO membrane. The high temperature tolerance and chemical resistance may make the vapor-trapping membrane suitable for high-temperature separation of corrosive solutions in industrial applications such as separation of acids or hot salt solutions, concentration of sugar solutions, etc.

Lastly, it should be mentioned that the maintaining hydrophobicity is the critical factor to operate the membrane. As shown in Section 3.3, the hydrophobicity of the silane-treated alumina membrane surface degrades with time. Once the defect rates exceed a certain point, then the salt leakage through the defects cannot be tolerable for reasonable drinking water salinity (< ~500 ppm). If the membrane is to be made of hydrophobic porous media, the Laplace pressure for the smallest effective pore size should be larger than applied pressure to prevent wetting. Fabrication of robust hydrophobic surface even in harsh condition is now a very active research area[97] and further technological progress may help to address this issue.

In conclusion, we believe that this new approach for desalination would address, at least, some of the current issues of reverse osmosis membranes and therefore lead to membranes with high permeate flux, high selectivity, and high chlorine resistance. These improved membrane properties are also expected to significantly advance other membrane-based separation technologies such as food processing[178], waste-water treatment[179] as well as energy generation technologies including pressure-retarded osmosis[180].

Appendices

A. Effect of meniscus curvature on the transmission probability

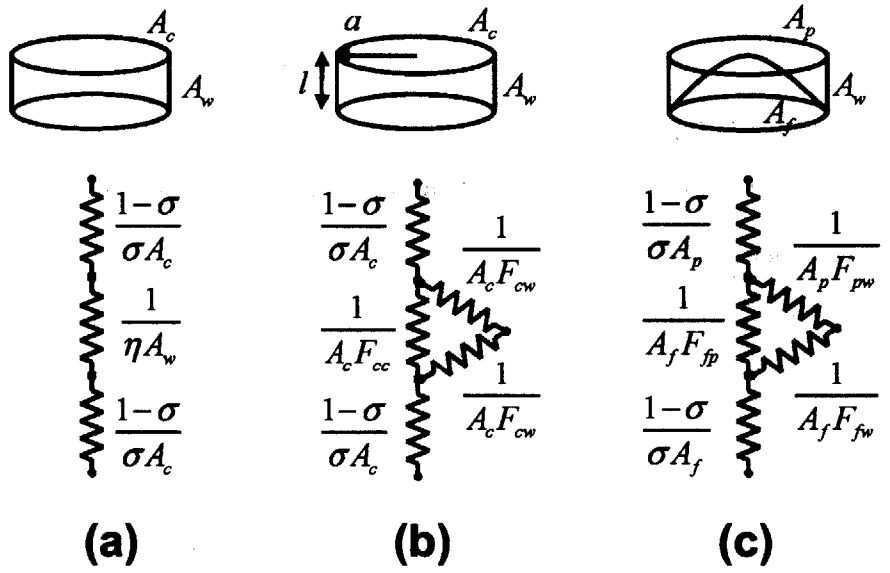

Figure 27. Resistance networks for estimating the effect of meniscus curvature on transmission probability using the radiation heat transfer analogy. A_c, A_w, A_f, and A_p denote the area of cross section of pore, pore wall, menisci at feed and permeate sides, respectively. F_{cc} and F_{cw} indicate view factors between the two menisci, and a meniscus and the pore wall, respectively, for flat interfaces. F_{fp}, F_{fw} and F_{pw} denote view factors between the menisci at feed and permeate sides, the meniscus at feed side and the pore wall, and between the meniscus at permeate side and the pore wall, respectively, assuming that the meniscus on the feed side is curved (maximum possible curvature at a contact angle of 120°) and that on the permeate side is flat. F_{cc} and F_{cw} indicate view factors between the two menisci, and from a meniscus to the pore wall, respectively, for flat interfaces. F_{fp}, F_{fw} and F_{pw} denote view factors from the meniscus on the feed side to that on the permeate side, from the meniscus on the feed side to the pore wall, and from the meniscus on the permeate side to the pore wall, respectively, assuming that the meniscus on the feed side is curved (maximum possible curvature at a contact angle of 120°) while that on the permeate side is flat.

The net mass flux may be affected by the meniscus curvature because the larger surface can emit a larger number of molecules and the scattering between the meniscus and the pore wall may be different compared with a flat meniscus. Clausing[50] obtained integral equation for transmission probability η of pore connecting two reservoirs with different pressures. Therefore η includes the effect of variation of incidental rate and directions of molecules on the pore wall. When we use heat radiation analogy to calculate the mass flux, we employ view factors F's to obtain mass

transport resistance across the pore instead of using η. However, this approach assumes a certain mean pressure (it is analogous to assuming that an insulating surface is at a uniform temperature) along the entire length of the pore. This assumption is valid for short pores, but fails for longer pores. The heat transfer analogy can account for meniscus curvature using view factors, and we therefore compare the difference in transmission probability introduced by the curvature using the heat transfer analogy. Figure 27 shows three different mass transport resistance networks for small l/a corresponding to pores with flat and curved menisci. The first case corresponds to flat menisci and the exact transmission resistance obtained from η. The second case corresponds to flat menisci and transmission resistance obtained using view factors from the heat transfer analogy. The third case corresponds to a curved meniscus on one side and transport resistances obtained using the heat transfer analogy.

Assuming contact angle of 120°, the aspect ratio at which meniscus at feed side touches the other side is $l/a = 0.27$. At this pore length, the difference of mass flux between the case employing η (Figure 27a) and that using view factors (Figure 27b) is less than 0.1%. The mass flux for curved meniscus configuration by using view factors (Figure 27c) is about 3% larger than the former two cases for σ ranging from 0 to 1. The curved surface modestly increases the mass flux due to the increased emission surface area, but it is offset by the altered view factors. This tendency is similar when $l/a = 0.81$, where the mass flux is slightly increased (~3.5%) compared to the case using η with flat meniscus assumed.

When l/a becomes larger, for example $l/a > 3$, the difference between the mass fluxes obtained by employing η and view factors for flat surfaces becomes larger. However, the mass fluxes for the curved and flat surfaces by using view factors are still within 3%. Therefore it would be reasonable to conclude that the effect of the curved surface on mass flux is negligible to within 5%.

B. Temperature difference across a membrane incorporating vapor-trapping nanopores

The membrane material and porosity are important considerations for minimizing the temperature difference across the membrane. Membrane porosity is defined as the void fraction of the whole membrane volume. Since the membrane considered here is assumed to have straight cylindrical pores, the porosity is the same as the ratio of total cross section area of pores to membrane surface area. Typically, commercial membrane porosity ranges from 20% to 60%. The mass flux through the pore will increase with porosity, but the temperature difference between feed and permeate sides will become larger due to the latent heat transfer by evaporation and condensation. Then the vapor pressure at feed side will therefore decrease and it will reduce the vapor transport. Conduction through the non-porous part on the membrane is needed for maintaining nearly isothermal conditions. When the heat transfer by evaporation and condensation is balanced by heat conduction through the membrane, we have:

$$\Delta T = \frac{\dot{m} h_{fg} l}{k\left(1 - A_{pore} / A_{total}\right)}, \tag{52}$$

where A_{total} and A_{pore} are total membrane area and total area occupied by pores, respectively. $\dot{m}$ is the mass flux per unit total area, which can be obtained from Equation. (22) and membrane porosity. h_{fg} is latent heat of vaporization of water, k is the thermal conductivity of the membrane material, ΔT is temperature difference across the membrane, and l denotes membrane thickness or the length of the pores. For example, the vapor pressure difference at 20°C across the membrane by applying 50 bar on the feed side is 35 Pa. Based on polytetrafluoroethylene membrane of thermal conductivity[181] of 0.27 W/m·K as one possible material with 40% porosity, $\sigma = 1.0$, $a = 5$ nm, and $l = 20$ nm (note that $(l/a)_{\min} = 3.1$), the mass flux is 5.4 g/m^{2}s when the salt concentration

is 0.62 M NaCl. The temperature difference obtained by balancing heat conduction and latent heat transport is 0.0016°C. This temperature difference reduces the vapor pressure difference by 0.7%. As another example, with a temperature of 50°C and the same pore radius, the vapor pressure difference induced by the latent heat transport decreases by 2.9% at l = 20 nm, 3.9% at l = 50 nm, 4.4% at l = 100 nm, and by 5.4% at l = 5μm. Figure 28 shows the decrease in vapor pressure difference for temperature of 50°C and the same σ, salt concentration, and porosity as pore radius and length vary with an aspect ratio larger than $(l/a)_{min}$. For a given pore length, the decrease is smaller with smaller pore radius due to lower flux. Therefore membranes with smaller pore size and length are more preferable. The maximum variation does not exceed 12.5% based on a thermal conductivity of 0.27 W/m·K, and is correspondingly lower for membrane materials with higher thermal conductivities. In the present study, we therefore neglect the temperature gradient effect and assume isothermal transport.

C. Estimation of average aspect ratio

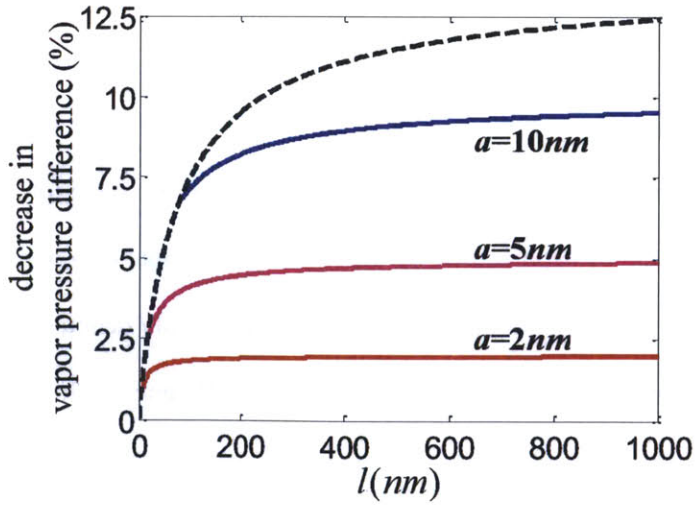

Figure 28. Decrease in vapor pressure difference across a membrane with thermal conductivity of 0.27 W/m-K. Applied pressure of 50 bar, temperature of 50°C, NaCl concentration of 0.62 M, condensation probability of 1.0, and porosity of 40% are assumed. Dashed line indicates the vapor pressure difference variation at minimum aspect ratio $(l/a)_{min}$.

SEM images of membrane surface provide porosity and equivalent diameters of nanopores. The equivalent diameter for each nanopore was assumed to be the diameter of a circle having the same cross-section area as the nanopore. From about 30 SEM images, the equivalent radii a_j (half the equivalent diameter, $j = 1, \ldots, N$; $N \sim 3{,}000$) were obtained and assumed to be representative for the all membranes tested.

Membranes were fabricated in batches, with one membrane in each batch being reserved for characterization. To obtain average AR for each batch after the same duration of plasma etching, a reference membrane was broken and etch depths l_i were measured at 5 – 10 different locations from SEM images of membrane cross-section (see Figure 11d). After sets of ARs $AR_{ij} \equiv l_i / a_j$ were created for each l_i, equivalent average ARs ($\overline{AR_i}$) were obtained such that the average of calculated flux from all the individual nanopores with the corresponding ARs is matched with the calculated flux from a membrane of average porosity ε consisting of nanopores having an equivalent $\overline{AR_i}$ and an average radius $\bar{a}$ as follows:

$$\frac{\sum_{j=1}^{N} fr\left(AR_{ij}, a_j, \sigma, T, C, p_0\right)}{\sum A_m} = flux\left(\overline{AR_i}, \bar{a}, \varepsilon, \sigma, T, C, p_0\right), \tag{53}$$

where $fr\left(AR_{ij}, a_j, \sigma, T, C, p_0\right)$ is predicted mass flow rate from individual nanopore with AR_{ij} and a_j. p_0 is the estimated average pressure inside the nanopores as stated in Chapter 4.1.2, i.e., p_0 = 0.5 bar. A_m's are areas of the membranes that were imaged and where pore diameter information was gathered. $flux\left(\overline{AR_i}, \bar{a}, \varepsilon, \sigma, T, C, p_0\right)$ is the calculated mass flux with $\overline{AR_i}$, $\bar{a}$ and ε. Note that the flux is also a function of condensation coefficient σ which is unknown. However any reasonable selection of σ (0.1 – 0.5) results in not more than 1% difference in the final value of average AR ($\overline{AR}$). With the other parameters remained the same, Newton-Rhapson iterative

method was used to find $\overline{AR_i}$. Finally, the average of $\overline{AR_i}$ was regarded as the average AR ($\overline{AR}$) with corresponding standard deviation.

D. Estimation of the condensation coefficient

Condensation coefficients (σ) shown in Figure 23 were estimated as follows. To find the best-fit value of σ while taking into account the effects of concentration on the fluxes, all the measured mass fluxes for each average AR ($\overline{AR}$) were divided by the corresponding osmotic pressure differences, i.e., $\dot{m}_{meas}\left(\overline{AR},C,T\right)/\Delta\Pi(C,T)$ with fixed temperature T. Then, the predicted fluxes for the same $\overline{AR}$ were also divided by the same osmotic pressure differences, i.e., $\dot{m}_{\text{model}}\left(\overline{AR},\bar{a},\varepsilon,C,T,\sigma,p\right)/\Delta\Pi(C,T)$ where p is estimated air concentration (pressure) inside the nanopores, i.e., $p = p_0 \pm \Delta p$ where p_0 = 0.5 bar and Δp = 0.3 bar. The best-fit σ (σ_{fit}) was identified as the value that minimized sum of the squares of differences in those two values, i.e., $\min\left\{\sum_{\overline{AR},C,membranes}\left[\dot{m}_{\text{model}}\left(\overline{AR},\bar{a},\varepsilon,C,T,\sigma_{fit},p_0\right)/\Delta\Pi(C,T)-\dot{m}_{\text{meas}}\left(\overline{AR},C,T\right)/\Delta\Pi(C,T)\right]^2\right\}$. As a result, σ_{fit} was obtained as 0.23 at 39.0°C (Figure 23a).

In Figure 23a, mass flux $\dot{m}$ was normalized by that with zero interface resistance, i.e., $\dot{m}_{\sigma=1}$. While we use $\dot{m}=\dot{m}_{meas}$ and $\dot{m}_{\sigma=1}=\dot{m}_{\text{model},\sigma=1}$, the normalized value $\dot{m}_{meas}/\dot{m}_{\text{model},\sigma=1}$ has uncertainties due to the uncertainty in p. The uncertainty in $\dot{m}_{meas}/\dot{m}_{\text{model},\sigma=1}$, i.e., $\Delta\left(\dot{m}_{meas}/\dot{m}_{\text{model},\sigma=1}\right)$ was estimated as follows. For each $\overline{AR}$ and C at T = 39.0°C, standard deviation of measured mass flux was regarded as an uncertainty, $\Delta\dot{m}_{meas}$, about the mean value of measured mass flux, $\overline{\dot{m}_{meas}}$. Uncertainty of $\dot{m}_{\text{model},\sigma=1}$, i.e., $\Delta\dot{m}_{\text{model},\sigma=1}$ was estimated as a

maximum value of differences between model prediction at $p = p_0$ and $p = p_0 \pm \Delta p$, i.e., $\Delta \dot{m}_{\text{model},\,\sigma=1} = \max\left\{\left|\dot{m}_{\text{model},\,\sigma=1,p=p_0} - \dot{m}_{\text{model},\,\sigma=1,p=p-\Delta p}\right|, \left|\dot{m}_{\text{model},\,\sigma=1,p=p_0} - \dot{m}_{\text{model},\,\sigma=1,p=p+\Delta p}\right|\right\}$. Since both $\dot{m}_{meas}$ and $\dot{m}_{\text{model},\,\sigma=1}$ are dependent on p, the uncertainty of $\dot{m}_{meas} / \dot{m}_{\text{model},\,\sigma=1}$ can be estimated as[182]:

$$\Delta\left(\frac{\dot{m}_{meas}}{\dot{m}_{\text{model},\,\sigma=1}}\right) = \frac{\overline{\dot{m}_{meas}}}{\dot{m}_{\text{model},\,\sigma=1,p=p_0}} \cdot \left[\left|\frac{\Delta\dot{m}_{meas}}{\overline{\dot{m}_{meas}}}\right| + \left|\frac{\Delta\dot{m}_{\text{model},\,\sigma=1}}{\dot{m}_{\text{model},\,\sigma=1,p=p_0}}\right|\right] = \frac{\Delta\dot{m}_{meas}}{\dot{m}_{\text{model},\,\sigma=1,p=p_0}} + \frac{\overline{\dot{m}_{meas}} \cdot \Delta\dot{m}_{\text{model},\,\sigma=1}}{\dot{m}^2_{\text{model},\,\sigma=1,p=p_0}} \tag{54}$$

Note that the first term in the right-hand side represents the standard deviation of $\dot{m}_{meas} / \dot{m}_{\text{model},\,\sigma=1}$ for $\Delta p = 0$. Figure 29b (same as Figure 23a) shows the distribution of $\dot{m}_{meas} / \dot{m}_{\text{model},\,\sigma=1}$ taking into account the uncertainty of p, while Figure 29a,c depict the two extreme cases corresponding to $p = 0 \pm 0.0$ bar and $p = 1 \pm 0.0$ bar, respectively.

The uncertainty of $\psi \equiv R_i / R_t = 0.5\left(\dot{m}_{\sigma=1} / \dot{m} - 1\right)$ was estimated in the same way. The mean values $\bar{\psi}$'s for each $\overline{AR}$ were obtained as:

$$\bar{\psi} = \overline{\left(\frac{R_i}{R_t}\right)} = 0.5\left[\overline{\left(\frac{\dot{m}_{\text{model},\,\sigma=1}}{\dot{m}_{meas}}\right)} - 1\right], \tag{55}$$

where $\overline{\left(\dot{m}_{\text{model},\,\sigma=1} / \dot{m}_{meas}\right)}$ is the mean value of $\dot{m}_{\text{model},\,\sigma=1,p=p_0} / \dot{m}_{meas}$ for different concentrations with the same $\overline{AR}$. As shown in Equation (54), because both $\dot{m}_{\text{model},\,\sigma=1}$ and $\dot{m}_{meas}$ are dependent on p, the uncertainty of $\dot{m}_{\text{model},\,\sigma=1} / \dot{m}_{meas}$ is:

$$\Delta\left(\frac{\dot{m}_{\text{model},\,\sigma=1}}{\dot{m}_{meas}}\right) = \Delta\left(\frac{\dot{m}_{\text{model},\,\sigma=1} / \Delta\Pi}{\dot{m}_{meas} / \Delta\Pi}\right) = \overline{\left(\frac{\dot{m}_{\text{model},\,\sigma=1}}{\dot{m}_{meas}}\right)} \cdot \left[\left|\frac{\Delta\left(\dot{m}_{meas} / \Delta\Pi\right)}{\overline{\dot{m}_{meas} / \Delta\Pi}}\right| + \left|\frac{\Delta\left(\dot{m}_{\text{model},\,\sigma=1} / \Delta\Pi\right)}{\dot{m}_{\text{model},\,\sigma=1,p=p_0} / \Delta\Pi}\right|\right] \tag{56}$$

Note that $\dot{m}/\Delta\Pi$ is independent of concentration. Figure 29e (same as Figure 23b) shows the distribution of ψ where the uncertainties from p are introduced, compared to Figure 29d,f for p = 0 and p = 1bar, respectively, without including the uncertainty in p.

For calculating σ at each $\overline{AR}$ shown in Figure 23c, an iterative method was first used until condensation coefficients assuming $\Delta p = 0$, i.e., σ_0's were found to match $\dot{m}_{\text{model}}\left(\overline{AR},\bar{a},\varepsilon,C,T,\sigma_0,p_0\right)/\Delta\Pi(C,T)$ with $\dot{m}_{meas}\left(\overline{AR},C,T\right)/\Delta\Pi(C,T)$. These σ_0 values were obtained for different concentrations in 3 – 5 different membranes with the same $\overline{AR}$.

To include the effect of uncertainty in p, mass flux $\dot{m}=\dot{m}\left(\overline{AR},\bar{a},\varepsilon,C,T,\sigma,p\right)$ for fixed temperature can be expressed as a following function:

$$\frac{\dot{m}}{\Delta\Pi}=g\left(\sigma,p,x_j\right), \tag{57}$$

where x_j are the other fixed variables. If we express σ as a function of the other variables, i.e., $\sigma=f\left(\frac{\dot{m}}{\Delta\Pi},p\right)$, the differential of σ is given as follows:

$$d\sigma=\frac{\partial f}{\partial(\dot{m}/\Delta\Pi)}d(\dot{m}/\Delta\Pi)+\frac{\partial f}{\partial p}dp. \tag{58}$$

Since we defined σ_0 as condensation coefficient obtained by assuming $p = p_0$, the first term in right-hand side is equivalent to $d\sigma_0$. Therefore the above equation can be modified further as:

$$d\sigma=d\sigma_0-\frac{\partial(\dot{m}/\Delta\Pi)}{\partial p}\left[\frac{\partial(\dot{m}/\Delta\Pi)}{\partial\sigma}\right]^{-1}dp, \tag{59}$$

where cyclic chain rule was used. Since $\dot{m}/\Delta\Pi$ and p are now independent variables, σ_0 and p are also independent to each other. Then the uncertainty of σ, i.e., $\Delta\sigma$, can be estimated as[s182]:

$$\Delta\sigma = \sqrt{(\Delta\sigma_0)^2 + \left\{\frac{\partial(\dot{m}/\Delta\Pi)}{\partial p}\left[\frac{\partial(\dot{m}/\Delta\Pi)}{\partial\sigma}\right]^{-1}\Delta p\right\}^2}\,. \tag{60}$$

The partial derivatives are evaluated at $p = p_0$ and $\sigma = \bar{\sigma}$, where $\bar{\sigma}$ and $\Delta\sigma_0$ are the mean value and standard deviation of σ_0 for each $\overline{AR}$, respectively. The distributions of σ including the error propagation from uncertainty of p are shown in Figure 29h (same as Figure 23c). It can be noticed that the change in $\Delta\sigma$ becomes more significant for larger $\overline{AR}$ because the effect of uncertainty in transmission resistance is more prominent in long nanopores.

The σ values for different temperatures were obtained in the same way based on the data measured with 1 M KCl and average AR of 9.6 ± 0.7. An iterative method was used again to find the distribution of σ's that match $\dot{m}_{\text{model}}\left(\overline{AR},\bar{a},\varepsilon,C,T,\sigma,p_0\right)/\Delta\Pi(C,T)$ with $\dot{m}_{meas}\left(\overline{AR},C,T\right)/\Delta\Pi(C,T)$ for different temperatures (Figure 23c). Then, the uncertainty of σ including the uncertainty in p was included in the same way as above, and the distributions of σ's are shown in Figure 29k (same as Figure 23d).

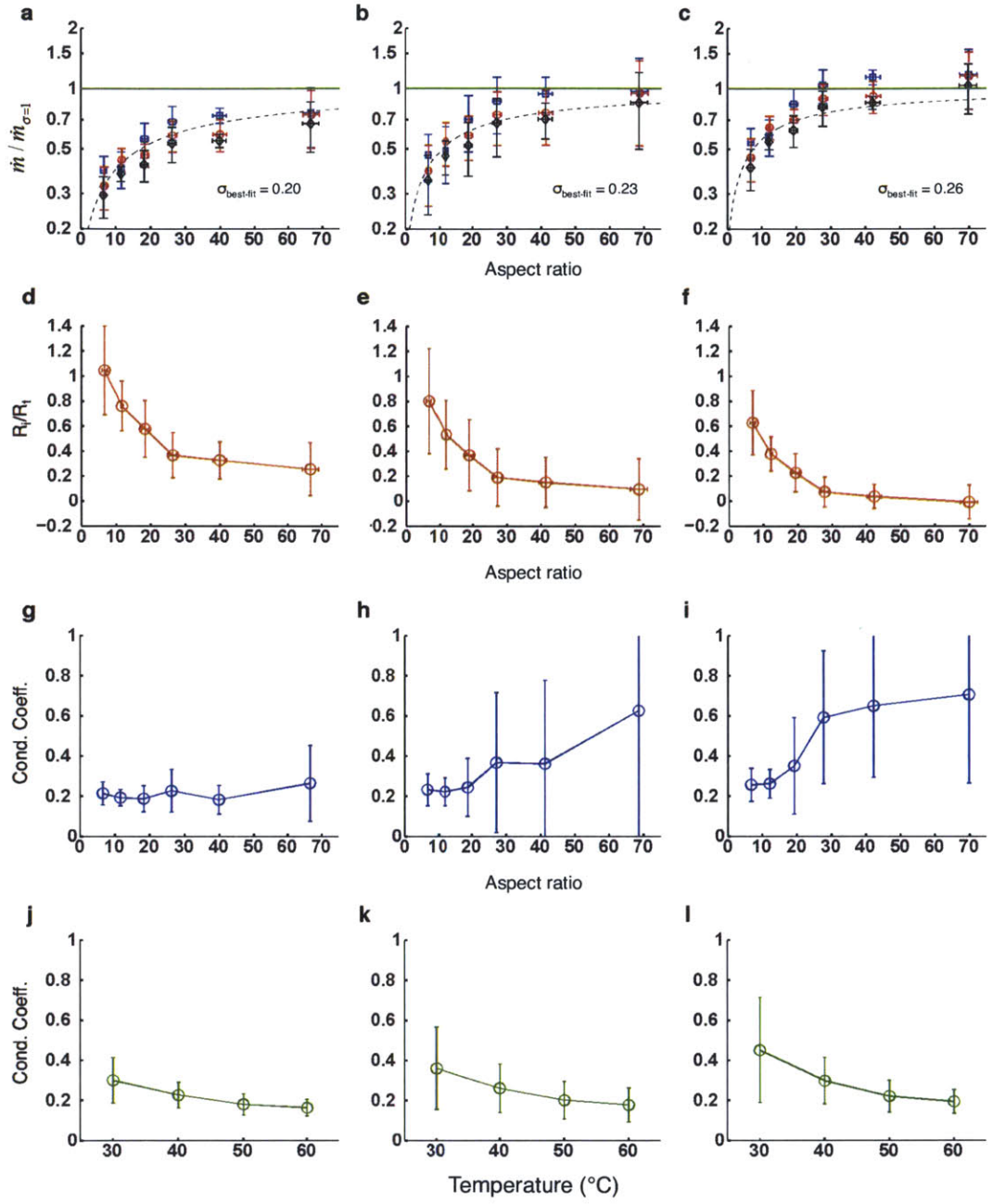

Figure 29. Effect of air pressure inside the nanopores. a, b, c Mass flux normalized by that with zero interface resistance for (a) $p = 0\pm0.0$ bar; (b) $p = 0.5\pm0.3$ bar; (c) $p = 1\pm0.0$ bar. d, e, f Ratio of R_i and R_t for different aspect ratios with (d) $p = 0\pm0.0$ bar; (e) $p = 0.5\pm0.3$ bar; (f) $p = 1\pm0.0$ bar. g, h, i Estimated condensation coefficients for different aspect ratios with (g) $p = 0\pm0.0$ bar; (h) $p = 0.5\pm0.3$ bar; (i) $p = 1\pm0.0$ bar. j, k, l, Estimated condensation coefficients for different temperatures with (j) $p = 0\pm0.0$ bar; (k) $p = 0.5\pm0.3$ bar; (l) $p = 1\pm0.0$ bar.

E. Alternative fabrication method for short hydrophobic nanopores

Short hydrophobic nanopores may be fabricated in an alternative way. Anodized aluminum oxide (AAO) membranes can be again chosen as the template for fabrication of hydrophobic membranes. Since chemical bonds are formed between thiol group and gold[183], the entrance region of the pores was coated with gold and modified with hydrophobic self-assembled alkanethiol monolayers.

The degree of hydrophobicity on the top of the monolayer is determined by the type of tail group ($-CH_2$, $-CH_3$, $-CF_2$, $-CF_2H$, $-CF_3$), with $-CF_3$ possessing the lowest surface energy[184]. We selected the hydrophobic perfluorodecanethiol (Sigma Aldrich) which has a fluorocarbon tail group for modification of the AAO membrane.

Fabrication of a thin hydrophobic membrane was realized by deposition of gold to a certain depth of the nanopores of the AAO membrane and by formation of self-assembled monolayer on the gold. The AAO membranes were placed on a rotating mechanism of a windup spring clock. Then the rotating mechanism was mounted inside the chamber of electron beam evaporator with a certain slant angle. In that way, evaporated metal can be deposited only near at the entrance of the pores (Figure 30a). About 5 nm thick titanium was evaporated first on the membrane as an adhesion layer and then 5 nm thick gold was deposited. The hydrophobic pore length and therefore hydrophobic membrane thickness could be determined by controlling the slant angle. Here, the slant angle ϕ was chosen as 20° for the gold-coated depth of about 600 nm, i.e., 200 nm/tan 20° ≈ 600 nm).

The gold-coated membranes were rinsed thoroughly with ethanol for about 20 minutes, and placed for 24 hours in 1 mM perfluorodecanethiol solution in ethanol allowing for formation of gold-thiol bond and self-assembled monolayers (Figure 30b). This procedure resulted in a membrane that was hydrophobic on one side and hydrophilic on the other side. The same self-

assembled monolayer on plane gold-coated glass slides yielded an advancing contact angle of approximately 108° (Figure 30c).

We did not continue to use this alkanethiol self-assembled monolayers for hydrophobic surface modification because thiol-Au bonds are prone to oxidation in an ambient condition[185]. In fact, we observed that the hydrophobicity of the alkanethiol-treated membranes was degraded within a week and therefore it was difficult to maintain high quality hydrophobicity.

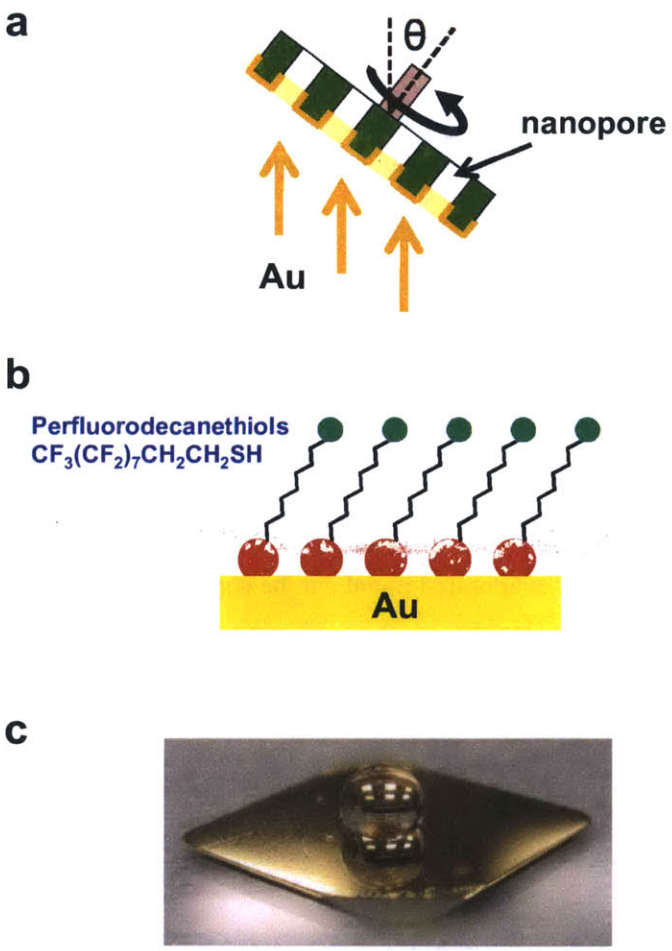

Figure 30. Fabrication method using alkanethiol self-assembled monolayers. a, E-beam evaporation of gold on rotating membrane with an angle θ. b, Schematic diagram of self-assembled monolayers formed based on thiol-gold bonding. c, Water droplet on the fabricated membrane

F. Alternative defect characterization method

Apart from electric impedance measurement, we also used a calcium ion binding fluorescent dye (Fluo-4 from Invitrogen Inc.) to characterize the defects. Fluo-4 is negatively charged salt and is used as a calcium indicator since the fluorescent light intensity is increased by a factor >100 upon binding to a calcium ion.

As shown in Figure 31a, two different solutions were introduced on either side of the hydrophobic membrane. On the top side, the solution was 0.5 mM Fluo-4 and 0.5 mM ethylenediaminetetraacetic acid (EDTA) in deionized water whereas the solution on the bottom side was 10 mM $CaCl_2$. In the presence of an electrical field across the membrane, the Fluo-4 and Ca^{2+} ions can be driven across the membrane to bind together or driven away from the membrane to be depleted and separated from each other depending on the direction of the electrical field. By capturing the light intensity modulation under an AC voltage applied across the membrane, the locations of defects (i.e., open pores) could be determined. In the experiments, amplitude of 1V and frequency of 0.2 Hz were applied across the membranes through Ag/AgCl electrodes (Figure 31a, b).

Figure 31c and e shows the fluorescence images when AC voltage was applied on a 'leaky' and 'low defect' membranes, respectively. Fluorescent spots with intensity modulated at 0.2 Hz were clearly observed where Fluo-4 and Ca^{2+} were driven through the defective wetted pores by the AC voltage bias. Fourier transform for the fluorescent light intensity was performed to detect the defective area and construct maps of defects where Fourier coefficient corresponding to the applied AC field frequency are larger than a certain threshold (Figure 31d and f).

Figure 31g indicates a time sequence of fluorescent light intensity change at a certain spot. The period of peak to peak response is 5 seconds and is exactly same as the period of the applied AC voltage. It can be also observed that the overall intensity increased with time. It may be attributed

to that a portion of Fluo-4 and Ca^{2+} diffuse to the other side far enough or bind together such that their flux is lower when the voltage is reversed, resulting in a net accumulation of fluorescence in each cycle. Based on these experiments, the ratio of wetted pores to functional pores was estimated to be less than 1%. Defect-free areas with dimensions in the range of 100-200 μm were observed, which is sufficient for measurement of transport characteristics of these membranes.

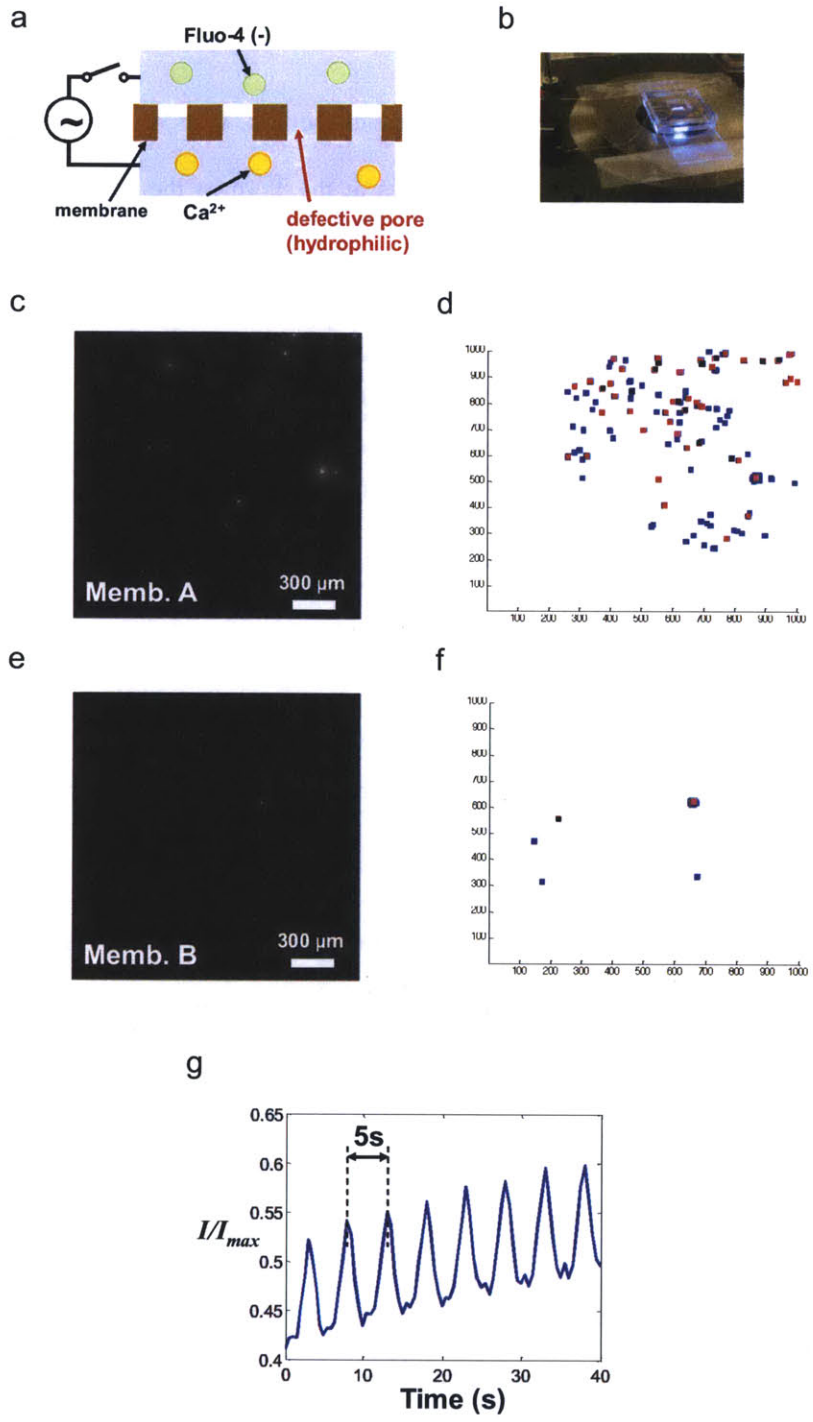

Figure 31. Defect characterization using Fluo-4. a, Schematic diagram of setup with a membrane. 0.5 mM Fluo-4 solution on the top side and 10 mM $CaCl_2$ solution on the bottom side are placed under AC electric field. b, Snapshot of the experimental setup on fluorescence microscope. c, Fluorescence image of 'leaky' membrane. d, Corresponding Fourier transformed map for fluorescence light intensity. e, Fluorescence image of 'low defect' membrane. f, Corresponding Fourier transformed map for fluorescence light intensity. g, Time trace of fluorescence light intensity normalized by a maximum intensity at a specific 'leaky' pore.

References

1. Engelman, R., Cincotta, R.P., Dye, B., Gardner-Outlaw, T. & Wisnewski, J. People in the Balance: Population and Natural Resources at the Turn of the Millennium. (Population Action International, Washington D.C.; 2000).

2. Miller, J.E. Review of water resources and desalination technologies. (Sandia National Laboratories, 2003).

3. Cincotta, R.P., Engelman, R., Anastasion, D. & Population Action International. The security demographic : population and civil conflict after the Cold War. (Population Action International, Washington, D.C.; 2003).

4. Desalination: A National Perspective. (The National Academies Press, 2008).

5. Shannon, M. et al. Science and technology for water purification in the coming decades. *Nature* **452**, 301-310 (2008).

6. Ghaffour, N., Missimer, T. & Amy, G. Technical review and evaluation of the economics of water desalination: Current and future challenges for better water supply sustainability. *Desalination* **309**, 197-207 (2013).

7. Humplik, T. et al. Nanostructured materials for water desalination. *Nanotechnology* **22** (2011).

8. Fritzmann, C., Lowenberg, J., Wintgens, T. & Melin, T. State-of-the-art of reverse osmosis desalination. *Desalination* **216**, 1-76 (2007).

9. Loeb, S. & Sourirajan, S., Vol. 3133132 (US; 1964).

10. Cadotte, J., Vol. 4277344 (US; 1981).

11. Jeong, B.H. et al. Interfacial polymerization of thin film nanocomposites: A new concept for reverse osmosis membranes. *Journal of Membrane Science* **294**, 1-7 (2007).

12. Shannon, M.A. et al. Science and technology for water purification in the coming decades. *Nature* **452**, 301-310 (2008).

13. Zhou, Y. & Tol, R. Evaluating the costs of desalination and water transport. *Water Resources Research* **41** (2005).

14. Veerapaneni, S., Long, B., Freeman, S. & Bond, R. Reducing energy consumption for seawater desalination. *Journal American Water Works Association* **99**, 95-+ (2007).

15. Glater, J., Hong, S.K. & Elimelech, M. The Search for a Chlorine-Resistant Reverse-Osmosis Membrane. *Desalination* **95**, 325-345 (1994).

16. Cardew, P.T. & Le, M.S. Membrane Processes. (Royal Society of Chemistry, Cambridge; 1999).

17. Soltanieh, M. & Gill, W.N. Review of Reverse-Osmosis Membranes and Transport Models. *Chemical Engineering Communications* **12**, 279-363 (1981).

18. Magara, Y., Tabata, A., Kohki, M., Kawasaki, M. & Hirose, M. Development of boron reduction system for sea water desalination. *Desalination* **118**, 25-33 (1998).

19. Taniguchi, M., Kurihara, M. & Kimura, S. Boron reduction performance of reverse osmosis seawater desalination process. *Journal of Membrane Science* **183**, 259-267 (2001).

20. Greenlee, L., Lawler, D., Freeman, B., Marrot, B. & Moulin, P. Reverse osmosis desalination: Water sources, technology, and today's challenges. *Water Research* **43**, 2317-2348 (2009).

21. Glueckstern, P. & Priel, M. Optimization of boron removal in old and new SWRO systems. *Desalination* **156**, 219-228 (2003).

22. Rao, A.P., Joshi, S.V., Trivedi, J.J., Devmurari, C.V. & Shah, V.J. Structure-performance correlation of polyamide thin film composite membranes: effect of coating conditions on film formation. *Journal of Membrane Science* **211**, 13-24 (2003).

23. Holt, J.K. et al. Fast mass transport through sub-2-nanometer carbon nanotubes. *Science* **312**, 1034-1037 (2006).

24. Hummer, G., Rasaiah, J.C. & Noworyta, J.P. Water conduction through the hydrophobic channel of a carbon nanotube. *Nature* **414**, 188-190 (2001).

25. Wang, C. et al. Proton exchange membrane fuel cells with carbon nanotube based electrodes. *Nano Letters* **4**, 345-348 (2004).

26. Liu, Z.L. et al. Preparation and characterization of platinum-based electrocatalysts on multiwalled carbon nanotubes for proton exchange membrane fuel cells. *Langmuir* **18**, 4054-4060 (2002).

27. Striemer, C.C., Gaborski, T.R., McGrath, J.L. & Fauchet, P.M. Charge- and size-based separation of macromolecules using ultrathin silicon membranes. *Nature* **445**, 749-753 (2007).

28. Fornasiero, F. et al. Ion exclusion by sub-2-nm carbon nanotube pores. *Proceedings of the National Academy of Sciences of the United States of America* **105**, 17250-17255 (2008).

29. Lee, J. & Karnik, R. Desalination-of water by vapor-phase transport through hydrophobic nanopores. *Journal of Applied Physics* **108** (2010).

30. Srisurichan, S., Jiraratananon, R. & Fane, A.G. Mass transfer mechanisms and transport resistances in direct contact membrane distillation process. *Journal of Membrane Science* **277**, 186-194 (2006).

31. Lawson, K.W. & Lloyd, D.R. Membrane distillation .2. Direct contact MD. *Journal of Membrane Science* **120**, 123-133 (1996).

32. Lawson, K.W. & Lloyd, D.R. Membrane distillation. *Journal of Membrane Science* **124**, 1-25 (1997).

33. Mason, E.A. & Malinauskas, A.P. Gas transport in porous media : the dusty-gas model. (Elsevier, Amsterdam ; New York; 1983).

34. Cunningham, R.E. & Williams, R.J.J. Diffusion in gases and porous media. (Plenum Press, New York; 1980).

35. Beckstein, O. & Sansom, M.S.P. Liquid-vapor oscillations of water in hydrophobic nanopores. *Proceedings of the National Academy of Sciences of the United States of America* **100**, 7063-7068 (2003).

36. Giaya, A. & Thompson, R.W. Water confined in cylindrical micropores. *Journal of Chemical Physics* **117**, 3464-3475 (2002).

37. Stelzer, J., Paulus, M., Hunger, M. & Weitkamp, J. Hydrophobic properties of all-silica zeolite beta. *Microporous and Mesoporous Materials* **22**, 1-8 (1998).

38. Ramachandran, C.E., Chempath, S., Broadbelt, L.J. & Snurr, R.Q. Water adsorption in hydrophobic nanopores: Monte Carlo simulations of water in silicalite. *Microporous and Mesoporous Materials* **90**, 293-298 (2006).

39. Varanasi, K.K., Hsu, M., Bhate, N., Yang, W.S. & Deng, T. Spatial control in the heterogeneous nucleation of water. *Applied Physics Letters* **95**, 094101 (2009).

40. Cailliez, F., Stirnemann, G., Boutin, A., Demachy, I. & Fuchs, A.H. Does water condense in hydrophobic cavities? A molecular simulation study of hydration in heterogeneous nanopores. *Journal of Physical Chemistry C* **112**, 10435-10445 (2008).

41. McCool, B.A., Hill, N., DiCarlo, J. & DeSisto, W.J. Synthesis and characterization of mesoporous silica membranes via dip-coating and hydrothermal deposition techniques. *Journal of Membrane Science* **218**, 55-67 (2003).

42. Li, Y. et al. Mass and thermal accommodation coefficients of H2O(g) on liquid water as a function of temperature. *Journal of Physical Chemistry a* **105**, 10627-10634 (2001).

43. Vieceli, J., Roeselova, M. & Tobias, D. Accommodation coefficients for water vapor at the air/water interface. *Chemical Physics Letters* **393**, 249-255 (2004).

44. Morita, A., Sugiyama, M., Kameda, H., Koda, S. & Hanson, D. Mass accommodation coefficient of water: Molecular dynamics simulation and revised analysis of droplet train/flow reactor experiment. *Journal of Physical Chemistry B* **108**, 9111-9120 (2004).

45. Shaw, R. & Lamb, D. Experimental determination of the thermal accommodation and condensation coefficients of water. *Journal of Chemical Physics* **111**, 10659-10663 (1999).

46. Winkler, P. et al. Mass and thermal accommodation during gas-liquid condensation of water. *Physical Review Letters* **93** (2004).

47. SAGEEV, G., FLAGAN, R., SEINFELD, J. & ARNOLD, S. CONDENSATION RATE OF WATER ON AQUEOUS DROPLETS IN THE TRANSITION REGIME. *Journal of Colloid and Interface Science* **113**, 421-429 (1986).

48. Marek, R. & Straub, J. Analysis of the evaporation coefficient and the condensation coefficient of water. *International Journal of Heat and Mass Transfer* **44**, 39-53 (2001).

49. Eames, I., Marr, N. & Sabir, H. The evaporation coefficient of water: A review. *International Journal of Heat and Mass Transfer* **40**, 2963-2973 (1997).

50. Clausing, P. The flow of highly rarefied gases through tubes of arbitrary length. *The Journal of Vacuum Science and Technology* **8(5)**, 636-646 (1971).

51. Berman, A.S. Free Molecule Transmission Probabilities. *Journal of Applied Physics* **36**, 3356 (1965).

52. Eames, I.W., Marr, N.J. & Sabir, H. The evaporation coefficient of water: A review. *International Journal of Heat and Mass Transfer* **40**, 2963-2973 (1997).

53. Anisimov, S.I., Dunikov, D.O., Zhakhovskii, V.V. & Malyshenko, S.P. Properties of a liquid-gas interface at high-rate evaporation. *Journal of Chemical Physics* **110**, 8722-8729 (1999).

54. ROBINSON, R. & STOKES, R. TABLES OF OSMOTIC AND ACTIVITY COEFFICIENTS OF ELECTROLYTES IN AQUEOUS SOLUTION AT 25-DEGREES-C. *Transactions of the Faraday Society* **45**, 612-624 (1949).

55. Tester, J.W. & Modell, M. Thermodynamics and its applications, Edn. 3rd. (Prentice Hall, Upper Saddle River, N.J.; 1997).

56. Atkins, P.W. Physical chemistry, Edn. 5th. (W.H. Freeman, New York; 1994).

57. Klotz, I.M. & Rosenberg, R.M. Chemical thermodynamics : basic theory and methods, Edn. 6th. (John Wiley, New York; 2000).

58. Gregg, S.J. & Sing, K.S.W. Adsorption, surface area, and porosity, Edn. [U.S. (Academic Press, London, New York,; 1967).

59. Curry, J.A. & Webster, P.J. Thermodynamics of atmospheres and oceans. (Academic Press, San Diego; 1999).

60. Wex, H., Stratmann, F., Topping, D. & McFiggans, G. The Kelvin versus the Raoult Term in the Kohler Equation. *Journal of the Atmospheric Sciences* **65**, 4004-4016 (2008).

61. Mills, A.F. Heat transfer, Edn. 2nd. (Prentice Hall, Upper Saddle River, N.J.; 1998).

62. Lefevre, B. et al. Intrusion and extrusion of water in hydrophobic mesopores. *Journal of Chemical Physics* **120**, 4927-4938 (2004).

63. Vlassiouk, I., Park, C.D., Vail, S.A., Gust, D. & Smirnov, S. Control of nanopore wetting by a photochromic spiropyran: A light-controlled valve and electrical switch. *Nano Letters* **6**, 1013-1017 (2006).

64. Lum, K. & Luzar, A. Pathway to surface-induced phase transition of a confined fluid. *Physical Review E* **56**, R6283-R6286 (1997).

65. Wolf, P.H. & Siverns, S. in International Conference on Desalination Costing (Limassol; 2004).

66. Wilf, M. & Awerbuch, L. The guidebook to membrane desalination technology : reverse osmosis, nanofiltration and hybrid systems : process, design, applications and economics. (Balaban Desalination Publications, L'Aquila, Italy; 2007).

67. Mickols, W.E., Busch, M., Maeda, Y. & Tonner, J. in Proceedings of the International Desalination Association World Congress (Singapore; 2005).

68. Taniguchi, M. & Kimura, S. Estimation of transport parameters of RO membranes for seawater desalination. *Aiche Journal* **46**, 1967-1973 (2000).

69. Petersen, R.J. Composite Reverse-Osmosis and Nanofiltration Membranes. *Journal of Membrane Science* **83**, 81-150 (1993).

70. Kulkarni, A., Mukherjee, D. & Gill, W.N. Flux enhancement by hydrophilization of thin film composite reverse osmosis membranes. *Journal of Membrane Science* **114**, 39-50 (1996).

71. Kim, H.I. & Kim, S.S. Fabrication of reverse osmosis membrane via low temperature plasma polymerization. *Journal of Membrane Science* **190**, 21-33 (2001).

72. Lee, J., Laoui, T. & Karnik, R. Nanofluidic transport governed by the liquid/vapour interface. *Nature Nanotechnology* **9**, 317-323 (2014).

73. Storm, A., Chen, J., Ling, X., Zandbergen, H. & Dekker, C. Fabrication of solid-state nanopores with single-nanometre precision. *Nature Materials* **2**, 537-540 (2003).

74. Kim, M., Wanunu, M., Bell, D. & Meller, A. Rapid fabrication of uniformly sized nanopores and nanopore arrays for parallel DNA analysis. *Advanced Materials* **18**, 3149-+ (2006).

75. George, H. et al. Nanopore fabrication in amorphous Si: Viscous flow model and comparison to experiment. *Journal of Applied Physics* **108** (2010).

76. Farhoud, M. et al. Fabrication of 200 nm period nanomagnet arrays using interference lithography and a negative resist. *Journal of Vacuum Science & Technology B* **17**, 3182-3185 (1999).

77. Klein, M. et al. SiN membranes with submicrometer hole arrays patterned by wafer-scale nanosphere lithography. *Journal of Vacuum Science & Technology B* **29** (2011).

78. Cheung, C., Nikolic, R., Reinhardt, C. & Wang, T. Fabrication of nanopillars by nanosphere lithography. *Nanotechnology* **17**, 1339-1343 (2006).

79. Chen, P. et al. Atomic layer deposition to fine-tune the surface properties and diameters of fabricated nanopores. *Nano Letters* **4**, 1333-1337 (2004).

80. Bae, C. et al. Multisegmented nanotubes by surface-selective atomic layer deposition. *Journal of Materials Chemistry C* **1**, 621-625 (2013).

81. Vlassiouk, I. & Siwy, Z. Nanofluidic diode. *Nano Letters* **7**, 552-556 (2007).

82. Holt, J. et al. Fast mass transport through sub-2-nanometer carbon nanotubes. *Science* **312**, 1034-1037 (2006).

83. Nielsch, K., Choi, J., Schwirn, K., Wehrspohn, R. & Gosele, U. Self-ordering regimes of porous alumina: The 10% porosity rule. *Nano Letters* **2**, 677-680 (2002).

84. Lee, W. et al. Structural engineering of nanoporous anodic aluminium oxide by pulse anodization of aluminium. *Nature Nanotechnology* **3**, 234-239 (2008).

85. Xiao, Z. et al. Fabrication of alumina nanotubes and nanowires by etching porous alumina membranes. *Nano Letters* **2**, 1293-1297 (2002).

86. Yanagishita, T., Nishio, K. & Masuda, H. Fabrication of metal nanohole arrays with high aspect ratios using two-step replication of anodic porous alumina. *Advanced Materials* **17**, 2241-2243 (2005).

87. Vlassiouk, I., Rios, F., Vail, S., Gust, D. & Smirnov, S. Electrical conductance of hydrophobic membranes or what happens below the surface. *Langmuir* **23**, 7784-7792 (2007).

88. Smirnov, S., Vlassiouk, I. & Lavrik, N. Voltage-Gated Hydrophobic Nanopores. *Acs Nano* **5**, 7453-7461 (2011).

89. Mani, G. et al. Stability of self-assembled monolayers on titanium and gold. *Langmuir* **24**, 6774-6784 (2008).

90. Zhou, L., Guo, Y., Yagi, M., Sakurai, M. & Kameyama, H. Investigation of a novel porous anodic alumina plate for methane steam reforming: Hydrothermal stability, electrical heating possibility and reforming reactivity. *International Journal of Hydrogen Energy* **34**, 844-858 (2009).

91. Tadanaga, K., Katata, N. & Minami, T. Formation process of super-water-repellent Al2O3 coating films with high transparency by the sol-gel method. *Journal of the American Ceramic Society* **80**, 3213-3216 (1997).

92. Bard, A.J. & Faulkner, L.R. Electrochemical methods : fundamentals and applications, Edn. 2nd. (John Wiley, New York; 2001).

93. Tuteja, A., Choi, W., Mabry, J., McKinley, G. & Cohen, R. Robust omniphobic surfaces. *Proceedings of the National Academy of Sciences of the United States of America* **105**, 18200-18205 (2008).

94. Furstner, R., Barthlott, W., Neinhuis, C. & Walzel, P. Wetting and self-cleaning properties of artificial superhydrophobic surfaces. *Langmuir* **21**, 956-961 (2005).

95. Lawson, K. & Lloyd, D. Membrane distillation. *Journal of Membrane Science* **124**, 1-25 (1997).

96. Roach, P., Shirtcliffe, N. & Newton, M. Progess in superhydrophobic surface development. *Soft Matter* **4**, 224-240 (2008).

97. Azimi, G., Dhiman, R., Kwon, H., Paxson, A. & Varanasi, K. Hydrophobicity of rare-earth oxide ceramics. *Nature Materials* **12**, 315-320 (2013).

98. Cath, T., Childress, A. & Elimelech, M. Forward osmosis: Principles, applications, and recent developments. *Journal of Membrane Science* **281**, 70-87 (2006).

99. Gryta, M. Osmotic MD and other membrane distillation variants. *Journal of Membrane Science* **246**, 145-156 (2005).

100. WILHELM, E., BATTINO, R. & WILCOCK, R. LOW-PRESSURE SOLUBILITY OF GASES IN LIQUID WATER. *Chemical Reviews* **77**, 219-262 (1977).

101. Yan, R., Liang, W., Fan, R. & Yang, P. Nanofluidic Diodes Based on Nanotube Heterojunctions. *Nano Letters* **9**, 3820-3825 (2009).

102. CLAUSING, P. FLOW OF HIGHLY RAREFIED GASES THROUGH TUBES OF ARBITRARY LENGTH. *Journal of Vacuum Science & Technology* **8**, 636-& (1971).

103. Chapman, S., Cowling, T.G. & Burnett, D. The mathematical theory of non-uniform gases; an account of the kinetic theory of viscosity, thermal conduction and diffusion in gases, Edn. 3rd. (Cambridge University Press, Cambridge, Eng.; 1970).

104. Jackson, R. Transport in porous catalysts. (Elsevier Scientific Pub. Co., Amsterdam ; New York; 1977).

105. Mason, E.A. & Malinauskas, A.P. Gas transport in porous media : the dusty-gas model. (Elsevier, Amsterdam ; New York; 1983).

106. Krishna, R. & Wesselingh, J. Review article number 50 - The Maxwell-Stefan approach to mass transfer. *Chemical Engineering Science* **52**, 861-911 (1997).

107. REMICK, R. & GEANKOPL.CJ BINARY DIFFUSION OF GASES IN CAPILLARIES IN TRANSITION REGION BETWEEN KNUDSEN AND MOLECULAR DIFFUSION. *Industrial & Engineering Chemistry Fundamentals* **12**, 214-220 (1973).

108. REMICK, R. & GEANKOPL.CJ TERNARY DIFFUSION OF GASES IN CAPILLARIES IN TRANSITION REGION BETWEEN KNUDSEN AND MOLECULAR-DIFFUSION. *Chemical Engineering Science* **29**, 1447-1455 (1974).

109. POLLARD, W. & PRESENT, R. ON GASEOUS SELF-DIFFUSION IN LONG CAPILLARY TUBES. *Physical Review* **73**, 762-774 (1948).

110. EVANS, J., ABBASI, M. & SARIN, A. A MONTE-CARLO SIMULATION OF THE DIFFUSION OF GASES IN POROUS SOLIDS. *Journal of Chemical Physics* **72**, 2967-2973 (1980).

111. BERMAN, A. FREE MOLECULE TRANSMISSION PROBABILITIES. *Journal of Applied Physics* **36**, 3356-& (1965).

112. Walsh, J. Radiation from a perfectly diffusing circular disc. (Part I.). *Proceedings of the Physical Society of London* **32**, 59-71 (1920).

113. DELANEY, L., HOUSTON, R. & EAGLETON, L. THE RATE OF VAPORIZATION OF WATER AND ICE. *Chemical Engineering Science* **19**, 105-114 (1964).

114. Yip, N., Tiraferri, A., Phillip, W., Schiffman, J. & Elimelech, M. High Performance Thin-Film Composite Forward Osmosis Membrane. *Environmental Science & Technology* **44**, 3812-3818 (2010).

115. FUKUTA, N. & WALTER, L. KINETICS OF HYDROMETEOR GROWTH FROM A VAPOR-SPHERICAL MODEL. *Journal of the Atmospheric Sciences* **27**, 1160-& (1970).

116. Fuks, N.A. Evaporation and droplet growth in gaseous media. (Pergamon Press, London, New York,; 1959).

117. Alty, T. The maximum rate of evaporation of water. *Philosophical Magazine* **15**, 82-103 (1933).

118. HICKMAN, K. MAXIMUM EVAPORATION COEFFICIENT OF WATER. *Industrial and Engineering Chemistry* **46**, 1442-1446 (1954).

119. BONACCI, J., MYERS, A., NONGBRI, G. & EAGLETON, L. EVAPORATION AND CONDENSATION COEFFICIENT OF WATER, ICE AND CARBON-TETRACHLORIDE. *Chemical Engineering Science* **31**, 609-617 (1976).

120. Mills, A.F. & Seban, R.A. The Condensation Coefficient of Water. *International Journal of Heat and Mass Transfer* **10**, 1815-1827 (1967).

121. Nabavian, K. & Bromley, L.A. Condensation Coefficient of Water. *Chemical Engineering Science* **18**, 651-660 (1963).

122. CHODES, N., WARNER, J. & GAGIN, A. DETERMINATION OF CONDENSATION COEFFICIENT OF WATER FROM GROWTH-RATE OF SMALL CLOUD DROPLETS. *Journal of the Atmospheric Sciences* **31**, 1351-1357 (1974).

123. Garnier, J.P., Ehrhard, P. & Mirabel, P. Water Droplet Growth Study in a Continuous Flow Diffusion Cloud Chamber. *Atmospheric Research* **21**, 41-51 (1987).

124. HAGEN, D. et al. CONDENSATION COEFFICIENT MEASUREMENT FOR WATER IN THE UMR CLOUD SIMULATION CHAMBER. *Journal of the Atmospheric Sciences* **46**, 803-816 (1989).

125. JAMIESON, D. CONDENSATION COEFFICIENT OF WATER. *Nature* **202**, 583-& (1964).

126. Schrage, R.W. viii, 103 p. (Columbia University., New York,; 1953).

127. Maxwell, J.C. & Niven, W.D. Scientific papers. (Dover Publications, New York,; 1952).

128. VIETTI, M. & SCHUSTER, B. LASER SCATTERING MEASUREMENTS OF DROPLET GROWTH IN BINARY-MIXTURES .1. H2O AND AIR. *Journal of Chemical Physics* **58**, 434-441 (1973).

129. BARRETT, J. & CLEMENT, C. GROWTH-RATES FOR LIQUID-DROPS. *Journal of Aerosol Science* **19**, 223-242 (1988).

130. GOLLUB, J., CHABAY, I. & FLYGARE, W. LASER HETERODYNE STUDY OF WATER DROPLET GROWTH. *Journal of Chemical Physics* **61**, 2139-2144 (1974).

131. Fuchs, N.A. & Sutugin, A.G. Highly Dispersed Aerosols. (Ann Arbor Science, Ann Arbor and London; 1970).

132. Marlow, W.H. & Baltes, H.P. Aerosol microphysics II : chemical physics of microparticles. (Springer-Verlag, Berlin ; New York; 1982).

133. Vesala, T., Kulmala, M., Rudolf, R., Vrtala, A. & Wagner, P. Models for condensational growth and evaporation of binary aerosol particles. *Journal of Aerosol Science* **28**, 565-598 (1997).

134. MILLS, A. & SEBAN, R. CONDENSATION COEFFICIENT OF WATER. *International Journal of Heat and Mass Transfer* **10**, 1815-& (1967).

135. MOZURKEWICH, M. AEROSOL GROWTH AND THE CONDENSATION COEFFICIENT FOR WATER - A REVIEW. *Aerosol Science and Technology* **5**, 223-236 (1986).

136. MAEREFAT, M., AKAMATSU, T. & FUJIKAWA, S. NONEQUILIBRIUM CONDENSATION OF WATER AND CARBONTETRACHLORIDE VAPOR IN A SHOCK-TUBE. *Experiments in Fluids* **9**, 345-351 (1990).

137. Davidovits, P. et al. Mass accommodation coefficient of water vapor on liquid water. *Geophysical Research Letters* **31** (2004).

138. Ishiyama, T., Yano, T. & Fujikawa, S. Molecular dynamics study of kinetic boundary condition at an interface between a polyatomic vapor and its condensed phase. *Physics of Fluids* **16**, 4713-4726 (2004).

139. Meland, R., Frezzotti, A., Ytrehus, T. & Hafskjold, B. Nonequilibrium molecular-dynamics simulation of net evaporation and net condensation, and evaluation of the gas-kinetic boundary condition at the interphase. *Physics of Fluids* **16**, 223-243 (2004).

140. Kunz, W., Belloni, L., Bernard, O. & Ninham, B. Osmotic coefficients and surface tensions of aqueous electrolyte solutions: Role of dispersion forces. *Journal of Physical Chemistry B* **108**, 2398-2404 (2004).

141. Jungwirth, P. & Tobias, D. Specific ion effects at the air/water interface. *Chemical Reviews* **106**, 1259-1281 (2006).

142. Vrbka, L. et al. Propensity of soft ions for the air/water interface. *Current Opinion in Colloid & Interface Science* **9**, 67-73 (2004).

143. Jungwirth, P. & Tobias, D. Ions at the air/water interface. *Journal of Physical Chemistry B* **106**, 6361-6373 (2002).

144. MINKOWYC.WJ & SPARROW, E. CONDENSATION HEAT TRANSFER IN PRESENCE OF NONCONDENSABLES INTERFACIAL RESISTANCE SUPERHEATING VARIABLE PROPERTIES AND DIFFUSION. *International Journal of Heat and Mass Transfer* **9**, 1125-& (1966).

145. TANNER, D., POPE, D., POTTER, C. & WEST, D. HEAT TRANSFER IN DROPWISE CONDENSATION AT LOW STEAM PRESSURES IN ABSENCE AND PRESENCE OF NON-CONDENSABLE GAS. *International Journal of Heat and Mass Transfer* **11**, 181-& (1968).

146. NGUYEN, T. & WHITE, R. A WATER AND HEAT MANAGEMENT MODEL FOR PROTON-EXCHANGE-MEMBRANE FUEL-CELLS. *Journal of the Electrochemical Society* **140**, 2178-2186 (1993).

147. Peighambardoust, S., Rowshanzamir, S. & Amjadi, M. Review of the proton exchange membranes for fuel cell applications. *International Journal of Hydrogen Energy* **35**, 9349-9384 (2010).

148. Li, H. et al. A review of water flooding issues in the proton exchange membrane fuel cell. *Journal of Power Sources* **178**, 103-117 (2008).

149. Laaksonen, A., Vesala, T., Kulmala, M., Winkler, P. & Wagner, P. Commentary on cloud modelling and the mass accommodation coefficient of water. *Atmospheric Chemistry and Physics* **5**, 461-464 (2005).

150. Vadakkan, U., Chrysler, G.M. & Sane, S. in Semiconductor Thermal Measurement and Management Symposium, 2005 IEEE Twenty First Annual IEEE 182-186 (2005).

151. BATES, F. & FREDRICKSON, G. BLOCK COPOLYMER THERMODYNAMICS - THEORY AND EXPERIMENT. *Annual Review of Physical Chemistry* **41**, 525-557 (1990).

152. Fasolka, M. & Mayes, A. Block copolymer thin films: Physics and applications. *Annual Review of Materials Research* **31**, 323-355 (2001).

153. Smart, T. et al. Block copolymer nanostructures. *Nano Today* **3**, 38-46 (2008).

154. Tavakkoli, K. et al. Templating Three-Dimensional Self-Assembled Structures in Bilayer Block Copolymer Films. *Science* **336**, 1294-1298 (2012).

155. Jeong, B., Bae, Y., Lee, D. & Kim, S. Biodegradable block copolymers as injectable drug-delivery systems. *Nature* **388**, 860-862 (1997).

156. Rosler, A., Vandermeulen, G. & Klok, H. Advanced drug delivery devices via self-assembly of amphiphilic block copolymers. *Advanced Drug Delivery Reviews* **64**, 270-279 (2012).

157. Finnefrock, A., Ulrich, R., Toombes, G., Gruner, S. & Wiesner, U. The plumber's nightmare: A new morphology in block copolymer-ceramic nanocomposites and

mesoporous aluminosilicates. *Journal of the American Chemical Society* **125**, 13084-13093 (2003).

158. Pozzo, D. & Walker, L. Shear orientation of nanoparticle arrays templated in a thermoreversible block copolymer micellar crystal. *Macromolecules* **40**, 5801-5811 (2007).

159. Ciebien, J., Clay, R., Sohn, B. & Cohen, R. Brief review of metal nanoclusters in block copolymer films. *New Journal of Chemistry* **22**, 685-691 (1998).

160. Vriezema, D. et al. Self-assembled nanoreactors. *Chemical Reviews* **105**, 1445-1489 (2005).

161. Vriezema, D. et al. Positional assembly of enzymes in polymersome nanoreactors for cascade reactions. *Angewandte Chemie-International Edition* **46**, 7378-7382 (2007).

162. Shankar, R., Ghosh, T. & Spontak, R. Electroactive nanostructured polymers as tunable actuators. *Advanced Materials* **19**, 2218-+ (2007).

163. Asatekin, A. et al. Antifouling nanofiltration membranes for membrane bioreactors from self-assembling graft copolymers. *Journal of Membrane Science* **285**, 81-89 (2006).

164. Peinemann, K., Abetz, V. & Simon, P. Asymmetric superstructure formed in a block copolymer via phase separation. *Nature Materials* **6**, 992-996 (2007).

165. Jackson, E. & Hillmyer, M. Nanoporous Membranes Derived from Block Copolymers: From Drug Delivery to Water Filtration. *Acs Nano* **4**, 3548-3553 (2010).

166. Yamamoto, T. et al. Block Copolymer Permeable Membrane with Visualized High-Density Straight Channels of Poly(ethylene oxide). *Advanced Functional Materials* **21**, 918-926 (2011).

167. Yang, S. et al. Nanoporous membranes with ultrahigh selectivity and flux for the filtration of viruses. *Advanced Materials* **18**, 709-+ (2006).

168. Phillip, W., Rzayev, J., Hillmyer, M. & Cussler, E. Gas and water liquid transport through nanoporous block copolymer membranes. *Journal of Membrane Science* **286**, 144-152 (2006).

169. Daïan, J.-F. 1 online resource (ISTE, Ltd. ;

John Wiley & Sons,, London, UK

Hoboken, NJ; 2014).

170. Dullien, F.A.L. Porous media : fluid transport and pore structure, Edn. 2nd. (Academic Press, San Diego; 1992).

171. Ingham, D.B. & North Atlantic Treaty Organization. Scientific Affairs Division. Emerging technologies and techniques in porous media. (Kluwer Academic : Published in cooperation with NATO Scientific Affairs Division, Dordrecht ; Boston; 2004).

172. Joung, Y. & Buie, C. Electrophoretic Deposition of Unstable Colloidal Suspensions for Superhydrophobic Surfaces. *Langmuir* **27**, 4156-4163 (2011).

173. Liang, S. et al. Highly Hydrophilic Polyvinylidene Fluoride (PVDF) Ultrafiltration Membranes via Postfabrication Grafting of Surface-Tailored Silica Nanoparticles. *Acs Applied Materials & Interfaces* **5**, 6694-6703 (2013).

174. (U.S. Environmental Protection Agency, Washington, DC; 2008).

175. CHU, H., CAMPBELL, J. & LIGHT, W. HIGH-TEMPERATURE REVERSE-OSMOSIS MEMBRANE ELEMENT. *Desalination* **70**, 65-76 (1988).

176. Snow, M., deWinter, D., Buckingham, R., Campbell, J. & Wagner, J. New techniques for extreme conditions: High temperature reverse osmosis and nanofiltration. *Desalination* **105**, 57-61 (1996).

177. Wilf, M. & Klinko, K. Optimization of seawater RO systems design. *Desalination* **138**, 299-306 (2001).

178. CUPERUS, F. & NIJHUIS, H. APPLICATIONS OF MEMBRANE TECHNOLOGY TO FOOD-PROCESSING. *Trends in Food Science & Technology* **4**, 277-282 (1993).

179. Melin, T. et al. Membrane bioreactor technology for wastewater treatment and reuse. *Desalination* **187**, 271-282 (2006).

180. LEE, K., BAKER, R. & LONSDALE, H. MEMBRANES FOR POWER-GENERATION BY PRESSURE-RETARDED OSMOSIS. *Journal of Membrane Science* **8**, 141-171 (1981).

181. Hall, C. Polymer materials : an introduction for technologists and scientists. (Halsted Press, New York; 1981).

182. Taylor, J.R. An introduction to error analysis : the study of uncertainties in physical measurements, Edn. 2nd. (University Science Books, Sausalito, Calif.; 1997).

183. Love, J., Estroff, L., Kriebel, J., Nuzzo, R. & Whitesides, G. Self-assembled monolayers of thiolates on metals as a form of nanotechnology. *Chemical Reviews* **105**, 1103-1169 (2005).

184. HARE, E., SHAFRIN, E. & ZISMAN, W. PROPERTIES OF FILMS OF ADSORBED FLUORINATED ACIDS. *Journal of Physical Chemistry* **58**, 236-239 (1954).

185. Willey, T. et al. Rapid degradation of alkanethiol-based self-assembled monolayers on gold in ambient laboratory conditions. *Surface Science* **576**, 188-196 (2005).